Hydrophobic Engineering of a Bacterial Nanodimensional Capsule Protein

by

Omaima Ben Krayem

A thesis

presented to the University of Waterloo

in fulfilment of the

thesis requirement for the degree of

Master of Science

in

Chemistry

Waterloo, Ontario, Canada, 2017

I hereby declare that I am the sole author of this thesis. This is a true copy of the thesis, including any required final revisions, as accepted by my examiners.

I understand that my thesis may be made electronically available to the public.

Abstract

Recently, numerous protein-based nanomedicine platforms have been intensively explored. These systems are usually composed of self-assembling proteins that form controllable systems with different shapes and types. A particular type of the self-assembling proteins is the cage protein bacterioferritin (Bfr), a hollow protein that belongs to the ferritin superfamily of iron storage proteins. Bfr is composed of 24 *identical* protomers with 12 heme cofactors intercalated between adjacent subunits. Bfr has an 8 nm interior diameter and a 12 nm exterior diameter amenable for controllable modification. Previous investigations in the Honek laboratory involved engineering the Bfr cage proteins towards controlling the encapsulation of various guest molecules within its cavity. Polyhistidine amino acid sequences (His6-tags) were added to each of the C-termini of the Bfr protein subunits, which point towards the interior cavity of the protein, and successfully utilized as selective affinity interaction sites to bind several cargos such as a gold nanoparticle (AuNP), and a fluorescently labeled tetrameric protein, streptavidin. Additionally, the intrinsic heme cofactors were modified in different ways and reintroduced to the Bfr cage protein providing another approach for engineering this complex system. In the current study, the previously established engineering methodologies were utilized to investigate the possibility of engineering the Bfr cavity to be more hydrophobic and to examine its capability for encapsulating different hydrophobic molecules. The complexation between two different types of fatty acid-based molecules and the His6-Bfr cage protein was successfully achieved and analyzed. The two proof of concept guests studied in our laboratory were: a synthesized nonadecanoyl-nitrilotriacetic acid micelle and a commercially available lipid that has an NTA functionality preloaded with nickel ion. Also, another approach for labeling the heme propionate groups with long alkyl chains was investigated. Two long alkyl chain primary amines

were successfully added to the heme; however, the poor aqueous solubility of these hydrophobic analogues acts like a barrier towards their successful incorporation into the Bfr cage. The results gained from the above investigations highlight novel applications of not only Bfr, but also other cage proteins that have similar characteristics.

Acknowledgements

I would first like to thank my thesis advisor Prof. John F. Honek for being always around to help whenever I ran into a trouble spot or had a question about my research or writing. I am also grateful for his kind understanding and support when I had to go through the health challenges in my family.

I would also like to thank all the members of the Honek group who have a big contribution to the success of my work, in no particular order; Dr. Elisabeth Daub, Hawa Gyamfi, Noor Alamodi, David Kim, Taylor Urquhart, Yang Hu, Adrian Delgado, and Anton van der Ven. A special thanks to Yang Hu and Adrian Delgado, who contributed to performed the TEM experiments on my protein systems. I would also like to thank Dr. Jean Duhamel and Damin Kim who generously provided us with pyrene.

Acknowledgement must be made to the funding agencies of NSERC, the Libyan government, the Canadian Bureau for International Education (CBIE), and the University of Waterloo for funding.

Lastly, I would like to thank my little family, my dear husband and my lovely boys for their patience and support throughout the time of my studies. Also, a special thank you must go to my big family in Libya: my parents, my brothers and sister for supporting me spiritually throughout my studies and my life in general.

Table of Contents

List of Figures

List of Tables

Reaction Schemes

List of Abbreviations

^{1}H NMR: Proton nuclear magnetic resonance

AFF: 5-(aminoacetamido) fluorescein

ATRA: all-*trans* retinoic acid

AuNP: Gold nanoparticle

BCNU: Bis-chloronitrosourea

Bfr: Bacterioferritin

BNP: Bionanoparticles

CCMV: Cowpea chlorotic mottle virus

cmc: Critical micellar concentration

CPMV: Cowpea mosaic virus

CPP: Cell permeable peptide

Cys: Cysteine

Da: Daltons

DA: Dodecylamine

DCC: *N*,*N*′-dicyclohexylcarbodiimide

DCCH: 7-diethylaminocoumarin-3-carbohydrazide

DDP: Drug delivery platforms

DGS-NTA(Ni):1,2-dioleoyl-*sn*-glycero-3-[(N-(5-amino-1 carboxypentyl) iminodiacetic acid)succinyl] (nickel salt)

DLS: Dynamic light scattering

DMF: Dimethylformamide

DMPC**:** Dimyristoylphosphatidylcholine

DMPG: Dimyristoylphosphatidylglycerol

DMSO: Dimethyl sulfoxide

DNA: Deoxyribonucleic acid

DOX: Doxorubicin

Dps: DNA-binding proteins from starved cells

E. coli: *Escherichia coli*

EDC: *N*-(3-dimethylaminopropyl)-*N′*-ethylcarbodiimide hydrochloride

ELP: Elastin like polypeptide

EPR: Enhanced permeability and retention effect

Ftns: Ferritins

GdnHCl: Guanidine hydrochloride

Glu: Glutamate

His: Histidine

His6-Bfr: Bacterioferritin with hexahistidine tags attached to C-terminal of each subunit

IPTG: Isopropyl-β-D-1-thiogalactopyranoside

Kd: Dissociation constant

kDa: KiloDaltons

LB: Lysogeny broth

MDS: Micellar drug system

MRI: Magnetic resonance imaging

MS: Mass spectrometry

MW: Molecular weight

NA: Nonadecanoic acid

NBA: N-butylamine

NDI-ATRA: Nanodisk- all-*trans* retinoic acid

ND-NTA: Nonadecanoyl NTA

NEt_3: Triethylamine

NHS: *N*-hydroxysuccinimide

NTA: Nitrilotriacetic acid

OA: Octadecylamine

OD: Optical density

PEG: Polyethylene glycol

PEG-b-PCL: Polyethylene glycol-*b*-polycaprolactone

PPIX: Protoporphyrin IX

PS: Polystyrene

PS-DCC: Polystyrene-anchored dicyclohexylcarbodiimide

PS-TsCl: Polystyrene sulfonyl chloride

RFU: Relative fluorescence unit

RNA: Ribonucleic acid

SDS-PAGE: Sodium dodecyl sulfate polyacrylamide gel electrophoresis

SEC: Size exclusion chromatography

siRNA: Small interfering ribonucleic acid

TEM: Transmission electron microscopy

TLC: Thin layer chromatography

1. Chapter 1: Introduction

1.1. Overview

Recently, applications of bionanoparticles (BNP) in the field of medicine have intensively expanded; several nanoparticulate materials have been engineered in various ways for drug delivery and imaging purposes. A particular type of bionanoparticle is the cage protein, which consists of multiple subunits that self-assemble naturally to form varying hollow protein structures. Varieties of engineered cage proteins have the ability to host novel guest molecules within their cavity. Of interest to the current study is the cage protein bacterioferritin (Bfr), a hollow protein that belongs to the ferritin superfamily of iron storage proteins. Bfr is composed of 24 *identical* subunits with 12 heme cofactors intercalated between adjacent subunits. Bfr has an 8 nm interior diameter and a 12 nm exterior diameter amenable for controllable modification. The purpose of the presented experimental research is to further expand the versatility of Bfr as a bionanoparticle toward hydrophobic guest encapsulation and potentially molecular delivery. Changes in the hydrophobic character of the Bfr interior cavity through heme cofactor modification and through a series of controlled host-guest interactions have been explored. In this chapter, some nanomedical applications of proteins will be outlined, and the relevant background information on cage proteins, bacterioferritin, and encapsulation strategies will be discussed.

1.2. Proteins: platforms for nanomedical applications

Recent developments in the fields of bionanotechnology and medicinal chemistry have been focused upon the rational design of BNPs to be used as nanomedicine platforms. BNPs are preferred over completely synthetic NP for several reasons; such as, their well-organized architecture, uniform size, affordable large-scale production, and the availability of their genetic

sequence profile through which surface and intrinsic characteristics can be controlled by mutagenesis.[1] In particular, proteins and protein-like structures; for example, viral capsids, virus-like particles and protein cages like ferritins, heat shock proteins, vault cages and enzyme complexes (Figure 1.1), have been extensively studied as building blocks for BNP synthesis due to their biocompatibility, biodegradability and low toxicity.[2] A variety of these supramolecular units having a high degree of spatial organization and well-characterized self-assembly motifs has emerged as promising theranostic agents. Genetic alteration of protein scaffolds, such as the insertion of heterologous peptides or chemoselective bioconjugates into the protein shell has been used to produce scaffolds with medically relevant functionalization.[3-8]

Recently, selective chemical modification of protein scaffolds has achieved remarkable development. For example, the large surface area of protein-based NPs has been exploited for the attachment of multiple copies of affinity ligands, a process which has been shown to increase biomolecular target affinity.[9] An example of such enhancement was reported by Khor and collaborators who have modified the cowpea mosaic virus (CPMV) with multivalent display of peptide sequences on the surface which have increased its binding affinity to various targets.[10] Moreover, the surface modification of specific amino acid residues in viral capsids along with the alteration in their interior and interface have created viral capsids encapsulating molecular cargos such as the antitumor agent doxorubicin (DOX), polymeric sulphonic acid, and externally displayed antibody 19G2.[11-13] Other cage proteins such as small heat shock protein (Figure 1.1), whose interior and exterior have been genetically or chemically modified, have been used as a delivery platform for fluorescein, RGD 4C peptide, anti-CD4 antibody, and doxorubicin.[14-16] In fact, the unique container-like architecture of cage proteins has attracted extensive interest that has rapidly translated into potential medical applications. Ferritin/apoferritin protein cages, [17-20]

albumin, [21-23] casein, [24-27] elastin/elastin like polypeptide (ELP), [28-29] gliadin [30-31], collagen, [32,33] and gelatin, [34,35] are some of the proteins that have been successfully utilized as drug delivery platforms (DDP).

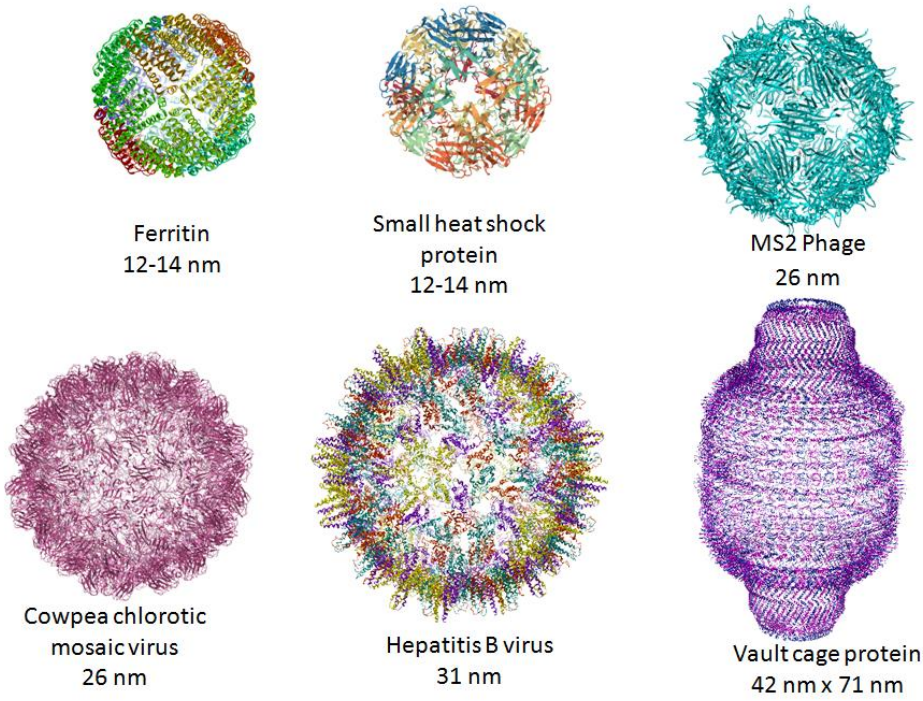

Figure 1.1: Structural illustration of some protein cages used as BNP for medical applications. The internal diameter of each protein is indicated. Images were generated in Chimera software using PDB IDs: 1BFR, 3VQK, 4ZOR, 2QZV, 5D7Y, 1CWP.

1.3. Bionanoparticles and hydrophobic drug delivery

Due to the fact that the vast majority of therapeutic agents are small hydrophobic molecules, efficient delivery of these hydrophobic dyes or drugs into their target cells has been the focus of attention for years. While chemical modification of new or existent hydrophobic compounds has been the "classical" approach to improve their pharmacokinetics and pharmacodynamic properties, many new investigations have focused on developing new strategies to improve the efficacy of poorly soluble hydrophobic molecules. BNPs as drug

carriers can provide new environments to incorporate various therapeutics, thus overcoming limitations caused by poor solubility of conventional drugs and improve their delivery.[36] Typical successful examples are the use of liposomes,[37] dendrimers,[38] and polymer conjugations such as poly(ethylene glycol) (PEG).[39] Despite the success of dendrimers and PEG-conjugated BNPs, which have been approved for clinical use, the size limitation and the lack of cellular targeting are critical drawbacks that made further development necessary. A newly developed BNP targeted for hydrophobic delivery can be found in the report of the sophisticated engineering of the Vault NP, which is a large ribonucleoprotein, encapsulating a recombinant nanodisc that is capable of carrying hydrophobic compounds (Figure 1.2).[40] Another attempt to generate a ferritin cage protein with a hydrophobic interior was proposed by a group of researchers from the University of Pennsylvania who has successfully designed a ferritin-like protein, DNA-binding proteins from starved cells (Dps), with a hydrophobic cavity through mutation of about 120 amino acids on the inside surface of the protein shell,[41] although previous studies suggested that hydrophobic mutation of hollow proteins may affect their stability.[42,43] The modified Dps cage protein exhibited reasonable stability and retained its natural capability of iron mineralization even with the large number of hydrophobic cavity mutations.

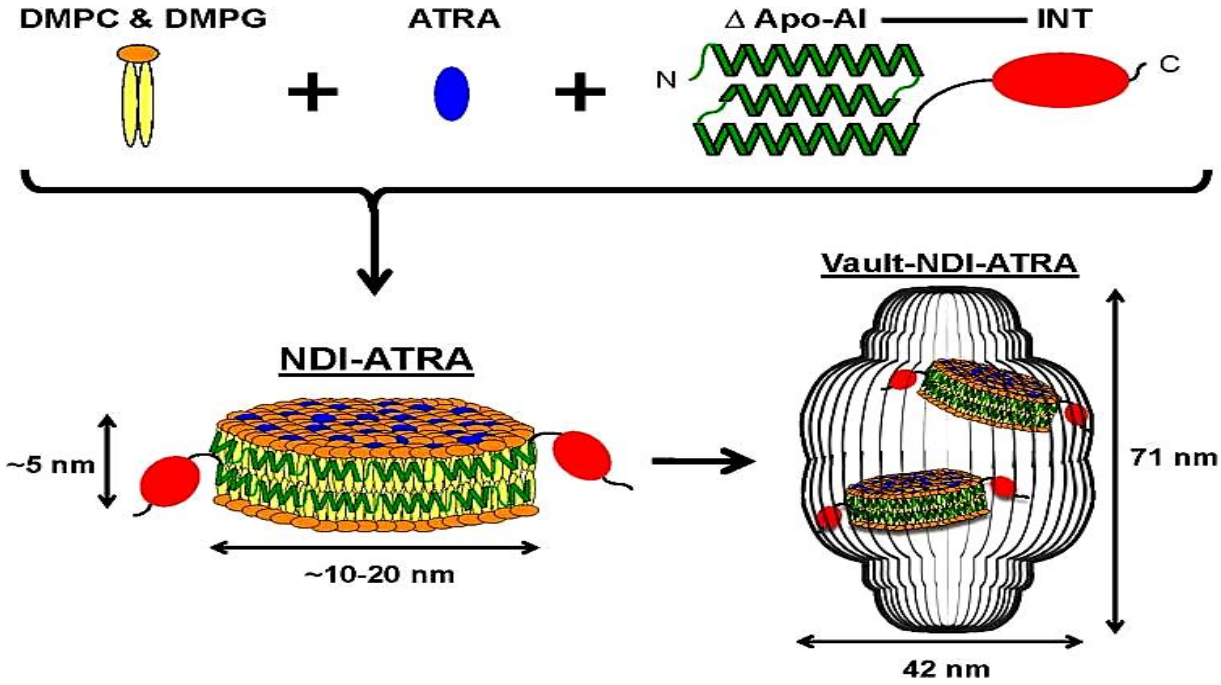

Figure 1.2: Schematic illustration of the nanodisk- all-*trans* retinoic acid (NDI-ATRA) formation and encapsulation into the vault nanoparticle. Dimyristoylphosphatidylcholine (DMPC) and dimyristoylphosphatidylglycerol (DMPG) lipids interact with Apolipoprotein-AI- binding domain INT (ΔApo-AI-INT) to form a discoidal phospholipid bilayer nanodisk (NDI). The amphipathic helices of ΔApo-AI-INT run perpendicular to the phospholipid acyl chains in a double belt-like manner around the circumference of the nanodisk. Addition of ATRA during formation results in the drug's absorption into the lipoprotein complex. NDI packaging into the vault nanoparticle is achieved by the vault binding-domain INT. The figure was taken with permission from Rome, L. *et al.*[40]

1.4. Designing BNPs with enhanced target specificity

Despite the tremendous advances in drug design and discovery especially in the field of chemotherapy, the lack of target specificity contributes for most of the unfavorable side effects of these therapeutics. Nonspecific binding of toxic drugs to uninfected, healthy tissues would result in unpleasant, if not serious, effects that have been a reason for withdrawal of a large number of drugs from clinical usage. Different strategies have been developed to overcome low target specificity such as passive and active targeting.

1.4.1. Passive targeting

Most of the clinically used NP-based drugs nowadays are passively targeted therapeutics, passively targeting a drug to certain types of cells, mainly tumor cells, involve the usage of drug formulations that will initially circumvent drug clearance through natural body defense mechanisms by the enhanced permeability and retention effect (EPR) of blood vessels and abnormal lymph drainage within diseased tissues (Figure 1.3) producing better therapeutic effect with substantially lower systemic toxicity.[44] Passive targeting involves modification of various elements that will enhance drug retention and accumulation within the body such as, molecular weight, surface charge, size and hydrophobicity of the carrier; surface modification of drug carriers was achieved by coating the surface with hydrophilic polymers or surfactants. PEG, poloxomer and polysorbate have been widely used for surface coating of drug delivery systems; for example, designed paclitaxil loaded NP fixed with a polymeric coat of PEG-polylactic acid exhibited high kinetic stability and prolonged retention time in blood circulation.[45] In a different study, DOX-loaded gelatin and PEGylated gelatin- based NPs presented increased accumulation rates within tumor cells compared to free drug.[46] Despite substantial improvement in therapeutic effects of drug systems targeted through passive targeting strategies, such drug formulations undergo non-specific uptake by healthy tissues leading to unpleasant, sometimes fatal, adverse effects due to the accumulation of drug in those tissues. Therefore, more efficient targeting pathways are being developed such as active targeting and drug-carrier-based targeting strategies.

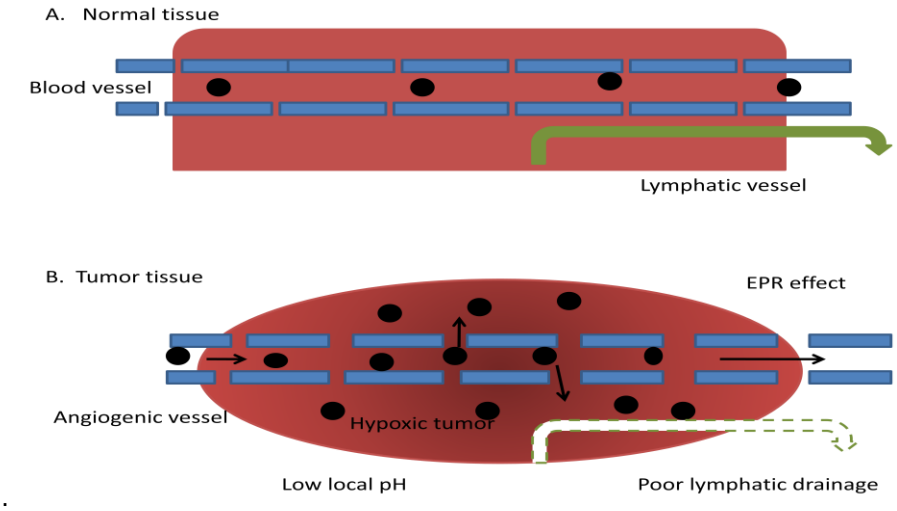

Figure 1.3: Tumor vascular pathophysiology and EPR effect in NP delivery. The normal (A) and the tumor (B) tissue microvasculature are represented. NPs with size between 10-100 nm could permeate through the leaky vasculature of the tumor tissue, while the intact blood vessels of normal tissues do not allow NPs leakage; therefore, the systemic toxicity will be substantially decreased, this figure was modified with permission from Upreti, M. *et al*.[44]

1.4.2. Active targeting

This targeting strategy involves the use of chemical and/or biological affinity ligands like peptides, monoclonal antibodies, and sugar chains, to direct NPs to their cellular targets; such ligands have featured recognition to their cellular targets which are usually overexpressed in diseased cells. An example of this strategy is Calicheamicin-conjugated anti-CD33 monoclonal antibodies that exhibited increased selectivity against acute myeloid leukemia cell lines that express CD33.[47] Another approach is based on targeting unique receptors expressed on the surface of malignant cells through NPs delivery systems linked to targeting peptides; upon binding, the drug system undergoes receptor-mediated endocytosis. For instance, two separate studies confirmed selective targeting of transferrin[48] and lipoprotein[49] receptors in hepatoma cells through transferrin-conjugated drugs and hematoporphyrin-modified albumin NPs, respectively. Another promising form of active targeting via aptamers, which are RNA or DNA oligonucleotides folded into three dimensional structures, has been investigated; the high

specificity combined with low immunogenicity of aptamers has attracted numerous researchers to design drug delivery formulations that contain aptamers as affinity ligands. Aptamer-based NPs have been employed as diagnostic as well as therapeutic agents; an example of their diagnostic applications is the design of fluorescent DNA-silver nanoclusters that were able to detect the presence of cancer cells early; detection signals were generated as a result of conformational changes that occurred upon binding of the aptamer to the cancer cells.[50] Moreover, several studies have confirmed the enhancement of targeted cytotoxicity of aptamer-based therapeutics against different types of cancer. An example can be found in the study of a paclitaxel-loaded NP conjugated to DNA aptamer that exhibited high affinity to the MUC1 protein that is overexpressed in adenocarcinoma cells. The investigated drug platform presented high accumulation rates and hence increased cytotoxicity against breast cancer cell line models.[51] Targeting tumor cells via aptamers was found to be a method of choice in terms of selectivity; however, the high cost of aptamer production and optimization can be a critical disadvantage.

1.5. The Ferritin superfamily

Of interest to this current study, ferritin cage proteins have been an important family among drug delivery platforms. Ferritins are globular iron storage proteins found in all life kingdoms, they are responsible for maintaining the iron concentration inside the cell within a normal range.[52,53] The ferritin superfamily can be divided into three subfamilies which are the classical ferritins (Ftns), bacterioferritin (Bfr) and the DNA-binding proteins from starved cells (Dps).[53] Proteins of this family consist of subunits that naturally self-assemble into roughly spherical cages with outstanding thermal and chemical stability.[52]

Several ferritin/apoferritin DDPs have been developed based on their assembly and disassembly properties; for instance, the ability of apoferritin to assemble and disassemble under

pH control has been utilized to encapsulate Daunomycin, an anthracycline antibiotic used in the treatment of certain types of cancer, and deliver it to cancer cells.[54] Another investigation reported the loading of a gadolinium complex, a contrasting agent used in magnetic resonance imaging (MRI), into the apoferritin cage protein (Figure 1.4).[55]

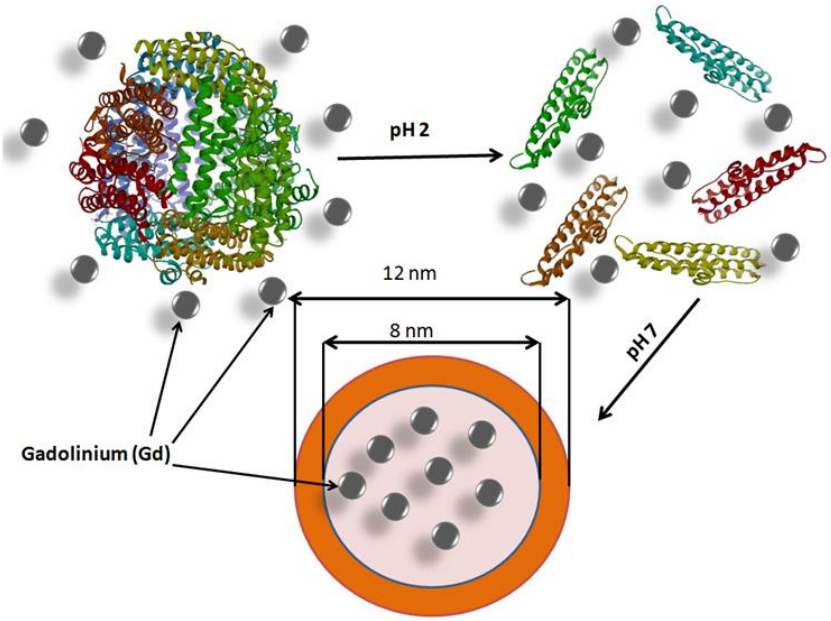

Figure 1.4: Schematic representation of the dissociation of apoferritin into subunits at pH 2, followed by its reformation at pH 7. In this way the solution components are trapped within the protein interior. The figure was modified from reference 55, and regenerated using the software program Chimera using PDB ID: 2W0O.

Moreover, a number of ferritin-based drug delivery platforms with an enhanced cellular specificity were designed; although ferritins are known for their natural cellular targeting through interaction with transferrin receptors, a number of affinity motifs, such as antibodies and primary peptides, were introduced to the ferritin nanocage surface in order to direct ferritin molecules to specific cells. Surface cysteine and lysine residues were exploited for the chemical addition of different dyes and targeting peptides to the exterior surface of the ferritin cage protein[56-60] (Figure 1.5). For instance, a ferritin-based DDP with enhanced cellular recognition was designed by a group of researchers from the University of Montana where a cell specific peptide, RGD-

4C, which exhibits tumor cell specificity, was incorporated on the exterior of human ferritin. This was accomplished by genetically modifying the external surface of the 12 nm multisubunit protein ferritin without affecting the structural or functional properties of the protein.[60] Some other applications of ferritin cages are listed in Table 1.[61]

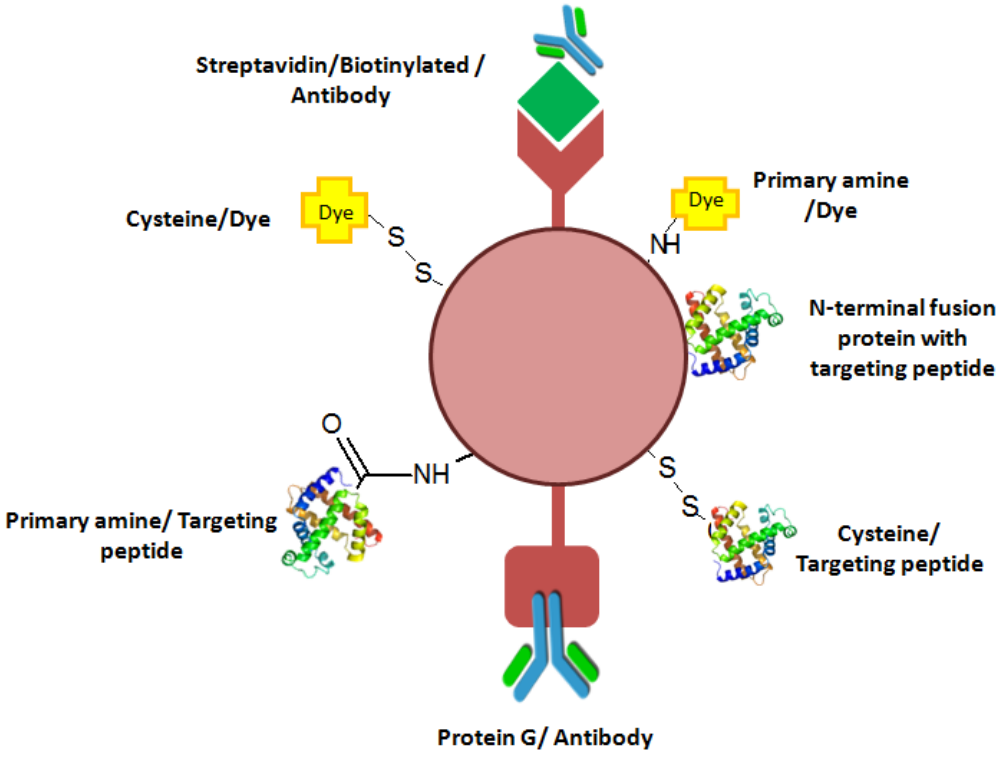

Figure 1.5: Schematic representation of various strategies adopted for addition of novel affinity motifs to the ferritin surface. This figure was taken in part and modified from reference 62.

Table 1: Applications and sources of ferritin used in bionanotechnology.[61]

Application	Core composition	Source
MRI contrast agent	Iron oxyhydroxide	Transfected human H-chain[63]
Phosphate removal from water	Ferric phosphate	*Pyrococcus furiosus* ferritin [64]
Quantum label	ZnSe	Horse spleen apoferritin[65]
Semi-conductor template	CdS/ZnSe	Apoferritin [66]
Au NPs	Au	Engineered human H-chain Ferritin[67]
Magnetic nanoparticles	Co_3O_4	Horse spleen apoferritin[68]

1.6. Bacterioferritin (Bfr)

1.6.1. Sequence identity

Recently, researchers in the Honek laboratory have been exploring the multiprotein complex Bfr from *Escherichia coli (E. coli)* as a cage protein and have investigated its possible application in the field of nanotechnology. Twenty-four identical subunits self-assemble to form the spherical hollow protein Bfr with inner and outer diameters of approximately 8 nm and 12 nm, respectively. Primarily, Bfr acts as an organelle that stores excess iron through the deposition of the solid Fe^{3+}, as an oxide, within its core.[69] Despite the high degree of structural conservation among members of the ferritin superfamily, the sequence identity between Bfr and other ferritins is less than 20%.[70] Since ferritin subfamilies share the same function which is deposition of oxidized iron within their cores, the residues involved in this process, also known as the ferroxidase centre, are highly conserved in all of the ferritin family members.[71]

1.6.2. Ferroxidase centre

Iron is essential for a wide variety of cellular processes. Ferritins play a crucial role in sustaining the cellular iron needs as well as maintaining iron homeostasis. Members of the ferritin superfamilies contain a dinuclear ferroxidase (iron) centre formed by intra-subunits for ferritins and Bfr, or inter-subunit interactions in Dps.[72,73] In the Bfr cage protein, the ferroxidase centre is composed of two iron binding sites in each subunit, each consisting of 4 glutamate residues (Glu18, Glu51, Glu94, and Glu127). Both Glu51 and Glu127 bridge two Fe^{2+}, while the other two Glu residues bridge two histidines (His54 and His130) (Figure 1.6).[74] This centre is responsible for binding the Fe^{2+} entering through the protein shell pores and oxidizing it to Fe^{3+}, which then forms the iron-oxide core of the protein. Like most ferritins, the Bfr cage protein can

accommodate a maximum of ~4500 iron atoms in its core;[75] however, the presence of intercalated 12 heme-b molecules between Bfr subunits is unique. Although the function of these heme molecules is not well identified, it has been reported that heme molecules play a role in releasing the iron ions from the Bfr core and enhance the iron core formation as well.[76]

1.6.3. Structural composition

Ferritin and Bfr have highly conserved quaternary structures. Two aspects are involved in the structure discussion of ferritin and Bfr. The first aspect concerns the functional unit of the ferroxidase center, the dimer (α_2), and the second concerns the intact 24-mer (α_{24}) quaternary structure. Each Bfr subunit is composed of 158 amino acids, with a molecular weight (MW) of 18.5 kiloDaltons (kDa). In total, the MW of the 24-mer protein complex is 443.9 kDa. The single Bfr subunit is composed of a left-handed, 4-α-helix bundle and one short helix at the C-terminus.[77] The N-terminus of each Bfr subunit faces the exterior surface while the C-terminus is situated to face the interior cavity of the cage protein. According to the three dimensional structure of Bfr, three types of channels are formed in the protein shell; eight are 3-fold symmetry channels, six are 4-fold symmetry channels and 24 are B-type channels (Figure 1.6). All of these channels mediate the transfer of iron in and out of the Bfr shell.[77] The Bfr 24-mer complex has an interior diameter of approximately 8 nm and an outer diameter of about 12 nm, with a total interior volume of 2144 nm^3.

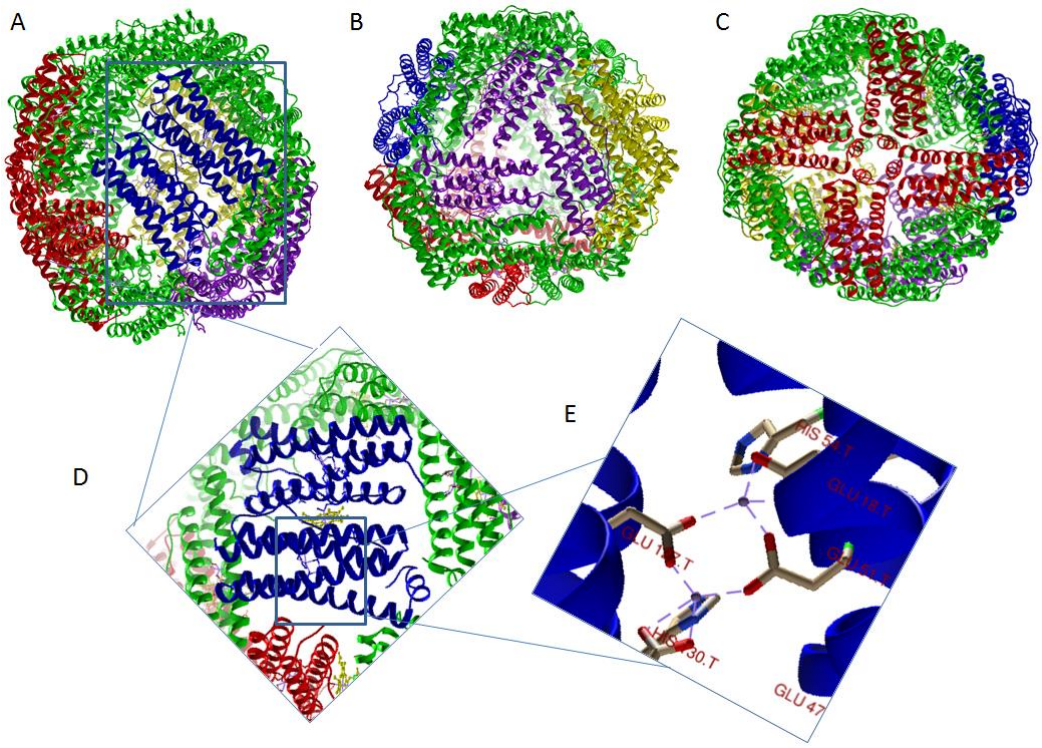

Figure 1.6: Structural overview of Bfr and the ferroxidase centre found at the interior surface of Bfr subunits. (A) The functional unit of Bfr, the dimer, is shown in blue within a 2-fold symmetry, one of the 3-fold symmetry channels is shown in purple (B), and a 4-fold symmetry channel shown in red in (c). Illustration of the heme, in yellow, situated between two adjacent protomers along with a focused image of the ferroxidase centre (E) showing the residues involved in coordinating 2 iron atoms (blue spheres). Images generated using Chimera software (PDB ID: 1BFR).

1.6.4. Heme cofactors

Heme is an iron Fe^{2+} containing cofactor, which is found in many metalloproteins, which are also known as hemoproteins, such as cytochromes, hemoglobin and myoglobin. Among the ferritin superfamily, Bfr is the only member that contains heme cofactors within its quaternary structure. Heme binding pockets exist between Bfr dimer interfaces, where two methionine residues contributed from two adjacent subunits coordinate one heme cofactor. According to the crystal structure of Bfr, heme propionate groups face the interior cavity of the protein. Although the function of these heme molecules is not well identified, it has been reported that the heme molecules play a role in releasing Fe^{2+} from the Bfr core and also enhance the iron core

formation.[77] The presence of heme in hemeproteins has provided additional sites for protein modification where useful functionalities can be labeled to the heme, through the modification of its propionate groups, and thus to the hemeprotein.[78,79] Different heme analogues have been synthesized and incorporated into the Bfr cage protein in our laboratory, in order to increase the versatility of this bionanoscaffold.[80] Further discussions of heme modifications will be presented in Chapter 2.

1.7. Encapsulation of functional guest molecules within cage proteins

The encapsulation of various guest molecules within DDP involves different kinds of host-guest interactions. In fact, understanding the methods used to encapsulate guest molecules is of critical importance to develop successful molecular delivery platforms. To date, the demand for designing effective DDP with well-understood and controllable host-guest interactions has been an active area of research. The encapsulation of novel guest molecules within cage proteins usually requires the disassembly of these cages, which allows various guest molecules to interact with the interior surface of the host protein. Upon interaction, protein cages reform their cage structures trapping the desired guest molecules within their cavities. Three strategies for guest molecules encapsulation are discussed below.

1.7.1. Concentration-dependent encapsulation

This strategy is one of the least favorable methods for encapsulation. The methodology is based on the disassembly of cage proteins in the presence of high concentrations of a guest molecule. Upon reassembly, the cage protein will encapsulate unpredictable quantities of the guest molecules within the cavity.[81] There are two critical disadvantages of this method; first is the lack of attractive forces between the host protein and the guest molecule; therefore a minor

repulsive force could be a barrier toward successful encapsulation. The second reason is the limited control over the encapsulation process, since variation in the number of guest molecules encapsulated can be observed under identical experimental studies. This non-specific strategy can be useful when high concentrations of guest molecules are available and it could be of preference to some researchers since no protein modification is needed. For instance, encapsulation of a small drug, cisplatin, into ferritin was accomplished utilizing concentration-based encapsulation experiments.[82] Another example of this approach was the encapsulation of horseradish peroxidase within cowpea chlorotic mottle virus (CCMV) using high concentrations of the guest enzyme.[83]

1.7.2. Covalent and genetically engineered encapsulation

In this second strategy, covalent bonds that can be formed between the host protein and the guest molecules can be utilized to achieve stable irreversible encapsulation. Although such interaction can be favorable for applications that do not require the release of the guest molecules such as cell imaging and enzyme encapsulations, however, other applications such as molecular delivery requires the encapsulated guests to be released upon reaching their targets. In case of cage proteins and peptides, genetic modification of the inner surface can provide covalent linkage to the guest molecules; example of this approach was reported by Douglas and coworkers, who were able to engineer bacteriophage P22 virus toward the encapsulation of a wide variety of enzymes such as CelB glycosidase and alcohol dehydrogenase.[84,85] Moreover, direct labeling of amino acids can be utilized to mediate covalent encapsulation of various functional molecules. The incorporation of a cysteine (Cys) residue by site-specific mutagenesis of the capsid interior of bacteriophage MS2 serves as an example of this approach. Added Cys

was utilized to covalently encapsulate a photodynamic therapeutic within the virus cage, and the loaded host protein was successfully directed to cancer cell surfaces.[86]

1.7.3. Non-covalent directed encapsulation

Non-covalent host-guest interaction creates a dynamic interaction, which may be beneficial for releasing different cargos in many studies. For example, a gold nanoparticle (AuNP) displaying a nitrilotriacetic acid (NTA) moiety on the surface was non-covalently bound to the Vault associated protein which was genetically modified to have a His-tag on its internal surface.[87] The non-covalent interaction between His-tags and the NTA moieties have provided a strong bond for a controllable cargo encapsulation. Similarly, the genetic addition of binding motifs to scaffolding proteins has increased the versatility of these nanodevices; for example, a chimeric viral capsid that has the ability to bind different types of therapeutic siRNA was designed through the fusion of a p19 RNA binding protein to the Hepatitis B virus.[88]

In fact, a number of non-covalent directed encapsulation studies were investigated in our laboratory using the Bfr cage protein, which was genetically engineered by Dr. Uthaiwan Suttisansanee onto the C-termini to have hexahistidine tags,[89] as a scaffold. His-tags have been shown to promote several host-guest interactions between the engineered Bfr and a variety of functional guest molecules containing NTA functionalities (Figure1.7). For example, the large tetrameric protein streptavidin and 5 nm AuNPs were successfully encapsulated in separate experiments in the 8 nm cavity of Bfr.[80] These His-tags were found to be essential to the encapsulation process since the absence of interactions between the cargo and the encapsulating cavity resulted in the failure of any encapsulation of guest molecules. This particular type of

host-guest interaction, the NTA-histidine interaction, is highly specific as its dissociation constant (K_d) is fairly low.[90]

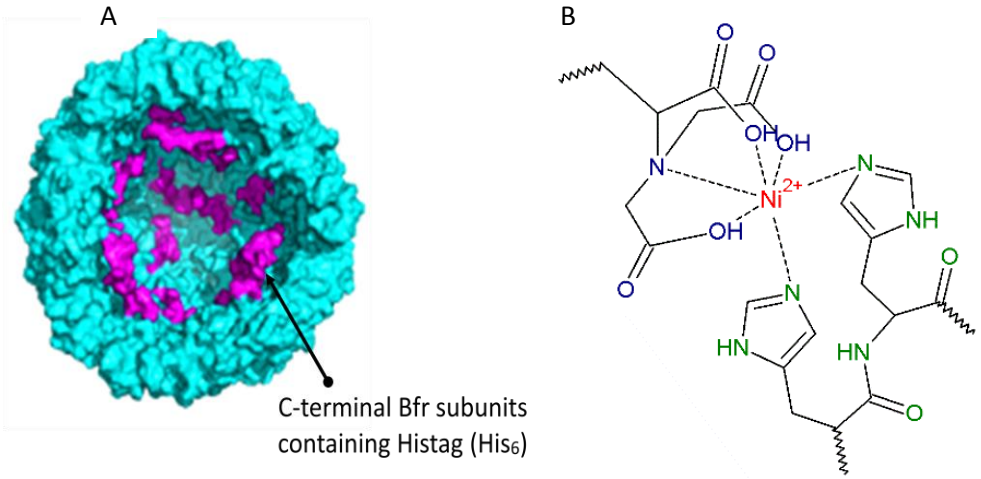

Figure 1.7: Illustration of two basic structures required for metal-mediated affinity interactions involved in the Bfr engineering. (A) X-ray structure of bacterioferritin with modeled His-tag residues at the C-terminus of the Bfr subunits (B) nitrilotriacetic acid (NTA) functionality coordinating a nickel atom (red) with two histidine residues. This affinity interaction was utilized for encapsulation of two large guest molecules within Bfr by the Honek group.

1.8. Motivations for pursuing Bfr engineering

The success in developing the Bfr cage protein to be an effective molecular delivery platform has opened a window for further explorations. The purpose of the work presented in this thesis is to develop the Bfr cage protein to serve as a delivery platform for hydrophobic guest molecules. Two approaches are designed to develop the Bfr cage to accommodate structures with long alkyl chains: firstly, the heme cofactors would be chemically modified with long alkyl chains attached to the heme propionate groups. Secondly, the His6-tags, which have been previously attached to the Bfr subunits, would be involved in a series of Ni^+ mediated affinity interactions with two long alkyl chains structures with NTA functionalities. Creating a controllable hydrophobic environment within the Bfr core would allow for several drugs or dyes to be encapsulated into this nanosized capsule. The success of the presented research may

highlight novel promising applications of the Bfr and other cage proteins as potential bio-NPs in nanomedicine.

Chapter 2: Heme Cofactor Modification

2.1. Introduction

Unlike other members of the ferritin superfamily, Bfr is the only family member that contains heme cofactors. Heme is a protoporphyrin with an iron atom in the centre of the porphyrin ring. In the cage of Bfr, twelve heme cofactors can be incorporated into a single Bfr capsule; heme cofactors are coordinated through two methionine residues, M52, from separate subunits (Figure 2.1). The protein-binding pockets for heme are on the inner face of Bfr and the propionate groups of the heme point towards the interior cavity of the protein. The nature of the heme propionate groups provided opportunities for the addition of novel functionalities and ligands to the heme cofactor and thus Bfr. Moreover, the success in individually modifying the heme propionate groups has increased the complexity of heme labeling.[91,92] These factors have made heme an ideal candidate to explore the further development of Bfr as a platform for bionanotechnology. For the past few years, several synthetic heme analogues were synthesized and incorporated into Bfr in the Honek laboratory; such as, labeling the heme with a fluorescent coumarin derivative, 7-diethylaminocoumarin-3-carbohydrazide (DCCH) and a fluorescein derivative, 5-(aminoacetamido) fluorescein (AAF) in two separate experiments (Figure 2.2.A&B).[80] A new approach was designed to utilize heme cofactors to change the hydrophilic character of the Bfr cavity into a hydrophobic cage in order to expand the versatility of Bfr as a molecular delivery platform (Figure 2.3).

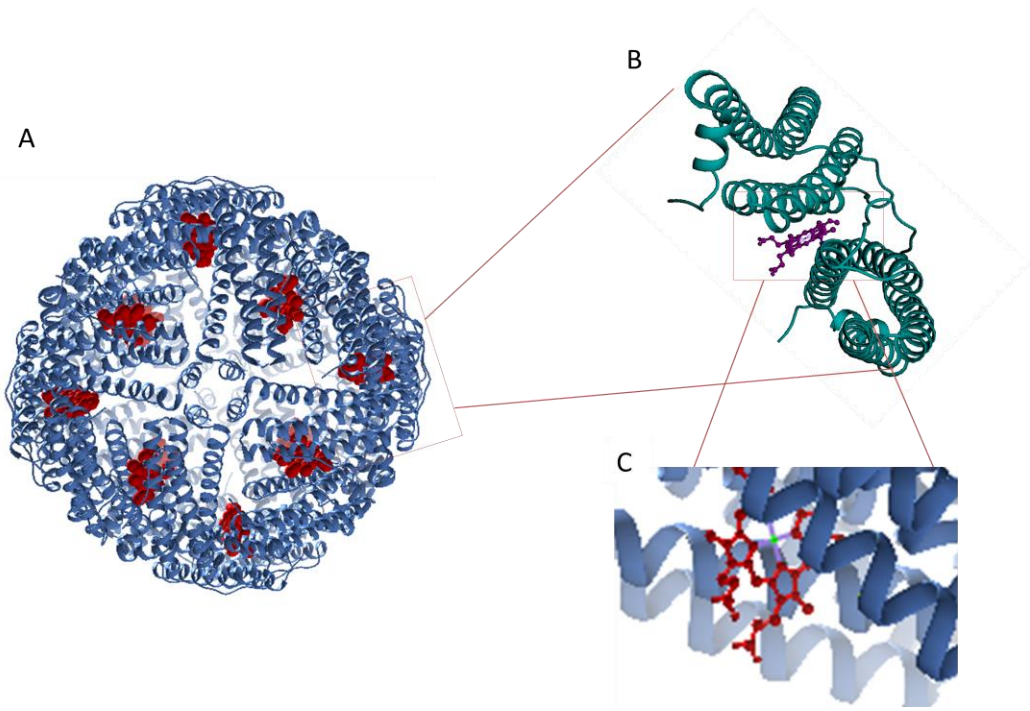

Figure 2.1: Heme cofactors are coordinated between two Bfr subunits. (A) Twelve heme cofactors can be incorporated into Bfr, eight are shown in red. (B) Illustration of heme positioning between two Bfr subunits with heme propionate groups pointing to the interior of the protein (C). Images were generated using Chimera software (PDB ID: 1BFR)

In this chapter heme modification of the propionate groups with a variety of lengths of alkyl chains, namely N-butylamine (NBA, $CH_3(CH_2)_3NH_2$), octadecylamine (OA, $CH_3(CH_2)_{17}NH_2$) and dodecylamine (DA, $CH_3(CH_2)_{11}NH_2$) will be explored. Different strategies for heme propionate group activation and labeling were investigated in order to obtain the ideal conditions for the synthesis of hydrophobic heme analogues; experimental procedures and results will be discussed. Also, attempts to introduce heme-DA analogues to the His6-Bfr will be presented and discussed.

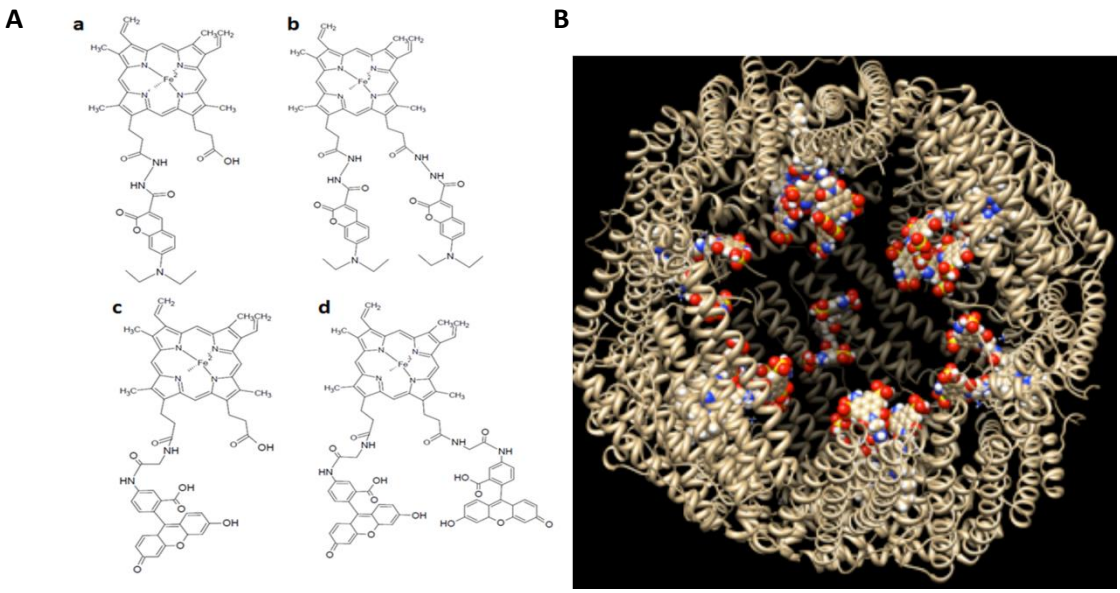

Figure 2.2: Structures of some of the heme analogues synthesized in the Honek laboratory and successfully introduced into bacterioferritin (A): (a) heme-mono-DCCH, (b) heme-bis-DCCH, (c) heme-mono-AAF and (d) heme-bis-AAF. Also, in B a modeled fluorescent dye attached to each of the propionate groups of heme cofactors are shown in the Bfr structure to obtain an approximate idea of the size and positioning of the dyes within a bacterioferritin cavity.

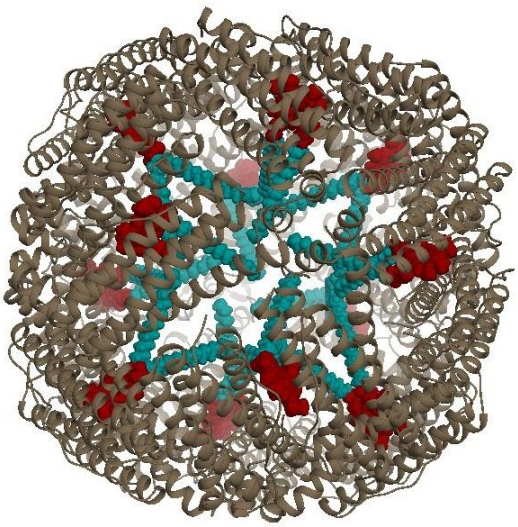

Figure 2.3: Illustration of the investigated approach to incorporate hydrophobic heme analogues into the Bfr. C18 amine (cyan) are linked to each of the two propanoic acids of each of the twelve heme cofactors. Image was generated in Chimera using PDB ID: 1BFR. C18 amines were chemically drawn linked in an amide bond to each heme propanoic acid.

2.2. Experimental

2.2.1. Materials

Hemin (Sigma-Aldrich, Buchs, Switzerland), Polystyrene-carbodiimide (Biotage, Hengoed, United Kingdom), N-hydroxysuccinimide (1-hydroxy-2,5-pyrrolidinedione) (Sigma-Aldrich, Louis, MO, USA), *N*-(3-dimethylaminopropyl)-*N′*-ethylcarbodiimide hydrochloride (EDC) (Sigma-Aldrich, Oakville, ON, Canada), *N*,*N′*-dicyclohexylcarbodiimide (DCC) (Sigma-Aldrich, Oakville, ON, Canada), and oxalyl chloride (Sigma-Aldrich, Oakville, ON, Canada) were used as received. Dimethylformamide and dimethyl sulfoxide (Sigma-Aldrich, Sheboygan Falls, WI, USA), pyridine and dichloromethane (Sigma-Aldrich, Oakville, ON, Canada) all in anhydrous form were utilized from a Sure-Seal^{TM} bottle and were stored over dry 4 Å molecular sieves before use for synthesis. N-Butylamine was purchased from Spruce Street, Saint Louis, MO, USA and octadecylamine and dodecylamine from Sigma-Aldrich, Milwaukee, WI, USA. Polystyrene benzaldehyde (PS-benzaldehyde) (1.2 mmol/g) and polystyrene sulfonyl chloride (PS-TsCl) (2.0 mmol/g) (Biotage, Hengoed, United Kingdom) were used as provided by the manufacturer.

2.2.2. Safety statement

All solvents and chemicals were handled with appropriate glove wear, laboratory coats, safety goggles, and in a fume hood. Chromatography using solvents was performed in a fume hood, and silica resins and thin layer chromatography (TLC) plates were disposed of properly through the hazardous waste management facility.

2.2.3. Activation of heme propionate groups using carbodiimide and N-hydroxysuccinimide (NHS)

In previous work, the reaction of heme with carbodiimide and NHS has been used to achieve the activation of heme propionate groups. Heme-NHS served as a semi-stable intermediate, which could be used directly to label heme with molecules containing primary amines or hydrazide functionalities (Scheme 2.1).

The procedure for the heme-NHS synthesis reaction was previously reported in the literature.[92] Hemin ((Chloro(protoporphyrin)iron(III); 200 mg, 307 µmol) was first stirred with polystyrene-anchored dicyclohexylcarbodiimide (PS-DCC) (954 mg, 2.8 equiv., 130 µmol/g) in anhydrous DMF (3.2 mL) at 23 °C for 10 minutes, followed by the addition of NHS (88 mg, 2.5 equiv., 760 µmol). The solution was stirred for 1 h, at 100 ^{0}C in a Biotage® Initiator Microwave Synthesizer (Scheme 2.2.a). After one hour, the reaction was allowed to come to room temperature and the mixture was filtered using a column with glass wool packed at the bottom to remove PS-DCC beads.

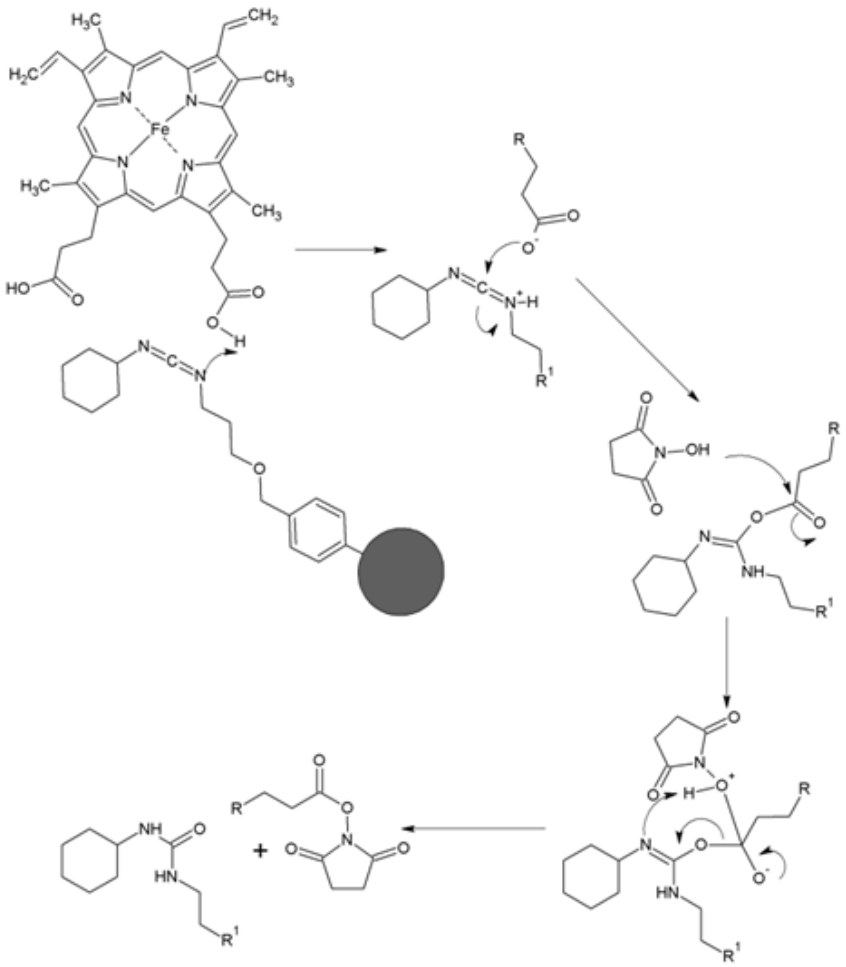

Scheme 2.1: Reaction mechanism for the synthesis of heme-NHS using a polystyrene linked carbodiimide.

The soluble hemin-containing compounds were precipitated by addition of a 10x volume of chilled, dry isopropanol. This was followed by centrifugation at 5000*g* for 20 minutes in a VWR clinical 100 centrifuge. The dark pellet was collected, dried under vacuum and stored away from light exposure at -20 °C. The product was analyzed using TLC on silica gel plates with dichloromethane and methanol (9:1) as elution solvent. The final heme-NHS product, mono and bis-substituted heme, had two R_f values 0.62 and 0.75. The product was used without further purification.

2.2.4. Heme-NHS reaction with NBA, DA and OA

Following the same protocol used previously in the Honek laboratory, heme-NBA was synthesized by mixing heme-NHS (3.4 mg, 4.2 µmol) with NBA (1.2 mg, 16 µmol, 4 equiv.) and stirring in anhydrous DMF (500 µL) at 100 °C for 40 minutes in a Biotage® Initiator Microwave Synthesizer.

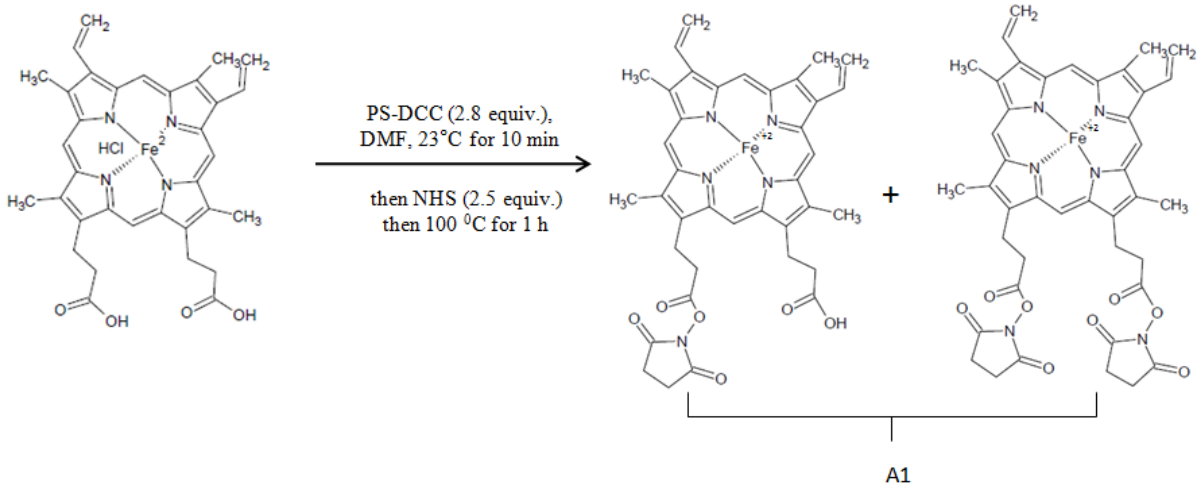

Scheme 2.2.a: Heme-NHS synthesis from heme activated with PS-carbodiimide and then reacted with NHS.

A number of trial reactions to synthesize the heme-OA analogues were performed under various reaction conditions. Different equivalents of OA were added to heme-NHS (20 mg, 24.6 µmol) and then dissolved in either $CHCl_3$ or DMF; the reactions were heated in the Biotage Initiator Microwave Synthesizer at 80 ^{0}C, 100 ^{0}C, and 120 ^{0}C for 1 h, 2 h and 5 h. In another experiment OA (16.5 mg, 61.5 µmol, 2.5 equiv.) was first melted at 100 ^{0}C for 20 minutes, followed by adding heme-NHS (20 mg, 24.6 µmol). The mixture was kept at 100 ^{0}C for 1 h in a Precision™ Gravity Convection oven. Once cooled to room temperature, the product was taken up in 500 µL hexane, washed with equal volumes of DMF (3X) and analyzed using mass spectrometry (MS). Attempts to remove the excess OA from heme-OA reactions were performed

using scavenger resins. In one experiment polystyrene sulfonyl chloride (PS-TsCl) (24.6 mg, 39.3 µmol, 2 equiv.) was added to the product of the heme-OA reaction, stirred for 5 h at 23 ^{0}C followed by heating at 50 ^{0}C for two hours in the Biotage® synthesizer. The beads were filtered from the solution using glass wool and the flow through solution was analyzed using MS. In another experiment, polystyrene benzaldehyde resin (63 mg, 57.8 µmol, 3 equiv.) was stirred with the product of heme-OA reaction, two drops of methanol were added to catalyze the reaction; the reaction was stirred for 18 h. A column packed at the bottom with glass wool was used to filter out the beads and the solution was analyzed using MS (Scheme 2.2.b).

Heme-DA was synthesized by mixing heme-NHS (20 mg, 24.6 µmol) with DA (13.3 mg, 72 µmol, 3 equiv.) and stirring in anhydrous DMF (1mL) at 100 °C for 1 h in a Biotage® synthesizer. The reaction time was increased to 3 h in another experiment to assess the time effect on the chemical reaction (Scheme 2.2.b).

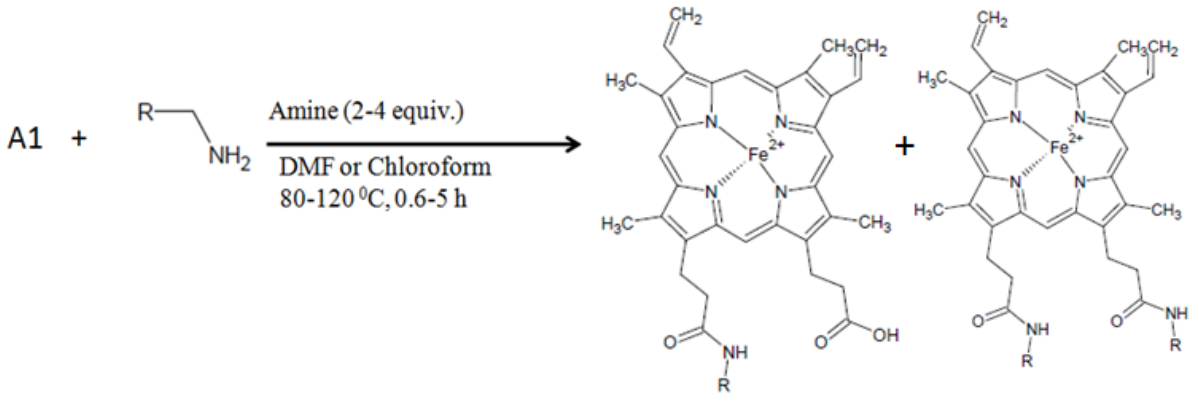

Scheme 2.2.b: Reaction of heme-NHS with primary alkyl amines

2.2.5. Reaction of heme with DA and OA in the presence of carbodiimides

Heme-DA was synthesized by dissolving hemin chloride (50 mg, 76.6 µmol) in 1.5 mL DMF or pyridine followed by addition of EDC (36.7 mg, 191.5 µmol, 2.5 equiv.) and then DA

(35.5 mg, 191.5 µmol, 2.5 equiv.). The solution was heated at 100 ^{0}C for 2 h in Biotage® synthesizer. Attempted syntheses of heme-OA using the previous procedure were conducted, using 1.5 and 2.5 equiv. of OA, and the temperature and reaction times were varied in different experiments as well. Dicyclohexylcarbodiimide (DCC) was used as an alternative coupling agent for another set of reactions using the same protocol as well. In addition, following a reported procedure for heme-bis-OA synthesis in the literature,[79] an experiment was carried out where hemin chloride (20 mg, 30.6 µmol) was stirred in anhydrous pyridine (1.5 mL) for 30 min at 0 ^{0}C; DCC (15.7 mg, 76.5 µmol, 2.5 equiv.) was added and the solution was stirred for 1.5 h. Then OA (20.6 mg, 76.5 µmol, 2.5 equiv.) in pyridine (1 mL) was gently added to the previous mixture and stirred at 0 ^{0}C for 24 h. A similar reaction was repeated at room temperature and was monitored for 12 days. The products of both reactions were analyzed using MS (Scheme 2.3).

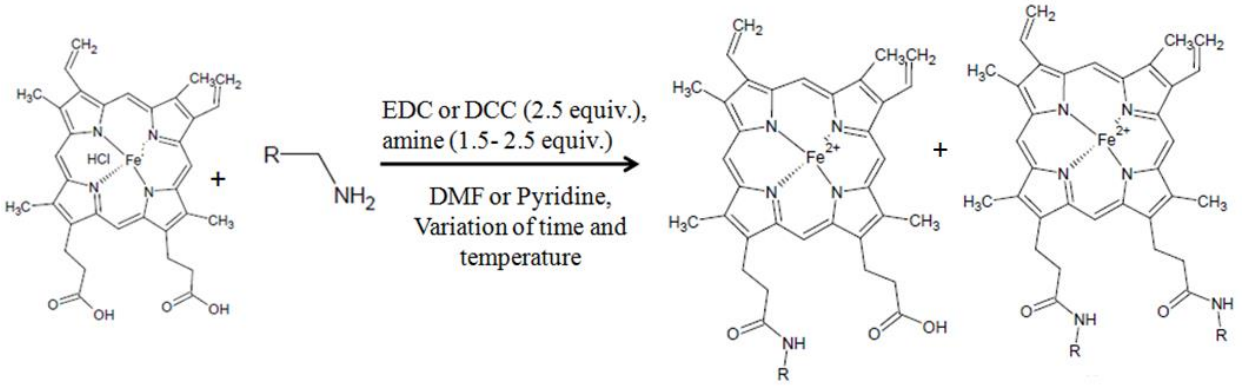

Scheme 2.3: Reaction of heme with DA and OA in the presence of carbodiimides

2.2.6. Reaction of heme with DA and OA in the presence of oxalyl chloride

Based on a protocol from the literature, a procedure that involved the activation of protoporphyrin IX propionate groups using oxalyl chloride was attempted.[93] Reactions were

started by suspending hemin chloride (50 mg, 76.6 µmol) in anhydrous dichloromethane (10 mL). Oxalyl chloride (100 µL, 153.2 µmol, 2 equiv.) was added along with anhydrous DMF (5 µL). The solutions were stirred for 1 h, solvents were evaporated under vacuum and the greenish brown intermediate product, heme-dichloride, was collected (Scheme 2.4.a). The heme-dichloride intermediate was dissolved in anhydrous pyridine (5 mL) mixed with anhydrous DMF (2 mL). DA (35.5 mg, 191.5 µmol, 2.5 equiv.) or OA (51.6 mg, 191.5 µmol, 2.5 equiv.) were dissolved in anhydrous pyridine (1.5 mL) and gently added to the solution and stirred for 10 h in two separate experiments (Scheme 2.4.b).

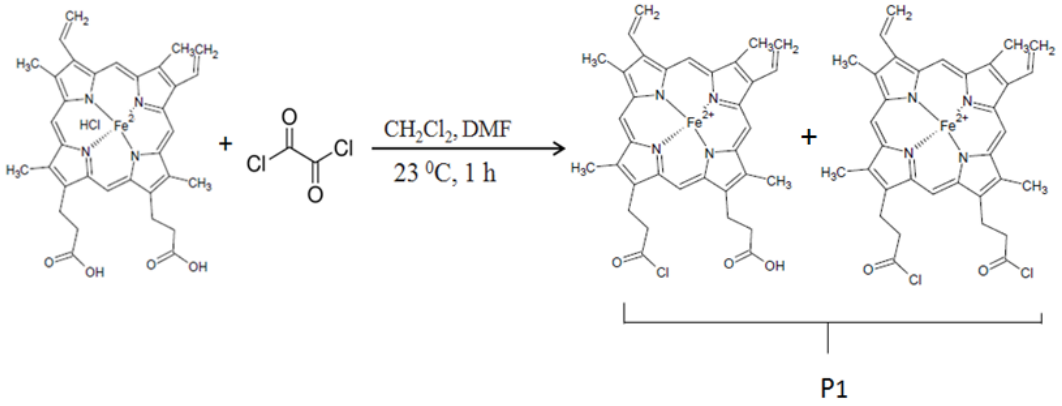

Scheme 2.4.a: Reaction of hemin chloride with oxalyl chloride to form mono and bis chloro heme intermediate.

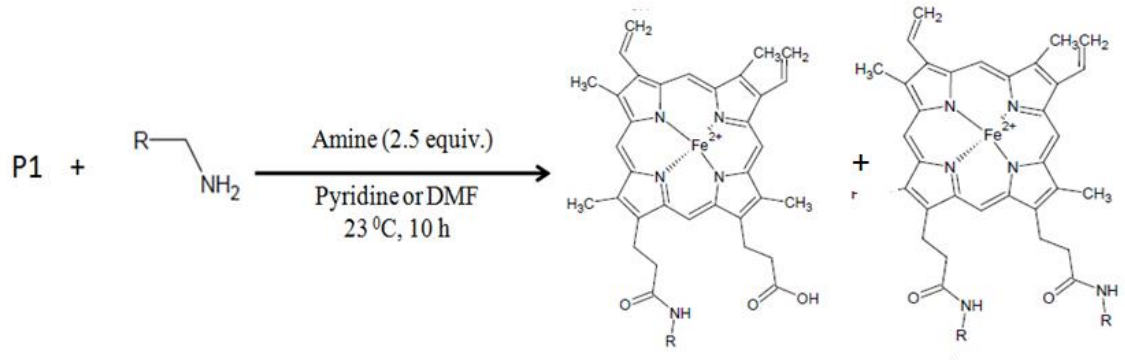

Scheme 2.4.b: Reaction of heme chloride adducts with long chain primary amines.

2.2.7. Reaction of protoporphyrin IX with OD and DA in presence of oxalyl chloride

Protoporphyrin IX-DA (PPIX-DA) analogue was synthesized by suspending PPIX (40 mg, 53.3 µmole) in anhydrous dichloromethane (15 mL). Oxalyl chloride (75 µL, 106.6 µmole, 2 equiv.) was added along with 2 drops of DMF; the mixture was stirred for 1 before the solvent was evaporated under vacuum and the greenish brown solid product was collected. This material was dissolved in anhydrous pyridine (3 mL) and DMF (2 mL). DA (24.6 mg, 133.2 µmole, 2.5 equiv.) was dissolved in anhydrous pyridine (1 mL) and added slowly to the above reaction mixture, which was stirred for 10 h; reaction product was analyzed using MS. The same procedure was followed for the synthesis of PPIX-OD adduct, using 30 mg of OA (133.2 µmole, 2.5 equiv.)

2.2.8. Purification of heme-DA products

Purifications of products of both heme-NHS and hemin chloride reactions with DA were performed. Heme-DA analogues were purified on a Biotage® KP-SIL SNAP column with a Biotage® Isolera chromatography system. Solvents were completely evaporated under vacuum, and the solid residues were dissolved in 2 mL dichloromethane (CH_2Cl_2); this was then added to a Biotage® KP-SIL samplet (1 g) where a tight brown band would form at the top of the samplet cartridge. Once dry, the samplet cartridge was added to the top of a KP-SIL cartridge (10 g resin) that had been equilibrated with 50 mL of a 9:1 chloroform:methanol mixture. The samplet cartridge was then added to the top of the column, and an elution gradient was applied (100% CH_2Cl_2 to 100% methanol in a total volume of 290 mL). Several solvent conditions to separate the bis-heme product from mono-adduct were investigated as well.

2.2.9. Attempts for incorporating heme-DA analogues to the His-Bfr cage protein

Heme-DA in DMF or DMSO (7×10^{-8} mol, 1.0 equiv.) was added to His6-tag Bfr (7.0×10^{-8} mol) buffered with 0.2 M MES and 1.0 M NaCl at pH 6.5. The mixture was then placed in a water bath at 80 °C for 10 minutes. After 10 minutes of incubation the mixture was allowed to cool to 23 °C. The precipitated heme was removed through centrifugation at 7650*g* for 10 minutes. Protein samples were purified using a GE SephacrylTM S-300HR resin, with a void volume of 99.05 mL, a running flow rate of 0.5 mL/min, and collecting fraction volumes of 1 mL.

2.2.10. MS experimentation

Crude reaction samples were prepared by diluting 5 μL of a 16 mM crude reaction into 50 μL of 1:1 MeCN: H_2O with 0.2% formic acid, and further diluting 5 μL of this dilution into 50 μL of the same solution. This was run on a Thermo Scientific LTQ Linear Ion Trap mass spectrometer.

2.3. Results and Discussion

Different methodologies for the synthesis of various hydrophobic heme analogues were explored. The results of the attempted syntheses will be presented and discussed in this section.

2.3.1. Heme preparation and modification

2.3.1.1. Heme activation with NHS

The first work with heme labeling in the Honek laboratory, was started by an undergraduate student, Denise Lieuson, who had successfully developed a method for heme-NHS synthesis, followed by labeling of the activated heme with N-butylamine (NBA). This work had set the stage for more heme analogue syntheses conducted by Anton van der Ven.[80] Hemin chloride, which is identical to heme with the exception that a chloride coordinates the heme iron, is highly soluble in DMF; therefore, most of the reactions were carried out in anhydrous DMF. The method that was eventually used for the majority of heme labeling reactions involved mixing hemin with a polystyrene bead linked carbodiimide (PS-DCC) and NHS in DMF. Heme activated by carbodiimide reacts with NHS to various extents; however, the majority of heme is fully activated to heme-bis-NHS, with some heme-mono-NHS detected (Figure 2.4). The heme-mono-NHS product was not separated from the bis-NHS product because purification can be performed after further reaction of the mixture with various amines. All equivalents were calculated under the assumption that the product, heme-NHS, is a 100% heme-bis-NHS. Heme reaction with NHS appeared to proceed toward completion, as monitored by MS, and formed largely the heme-bis-NHS product, which is consistent with what was reported by previous students. The product was analyzed using thin layer chromatography (TLC) on silica gel plates using dichloromethane and methanol (9:1) as elution solvent. (R_f = 0.62 (monoester); 0.75 (bis-

ester)). MS analysis using a Thermo Scientific LTQ^{TM} gave m/z for M^{+}= 713 (monoester, predicted: 713.55), 810 (bis-ester, predicted: 810.63).

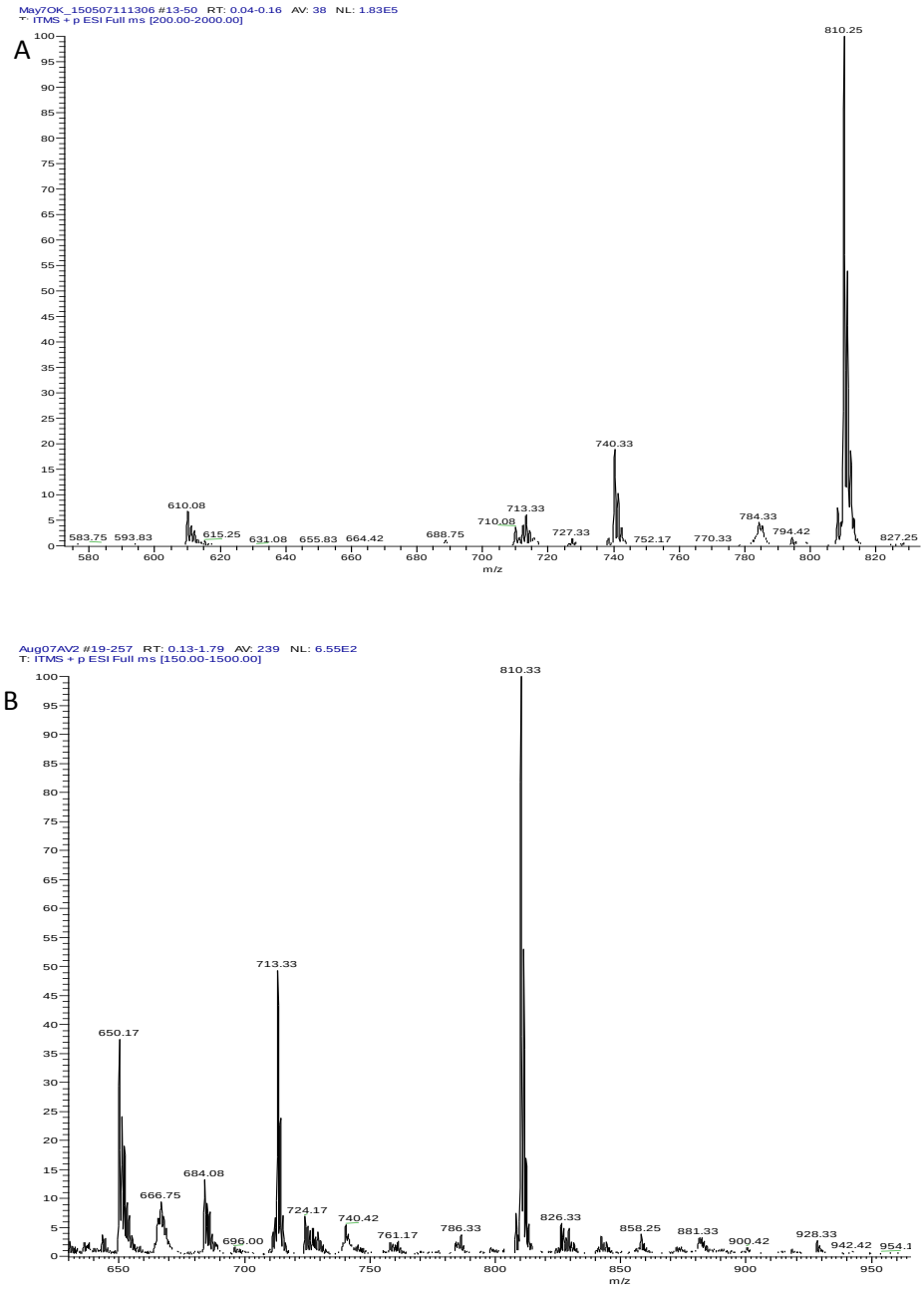

Figure 2.4: Mass spectrometry results of two heme-NHS reactions. Heme-bis-NHS has an expected mass of 810.63 g/mole, the heme-mono-NHS predicted mass is 713.55 g/mole, and free hemin chloride has an expected mass of 651.94 g/mole. Reaction (A) appeared to be more complete than B, since the predominant masses in the spectrum are for the bis and mono heme-NHS adducts, and the free hemin is hardly detectable in A.

2.3.1.2. Heme-NHS modification with functional alkyl labels

Previous work has established that heme can be labeled with a small ligand, N-butylamine. This reaction was used as a standard for the sake of consistency with previous work and to explore the effect of the size of the alkylamine on the heme labeling efficiency. Heme-NBA was produced through the mixing of heme-NHS with NBA in anhydrous DMF for 40 minutes at 100 ^{0}C. The heme analogue produced was mainly the heme-bis-NBA product. This was likely due to the small size of the alkylamine, having small steric hindrance on the bis-product formation (Figure 2.5).

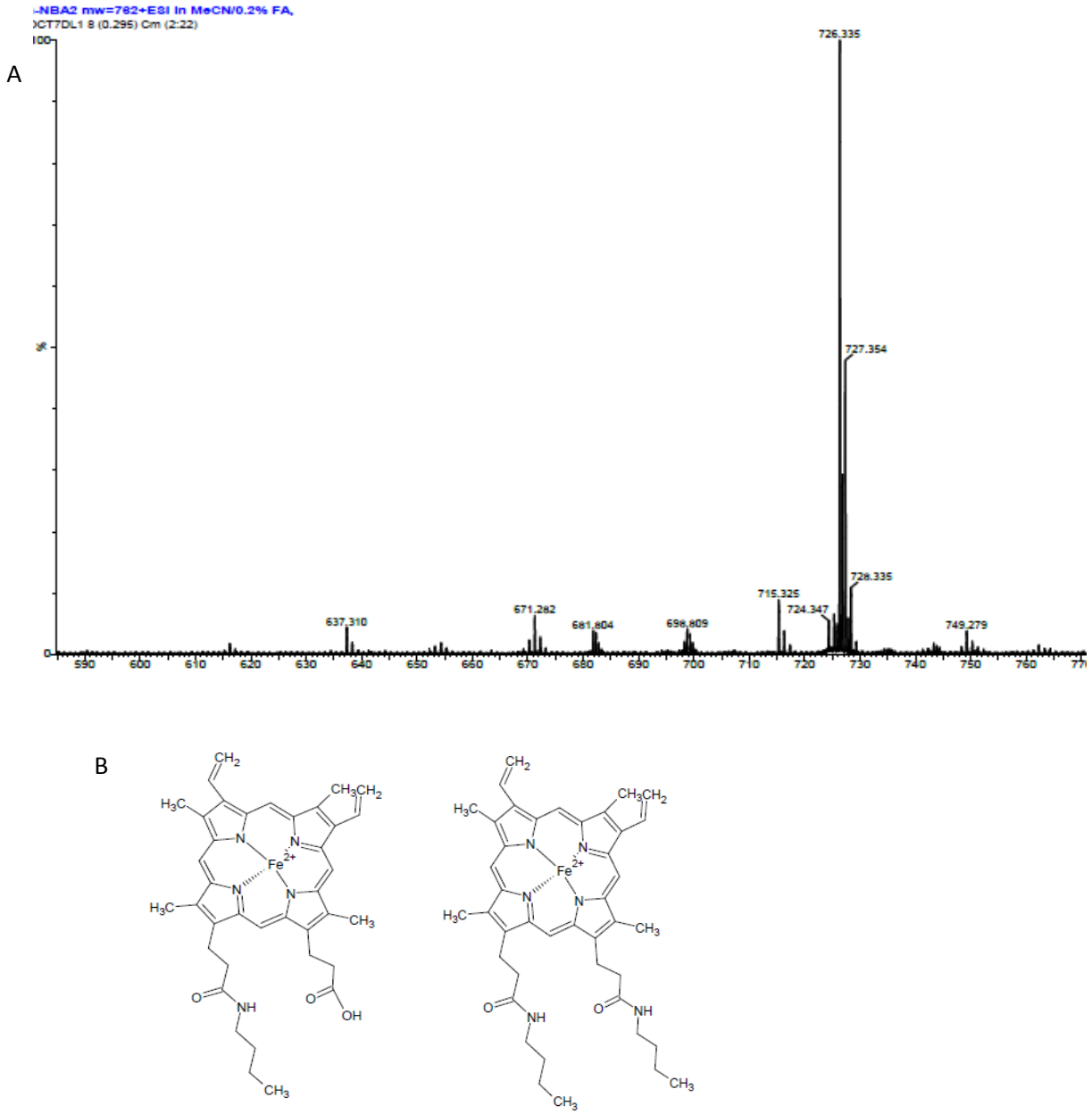

Figure 2.5: MS results of the heme-NHS reaction with N-butylamine (NBA). (A) The heme-mono-NBA substitute could be observed as a small peak with a calculated molar mass of 671.61 g/mol, while the most predominant compound was found to be the heme-bis-NBA analogue with a calculated molar mass of 726.73 g/mol. Structures of the mono- and bis-modified heme are displayed in B.

Attempted reactions to produce heme-bis-OA adduct were conducted, where different equivalents of OA were added to a solution of heme-NHS in DMF and stirred at 100-150 ^{0}C for different time periods (1 - 5 h). Surprisingly, no modified heme was detected in any of these reactions products, with evidence for the presence of the free label, OA (expected mass is 269.51 g/mol), (Figure 2.6.a). The disappearance of the heme adduct peaks could be due to the fact that the free long alkyl chain amine is suppressing the ionization of other compounds in the electrospray field; therefore, attempts to decrease the amounts of the free OA from the product using different scavenger resins were performed. All resins were polystyrene-anchored so they could be filtered out from solution using glass wool after the scavenging experiments were completed. The protocols for the scavenger resins, PS-benzaldehyde and PS-TsCl, were adapted from the protocols reported in the Biotage® products catalog for removing similar amines. According to the intensity of the peak corresponding to the free amine, PS-benzaldehyde resin seemed to bind the free OA more efficiently than the PS-TsCl resin (Figure 2.6.a) consequently it was chosen for all subsequent scavenger resin experiments. In addition, a peak corresponding to the potassium adduct of the heme-mono-OA was detected in the PS-benzaldehyde treated heme-OA (5 h reaction at 115 ^{0}C) (Figure 2.6.b), with no evidence for the formation of the heme-bis-OA. Taking into account that OA is only partially soluble in DMF which might be a barrier that prevents the completion of the reaction, two different experiments were conducted; in the first experiment DMF was replaced by chloroform to enhance the solubility of OA in the reaction solution; however, solvent replacement did not make any difference in the MS results and only heme-mono-OA was observed again. In the second experiment consisted in performing a solid-based reaction in which the heme-NHS was completely melted and sufficient equivalents of OA were then added. The mixture was heated at 100 ^{0}C for an hour, the reaction cooled, and

the produc was then dissolved in hexane and washed twice with DMF. Results of this reaction revealed the formation of relatively higher amounts of the mono adduct in the hexane layer where other heme compounds where detected in the DMF wash, which indicated that the solubilities of the heme-OA analogues are different from free heme and heme-NHS. Therefore, solvent extraction using hexane was performed for early detection of the hydrophobic heme-OA adduct formation based on color change in the hexane layer in addition to TLC and MS analysis. The reason behind the failure in the production of heme-bis-OA could be due to two reasons. Firstly, the length of the alkyl chain in the heme-mono-OA adduct, which is 18 carbons in length, might contribute a larger steric hindrance to the bis-adduct formation due to its greater dynamic conformational size. Secondly, the close proximity of the NHS group in the heme-mono-OA adduct might not be as accessible as in the heme-bis-NHS. In order to examine these two hypotheses, further experimentation with shorter alkylamines and using different heme activation strategies were investigated.

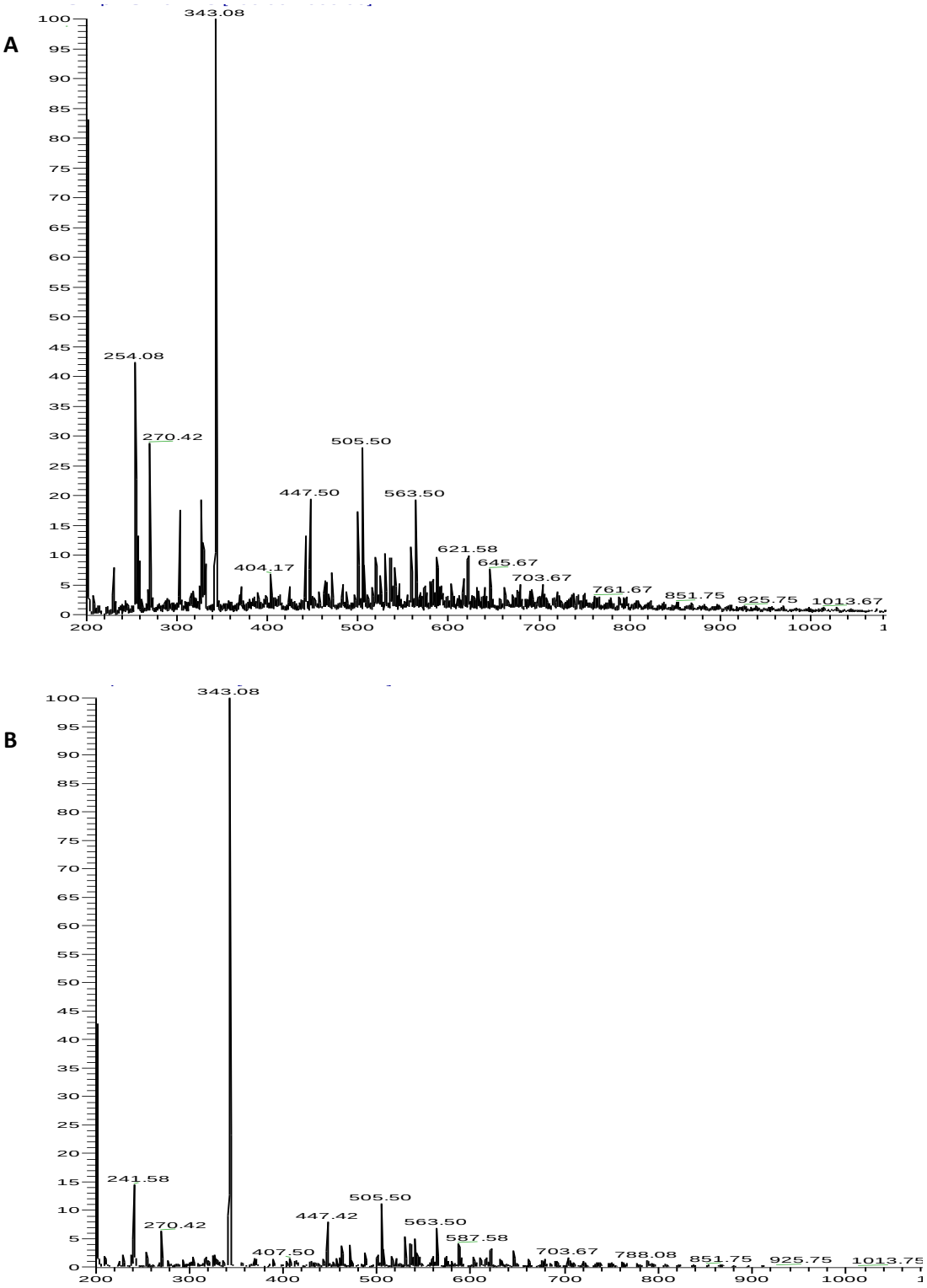

Figure 2.6.a: MS results for heme-NHS reaction with OA. (A) Predominant peaks correspond to free OA expected mass (269.51 g/mol) observed peak 270, and its DMF non-covalent complex (m/z^+= 343). (B) Intensity of free OA signal decreased after PS-benzaldehyde treatment with a little enhancement of the heme product signals.

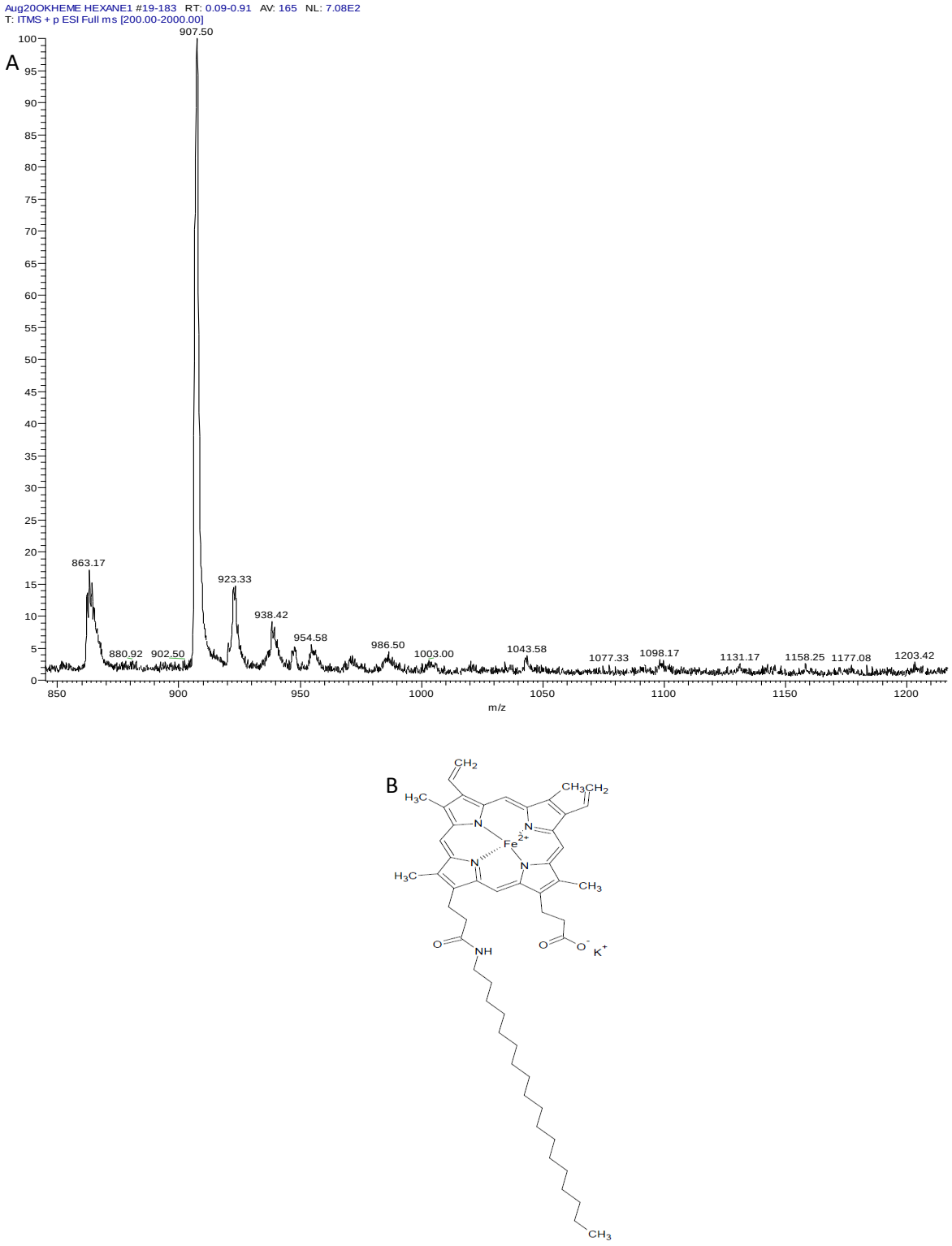

Figure 2.6.b: MS results of the product of one heme-NHS reaction with OA. (A) K^+-heme-mono-OA adduct, expected mass is 906.07 g/mol, detected in the hexane layer of the solid based reaction. Structure of the K^+ adduct is displayed in B.

A reaction of heme-NHS with a shorter amine was necessary to evaluate the efficiency of this heme labeling methodology and to investigate the possibility of producing shorter bis-alkyl heme analogues. Two reactions of heme-NHS with DA for 1 h and 3 h at 100 ^{0}C in the Biotage® Initiator microwave synthesizer were conducted. The MS analysis of both reactions indicated the formation of both mono and bis heme-DA products with characteristic m/z values of 783 and 950 respectively (Figure 2.7), with no significant effect by time variation. In comparison to the OA reaction, heme-DA labeling appeared to be more efficient which indicates that the length of the alkyl chain is of critical importance to the success of such reactions.

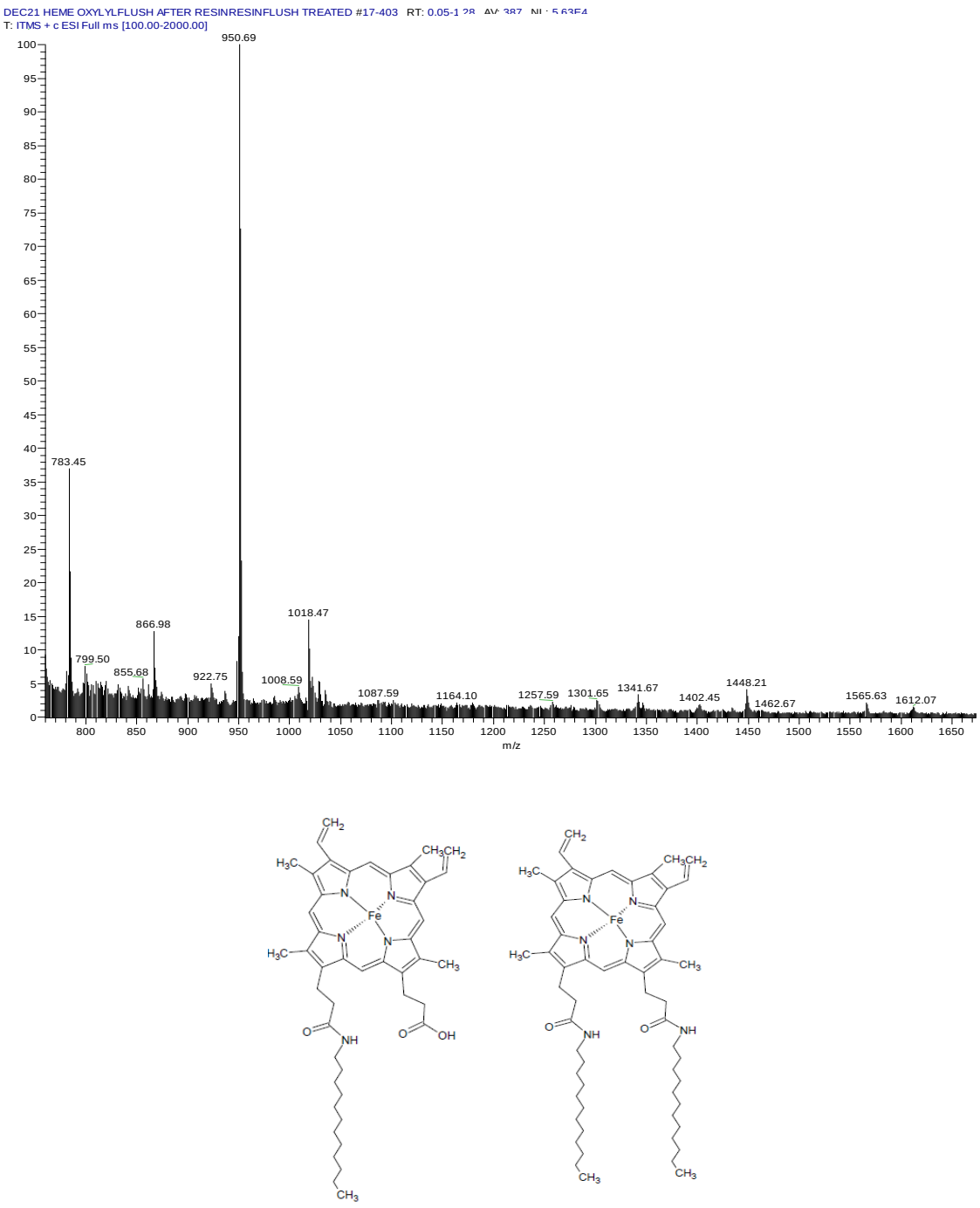

Figure 2.7: MS results of heme-NHS reaction with DA. Both heme-mono- and -bis- DA analogues were detected, expected masses are 783.8 g/mol and 951.1 g/mol respectively. Structures of heme-mono-DA and heme-bis-DA are displayed.

2.3.1.3. Reaction of heme chloride with OA and DA in presence of carbodiimides

Attempts to produce heme-bis-OA through activation of the heme propionate groups using direct carbodiimide activation were investigated. Heme chloride was stirred with EDC and different equivalents of OA in anhydrous DMF or anhydrous pyridine, reaction times and temperatures were applied in different experiments. MS analysis of the results of these reactions showed evidence of formation of the heme-mono-OA adduct and EDC-activated heme (Figure 2.8). Moreover, the intensity of the mass peaks that correspond to the mono-substituted analogue appeared to be larger with pyridine as solvent compared to the reactions where DMF was used as a solvent. This could be due to the enhanced solubility of EDC in pyridine compared to DMF. However, the variation in time and temperature did not have any effect on the reaction. TLC analyses of the various coupling reactions described in this thesis were also undertaken to confirm the MS analyses, and were consistent with the conclusions drawn from the relative mass peak intensities obtained through mass spectrometry. Although the synthesis of heme-bis-OA was reported in the literature using DCC (Figure 2.10) as an activator at 0 ^{0}C,[79] the same procedure was followed with no evidence of the heme-bis-OA formation. Moreover, to investigate the influence of temperature on this reaction, hemin chloride was stirred with DCC in pyridine for 1.5 h followed by addition of OA; the reaction was then stirred at 23 ^{0}C and monitored for 12 days. Aliquots from the reaction were taken on a daily basis and analyzed by MS. The formation of heme-mono-OA with an expected mass of 867.9 g/mol was observed since day 2, but no evidence of the heme-bis-OA until day 7 was obtained, wherein a small peak corresponding to the expected mass of the bis-adduct, 1119.4 g/mol, was detected. The intensity of this signal increased significantly from day 7 to 10; simultaneously, disappearance of the heme-mono-OA adduct signal was noticed during this period of time which indicated that all

heme-mono-OA was converted into the heme-bis-OA analogue. In addition, mass peaks corresponding to free heme, free OA, and mono and fully (bis) heme-DCC activated compounds were observed throughout the reaction, which indicated that the heme does not completely react with DCC and OA. After ten days, significant changes in the reaction solution's odor, color and MS results were observed (Figure 2.8).

Moreover, a reaction of heme with DA in the presence of EDC was conducted to further examine the influence of alkyl chain length. In this case, heating the hemin chloride with excess EDC and DA was sufficient to form heme-mono-DA and heme-bis-DA analogues, which is consistent with the hypothesis of the influence of the alkyl chain length on the degree of completion of such reaction.

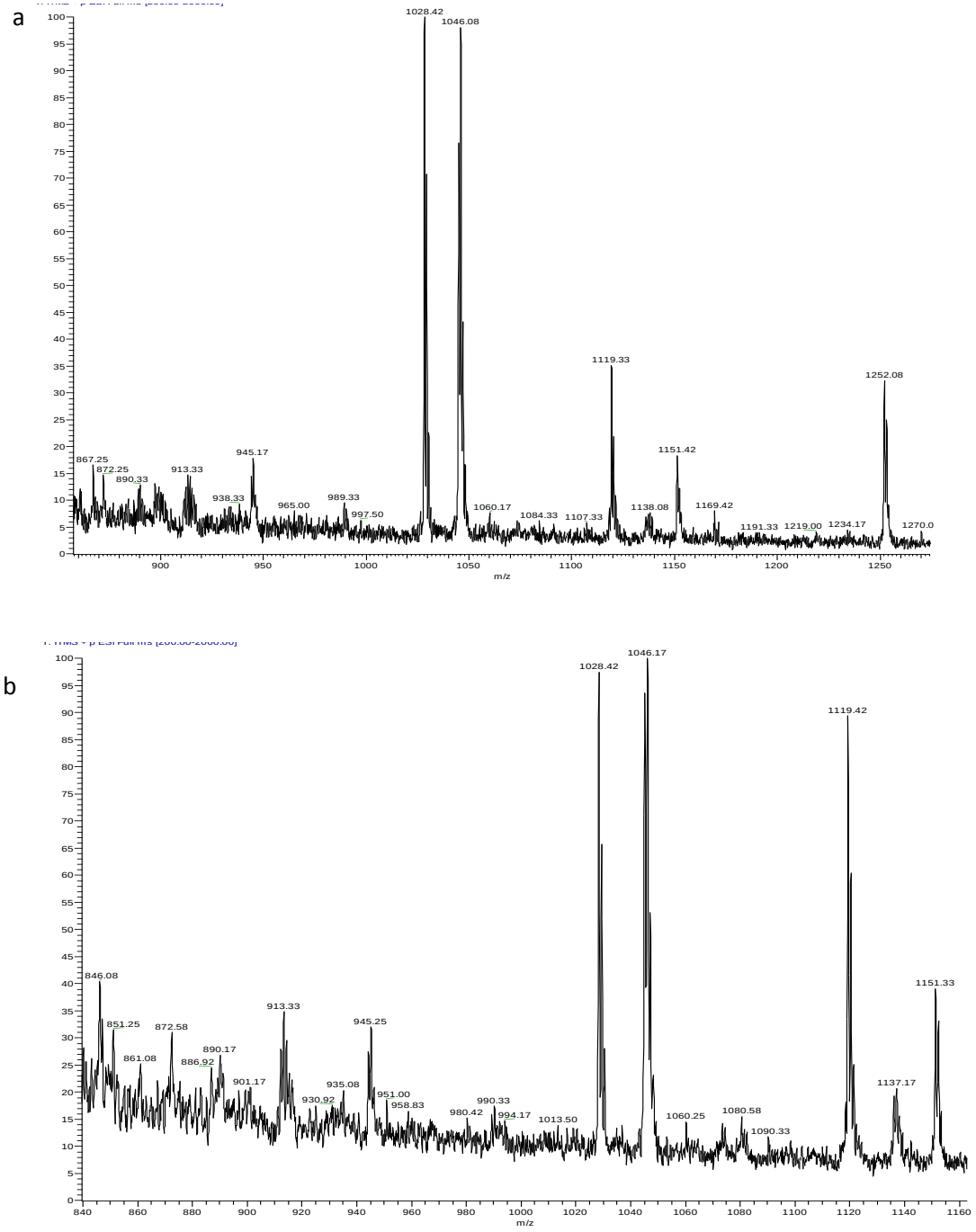

Figure 2.8: MS results of hemin chloride after numerous days with OA in presence of DCC. (a) Reported results for the day 7 of the reaction showed small signals for the heme-mono-OA m/z+(867) and signals for heme-bis-OA m/z+ (1119) whose intensity increased significantly by day 10 (b). Signals corresponding to heme-bis-DCC (1028) and heme-mono-OA +DCC (1046) were detected throughout the analysis.

2.3.1.4. Reaction of hemin chloride with OA and DA in the presence of oxalyl chloride

For further confirmation of the effect on the success of the coupling reaction by the type of leaving group and activation reagent, further experimentation with a smaller activation group, the chloride atom, was conducted (Figure 2.10). The reaction of the heme with oxalyl chloride to form the heme-bis-DA analogue was reported in the literature.[93] The procedure was followed and the MS results indicated the formation of both mono- and bis-DA heme substitution, which is consistent with the published findings;[93] however, the yield of heme-bis-DA appeared to be relatively lower than those of the heme-NHS and heme-EDC. This could be due to the instability of the heme-bis-chloride intermediate since the chloride atom should be more readily replaced by nucleophiles. Similar reactions with OA were conducted, heme-mono-OA was clearly detected in MS results; however, heme-bis-OA related peaks had very low intensity (Figure 2.9). Analyses of these results suggested that the small size of the leaving group could lead to a faster and more complete reaction. However due to the instability of the heme-Cl intermediate, the overall yield of this reaction was very low. Further experimentation of the heme-Cl reaction with OA, and utilizing different conditions in solvent, temperature, and time, could be investigated in order to optimize the reaction conditions.

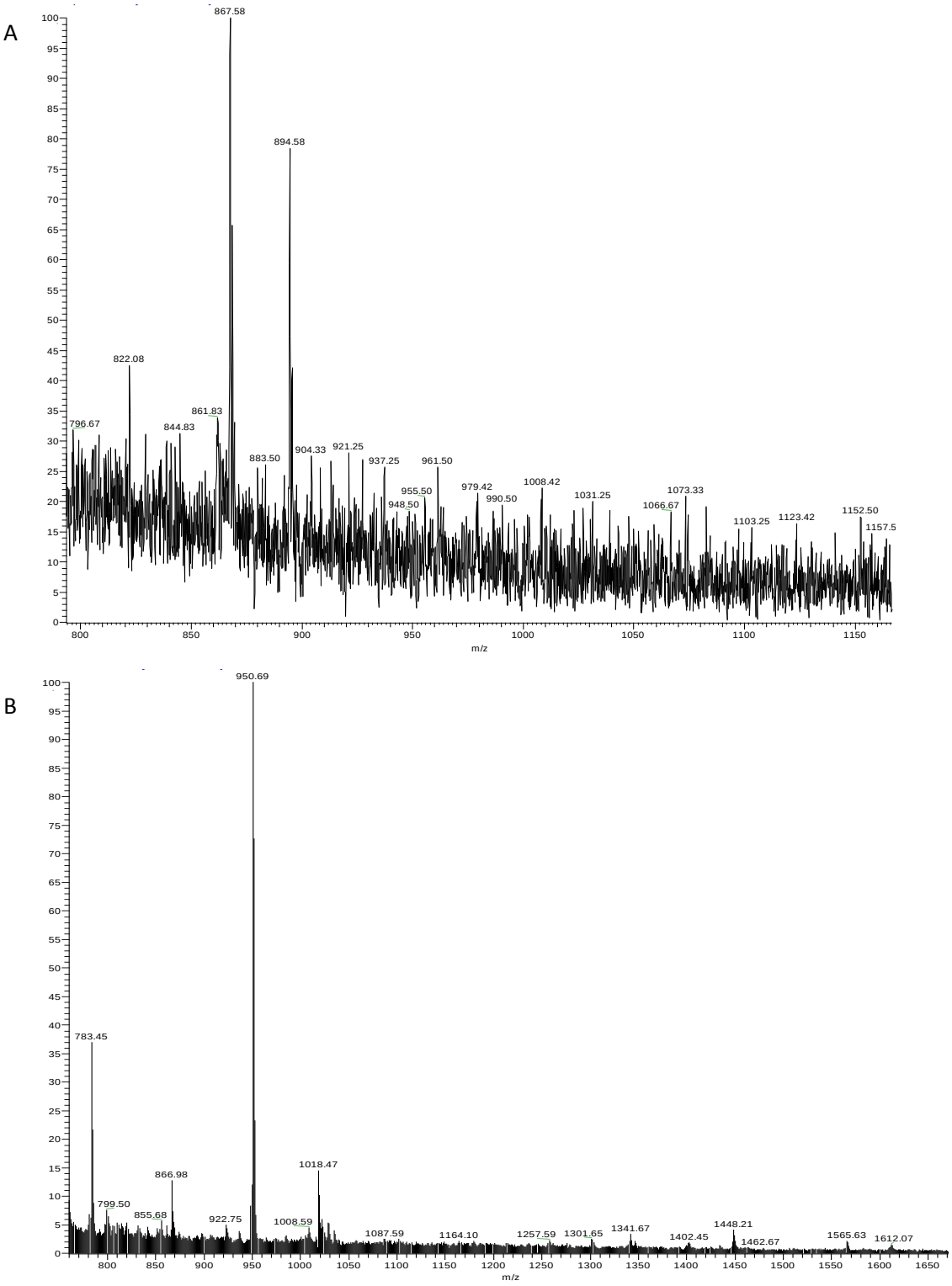

Figure 2.9: Mass spectrometry results of heme-Cl reactions with OA and DA. (A) a clear indication of the formation of heme-mono-OA adduct at m/z 867.58 which matches its calculated MW. (B) MS results of DA labeling reaction showed the successful synthesis of heme-bis-DA at m/z 950.69, and heme-mono-DA at m/z 783.45, predicted MWs for both analogues are 951.1 g/mol and 783.8 g/mol respectively.

Furthermore, the effect of the presence of iron in the porphyrin ring on such labeling reactions was assessed through conducting an experiment in which hemin chloride was replaced by protoporphyrin IX (Figure 2.10), which is an iron-free heme analogue. The results of the iron free analogue reaction in the presence of oxalyl chloride were similar to those of the heme reaction under the same conditions, where only the mono-OA adduct was observed in the PPIX-OA experiment and both of PPIX-mono and bis-DA were detected by MS. This suggested that the presence of Fe^{2+} has probably no effect on the reaction with long alkyl chains.

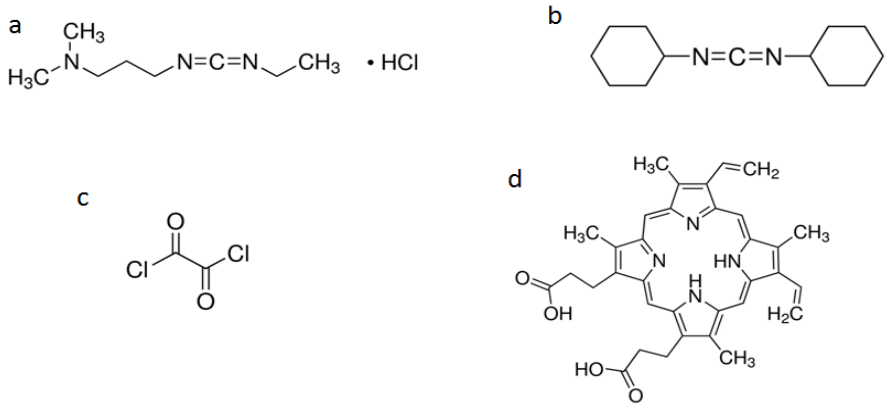

Figure 2.10: Chemical structures of various compounds involved in the synthesis. *N*-(3-Dimethylaminopropyl)-*N′*-ethylcarbodiimidehydrochloride (EDC) (a), dicyclohexylcarbodiimide (DCC) (b), oxalyl chloride (c), and protoporphyrin IX(d).

2.3.2. Purification of heme-DA analogues

A Biotage® KP-SIL SNAP column was used to purify heme-DA adducts. Samples were dissolved in a small volume of methylene chloride and introduced to the column on a Biotage® KP-SIL samplet. The conditions used were based on TLC experimentation performed in a 9:1 chloroform:methanol mixture. Fractions that showed high absorbance at 280 nm were collected and analyzed by MS and the previous conditions were found to allow the efficient separation of the heme-DA analogues from other reaction components. In an attempt to separate the bis-heme-

DA from the mono-heme adduct several conditions were investigated; such as, 9:1 methylene chloride: methanol and 100% ethyl acetate. In addition reversed phase chromatography using a Biotage® KP-C18 SNAP column using 100% methanol and a 1:1 methanol:ethyl acetate mixture in two different experiments. Both bis- and mono-heme-DA were observed to elute at the same time due to the high similarity in structure and low polarity of both compounds, which have made the separation quite challenging (Figure 2.11).

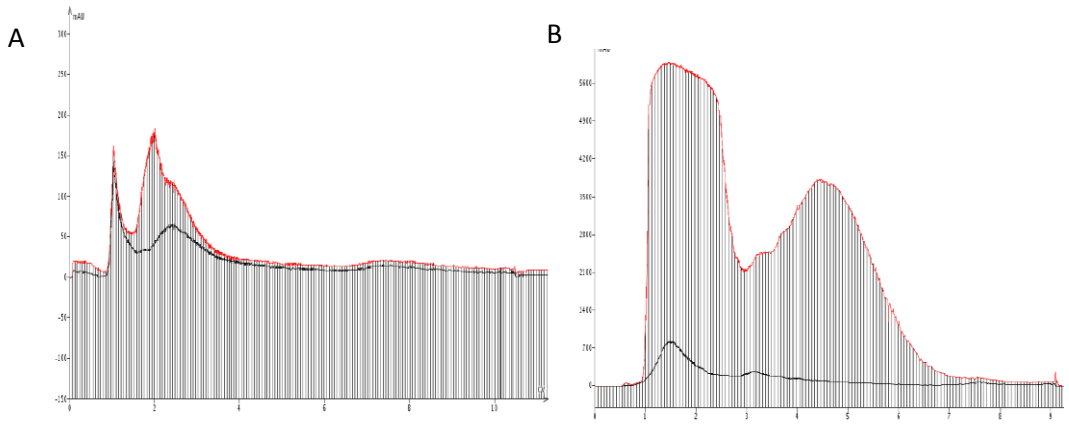

Figure 2.11: Fraction reports obtained from Biotage® Isolera chromatography system for purification of DA reaction mixtures with heme-NHS (A) and with hemin chloride in the presence of EDC (B) based on TLC conditions 9:1 methylene chloride: methanol. MS results of first peak fractions detected a mixture of mono and bis-heme DA adduct, whereas the second peak contained a mixture of free hemin, heme-mono-NHS and heme-bis-NHS along with some heme-DA analogues in A, and heme mono and bis EDC activated compounds in B.

2.3.3. Attempts for incorporating heme-DA analogues into the His6-Bfr cage

Attempts for incorporating the modified heme involved incubating the apo-His6-Bfr Bfr with heme-DA analogues at 80 °C for 10 minutes, after which the mixture was then allowed to cool to room temperature. This methodology has been previously used by Anton van der Ven to incorporate different heme analogues into the Bfr structure.[80] The added heme analogues were dissolved in either DMF or DMSO and then added to the buffered His6-Bfr solution. Precipitation of heme-DA analogues was observed upon the addition of DMF or dimethyl

sulfoxide (DMSO) to the protein sample, which made the incorporation of these hydrophobic analogues a challenging task. The success of incorporation was investigated by monitoring the change in the UV-Vis absorbance profile of the Bfr protein. The successful incorporation of the heme to the Bfr cage protein could be detected through the detection of the heme Soret band at around 420 nm in addition to the protein absorption signals at around 280 nm. However, in both trials no changes in the Bfr UV-Vis absorption profile were detected (Figure 2.12). Although DMF and DMSO are very compatible with the buffered protein samples, the precipitation of the heme-analogues out of solution upon their addition to the aqueous protein environment could prevent their introduction to the Bfr cage.

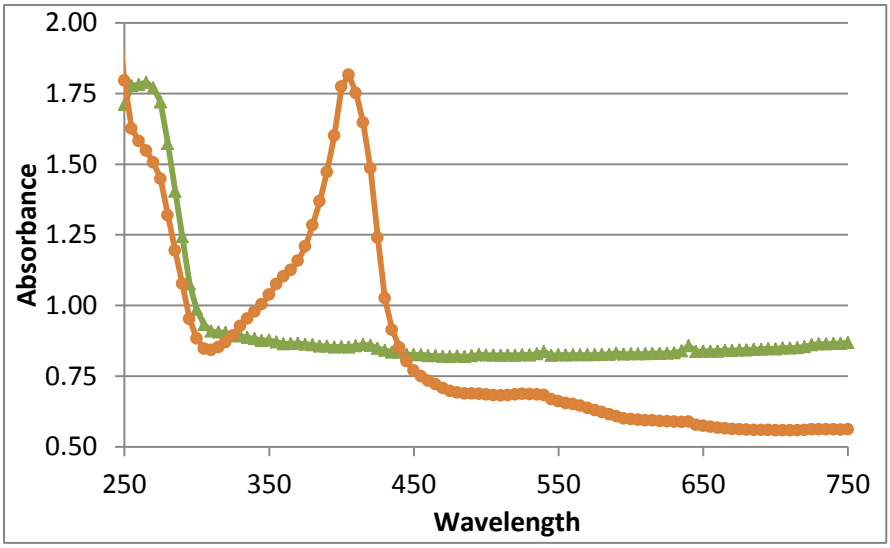

Figure 2.12: UV absorption spectra obtained for hemin (orange) and heme-DA (green) His6-Bfr incorporation experiments. A control experiment of incorporating hemin in 0.2 MES buffer and 5% DMSO was analyzed and the heme Soret band at 420 nm was observed, in contrast in the heme-DA analogue incorporation experiment, no heme signal was detected at 420 nm.

2.4. Conclusions

The results presented in this chapter indicate that the modification of heme with long alkyl chain labels is possible. The activation strategy followed to activate the heme propionate groups and the length of the added alkyl chains were found to affect the success of such reactions. In regard to the Bfr hydrophobic engineering approach that we are investigating, although we were able to synthesize and purify heme-DA analogues, the poor aqueous solubility of these analogues prevented their incorporation into the His6-Bfr cage protein.

3. Chapter 3: Encapsulation of Hydrophobic Guest Molecules within the His6-Bfr Cavity.

3.1. Introduction

Many chemotherapeutics are small molecular weight compounds which frequently have poor solubility in water. Poor water solubility can limit their therapeutic effects. During the past century, numerous studies aimed to optimize the therapeutic benefits of drugs while circumventing their systemic toxicity have been developed through the use of micellar drug systems (MDS) (Figure 3.1). The functional unit of a micellar drug carrier is the amphiphilic molecule; a molecule that has polar groups as well as nonpolar portions. These amphiphilic molecules are known to self-assemble into defined structures when exposed to solvents. In aqueus solutions, amphiphilic molecules pack in a way that expose their polar groups to the hydrophilic environment, while their hydrophobic portions are oriented away from the solvent, forming what is known as a regular micelle. Different types of amphiphilic molecules have been investigated as drug carriers and range from conventional surfactants to amphiphilic polymers.[94] For example, a particular class of surfactant known as gemini surfactants, a surfactant containing two head groups that are connected by a linker, have attracted rigorous biological as well as biomedical interest as gene delivery platforms.[95,96] Micellar drug delivery systems have several advantages; such as, simple preparation, increased drug solubility, increased circulation time coupled with reduced toxicity, enhanced tissue penetration and tissue targeting. However, they still have some limitations such as the systemic instability over long time periods, and the need for individualized system optimization for each drug.[97] These limitations have resulted in an inadequate sustained drug release provided by such nanocarriers. Several approaches were investigated in order to address the issue of poor sustained drug release from micellar nanocarriers; some of those approaches will be discussed below.

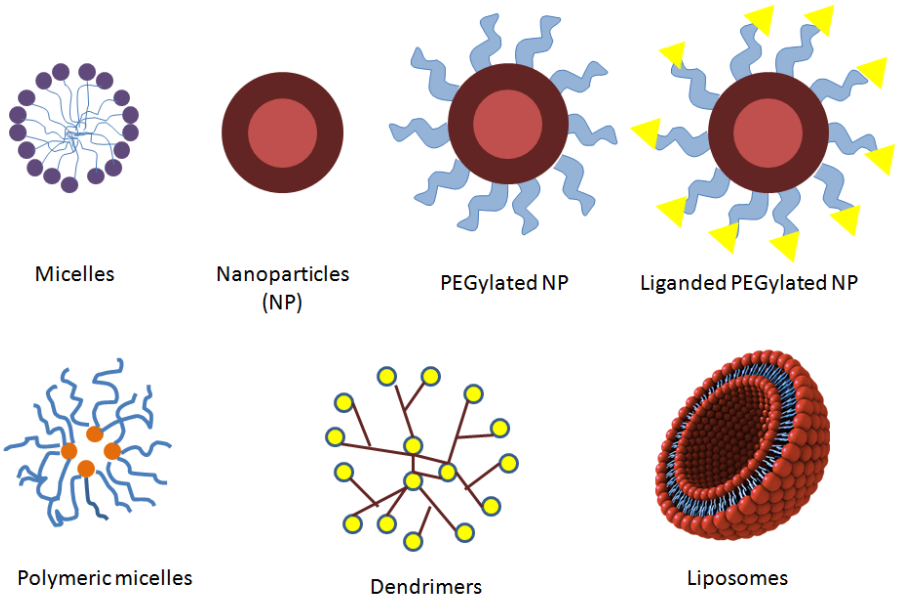

Figure 3.1: Structural illustration of some types of drug nanocarriers. This figure was modified from reference 97.

3.1.1. Strategies for improved sustained drug release from micellar structures

There have been several approaches toward optimizing drug release from micellar delivery systems; one of which has involved the encapsulation of prodrugs within the micelle core instead of using the drug in its free active form. In this case the conversion of the prodrug to an active drug in addition to the time required for micellar dissolution will increase drug retention levels. An example of this approach is the use of paclitaxel palmitate, a prodrug for paclitaxel, which was encapsulated in polyethylene glycol-*b*-polycaprolactone (PEG-*b*-PCL) micelles and exhibited an approximate 4-fold improvement in drug retention time in serum relative to paclitaxel itself, and also exhibited a better antiproliferative effect against cancer cells.[98] The formation of drug-polymer conjugates is another effective strategy used to improve MDSs, which usually involves the conjugation of a drug to the hydrophobic portion of the amphiphilic polymer.[97] Applying this strategy, Yoo and Park were able to conjugate doxorubicin

(DOX) to PLGA-PEG micelles and form an effective MDS.[99] Moreover, amphiphilic block copolymers have shown promising potential for hydrophobic drug delivery; for instance, Pathak and coworkers have recently reported a PEG-based polyaspartic acid peptide-poly(ethylene glycol)-poly(ε-caprolactone) NP which was an excellent carrier for curcumin, a hydrophobic compound with reportedly high activity against bone metastasis, and exhibited good retention time, lower blood coagulation risks and higher antitumor activity.[100] Other researchers have combined amphiphilic polymers with different structures to design novel polymeric MDSs; examples are the conjugation of copolymers with lipids[101] and polyaminoacids.[102] In addition, oligopeptides have been used to prepare MDS for doxorubicin delivery, and their efficacy and toxicity were examined and compared to DOX; these more complex systems were found to have better anticancer effects with lower cytotoxicities.[103] Another interesting class of amphiphilic-based nanoparticles are the liposomes which are usually formed via self-assembly of phospholipids after dispersion in aqueous solvents. Liposomes have been utilized as drug carriers for both hydrophilic and hydrophobic drugs. The unique self arrangement of liposomes allows for hydrophobic drugs to be combined to the hydrophobic membrane bilayers during the liposome formation, while the aqueous core can serve as a reservoir for hydrophilic therapeutics.[104] Despite the promising development in the design of MDSs, further progress toward longer sustained release and higher safety and tolerability is needed.

In this chapter, previously discussed nickel-mediated affinity interactions between His6-Bfr and guests carrying NTA functionalities will be utilized for the encapsulation of micellar structures within the cage protein cavity. Such encapsulation could increase the versatility of the Bfr cage protein for delivering hydrophobic theranostics to their targets, as well as provide a protected environment for the encapsulated micelles, which could improve the retention time of

the encapsulated drugs. Attempts to engineer the hydrophobicity of the inner cavity of the Bfr cage protein are of fundamental as well as practical interest towards potential molecular delivery applications. The encapsulation of two different amphiphilic guest molecules, 1,2-dioleoyl-*sn*-glycero-3-[(N-(5-amino-1 carboxypentyl) iminodiacetic acid)succinyl] (nickel salt) (DGS-NTA(Ni) and nonadecanoyl-NTA (ND-NTA), within the His6-tag Bfr cage protein will be outlined and discussed; and the micellar structures formed by these amphiphilic molecules under different conditions will be investigated. Molecular modelling on the fully extended ND-NTA indicated a length of 45 Angstroms which is the approximate radius of the interior cavity of Bfr; therefore ND-NTA would be the best first choic of fatty acids. The synthesis of single chain fatty acid-NTA, nonadecanoic-NTA, and His6-tag Bfr preparation and purification will be discussed in this chapter as well.

As described earlier in Chapter 1, the His6-tag Bfr capsule protein contains 24 hexahistidine tags which have been engineered onto the internally exposed C-termini of Bfr. These tags have been utilized successfully as specific affinity labels for encapsulation of guest molecules decorated with NTA functionalities. ProQ® sapphire 365 oligohistidine stain, Streptavidin labelled with fluorescein and 1.8 nm and 5 nm gold nanoparticles (AuNP)[80] are examples of NTA-containing guest molecules that have been successfully introduced to the His6-tag Bfr cavity by Dr. Honek's graduate students. As there are 24 subunits that compose the quaternary structure of His6-tag Bfr, we aimed to utilize all 24 His6-tags toward introducing different kinds of fatty acid-based guest molecules into the Bfr cavity. For example, encapsulation studies of a micellar structure consisting of saturated single chain NTA-fatty acids (Figure 3.2), and different concentrations of non-saturated NTA lipid were performed in order to investigate the behavior of the Bfr cage protein toward such alterations.

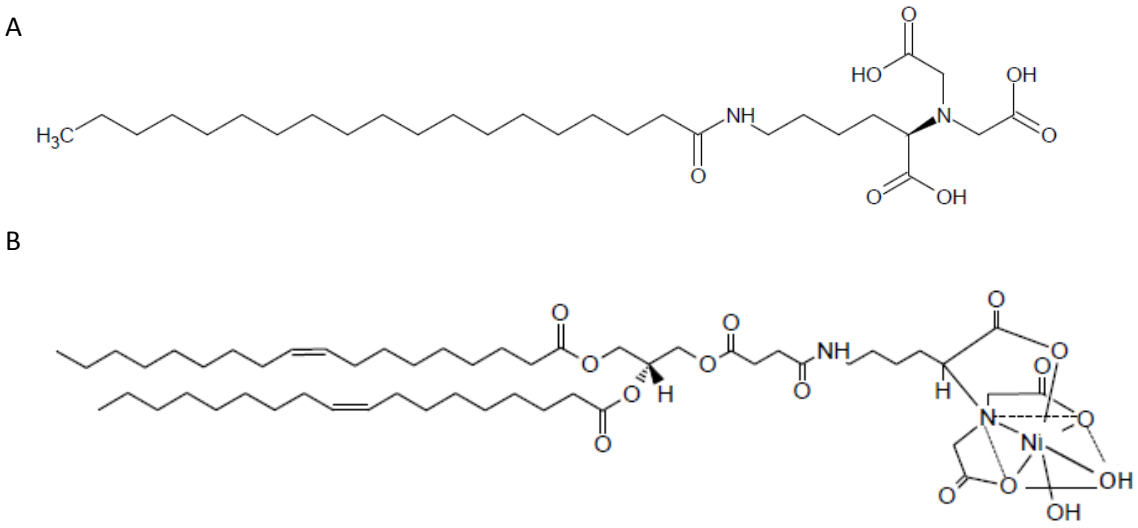

Figure 3.2: Structures of fatty acids involved in the His6-Bfr encapsulation studies. (A) Nonadecanoyl-NTA (C19-NTA). (B) A commercially available 18:1 DGS-NTA(Ni), 1,2-dioleoyl-*sn*-glycero-3-[(N-(5-amino-1 carboxypentyl) iminodiacetic acid)succinyl] (nickel salt) from Avanti Lipids, Incorporated.

Four methods would be utilized to confirm the encapsulation of the micellar guests within the His6-Bfr: size exclusion chromatography (SEC), mass spectrometry, pyrene fluorescence, and transmission electron microscopy (TEM). Pyrene is a unique hydrophobic probe whose fluorescence spectrum has been previously used to characterize ND-NTA micelles,[105] thus the encapsulation of pyrene-preloaded micelles can be detected through monitoring pyrene emission spectra. In addition to fluorescence analysis, TEM was pursued to characterize encapsulated micelles within the His6-Bfr cavity. Negative staining was performed using two types of stains; in this technique, the negative stain will create a layer in which protein structures will be embedded. According to the size of the stain molecules, some stains, atomic stains in particular, will penetrate through the pores of the protein shell and accumulate within its cavity. This methodology was previously utilized to confirm the encapsulation of guest molecules; such as AuNP and streptavidin within the Bfr lumen, since the presence of guest

cargos in the protein interior would exclude stain from the centre of the protein cage, and the absence of stain could be visualized and compared to the images of an empty protein cage.

In addition to the previously listed analysis techniques, dynamic light scattering (DLS) would be employed to estimate the size of the engineered micelles under encapsulation conditions but in the absence of Bfr, and also utilized to investigate changes in the size of the His6-Bfr cage proteins after encapsulating different cargos.

3.2. Experimental

3.2.1. Materials

All materials used in this section of the thesis are listed below otherwise they have been listed in Chapter 2.

Nonadecanoic acid (NA) was purchased from Sigma Aldrich (Milwaukee, WI, USA), N_{α},N_{α}-bis(carboxymethyl)-*L*-lysine hydrate (lysine NTA) (Sigma-Aldrich, Buchs, Switzerland, 1,2-dioleoyl-*sn*-glycero-3-[(N-(5-amino-1 carboxypentyl) iminodiacetic acid)succinyl] (nickel salt) (DGS-NTA(Ni|) (Avanti Polar Lipids, AL, Alabama), Carbon 400 mesh, Cu Grids (Canemco-Marivac, Gore, QC, Canada), Molybdic acid ($(NH_4)_6Mo7O_{24}$) (Sigma-Aldrich, Saint Louis, MO, USA), Phosphotungstic 39 acid ($H_3PW_{12}O_{40}$) (Sigma-Aldrich, Saint Louis, MO, USA), All buffers were made with Milli-Q^{TM} water with 18 MΩ cm^{-1} resistivity and filtered through a 0.45 μm cut-off membrane. High purity pyrene was obtained from Dr. Duhamel's laboratory.

3.2.2. Safety statement

Lab coat, gloves and protective glasses were used throughout all the experiments. Bacterial cultures were handled with extensive care and included working next to the flame and bleaching all the tools and glassware that came in contact with the bacteria. Experiments involving the use of organic chemicals like ethyl acetate or pyrene were performed in the fume hood and handled with extreme caution.

3.2.3. Protein expression and purification

Lysogeny broth (LB, 2 mL) containing ampicillin (30 μg/mL) was inoculated with a single colony of *Escherichia coli* BL21 culture with the *E. coli* Bfr gene engineered to have a C-terminal His-tag contained on a plasmid.[80] The mixture was shaken overnight (37 ^{o}C, 200 rpm), then added to 1.5 L of the liquid media containing ampicillin (30 μg/mL). After the culture reached its mid-log phase (optical density (OD) = 0.6-1.0), solid isopropyl-β-D-1-thiogalactopyranoside (IPTG) was added to a final concentration of 1 mM to induce expression of the recombinant Bfr. Cells were shaken for four additional hours and then harvested by centrifugation at 17700*g* for 10 minutes. Cells were resuspended in Tris buffer (50 mM Tris, 100 mM NaCl, pH 8.0) and then lysed utilizing a cell homogenizer (Avestin EmulsiFlex-C5). The resulting solution was spun down at 12000*g* for 20 minutes and the supernatant was collected. The supernatant was heat shocked at 70 ^{o}C and held at that temperature for 10 minutes, then left to cool to room temperature then centrifuged again at 12000*g* for 20 minutes. The supernatant was then collected for purification. The His6-tag containing Bfr was purified using a 1 mL GE His Trap^{TM} affinity column. The equilibration buffer was 50 mM Tris, 100 mM NaCl, and 20 mM imidazole, at pH 8.0, while the elution buffer used was 50 mM Tris, 100 mM NaCl, and 300 mM imidazole, at pH 8.0. The eluted proteins were analyzed using a 15% sodium dodecyl sulfate polyacrylamide gel electrophoresis (SDS-PAGE) gel and MS. Column fractions containing the desired protein were pooled and concentrated using an Amicon filtration apparatus with a molecular weight cut-off membrane of 10 kDa.

3.2.4. Synthesis of nonadecanoyl-NTA (ND-NTA)

The procedure for ND-NTA production was adapted from reference 105. Nonadecanoic acid (NA) (1 g, 3.3 mmol) and NHS (0.5 g, 4.9 mmol, 1.5 equiv.) were dissolved in dichloromethane (CH_2Cl_2, 50 mL) followed by the addition of 1-ethyl-3-(3-dimethylaminopropyl)carbodiimide (EDC)-HCl (0.9 g ,4.9 mmol, 1.5 equiv.) The reaction was stirred for 24 h and then diluted with water (50 mL); the organic and aqueous phases were separated (Scheme 3.1). The aqueous phase was extracted 3 times using CH_2Cl_2 (20 mL). Organic phases were collected, washed with brine solution (50 mL), dried over anhydrous Na_2SO_4, filtered and concentrated under reduced pressure. The concentrated product was then recrystallized from hot ethyl acetate (EtOAc; 30 mL) to obtain a 0.8 g, 80 % yield, white powder of nonadecanoyl-NHS with a calculated molecular mass of 395.57 g/ mol (Scheme 3.1).

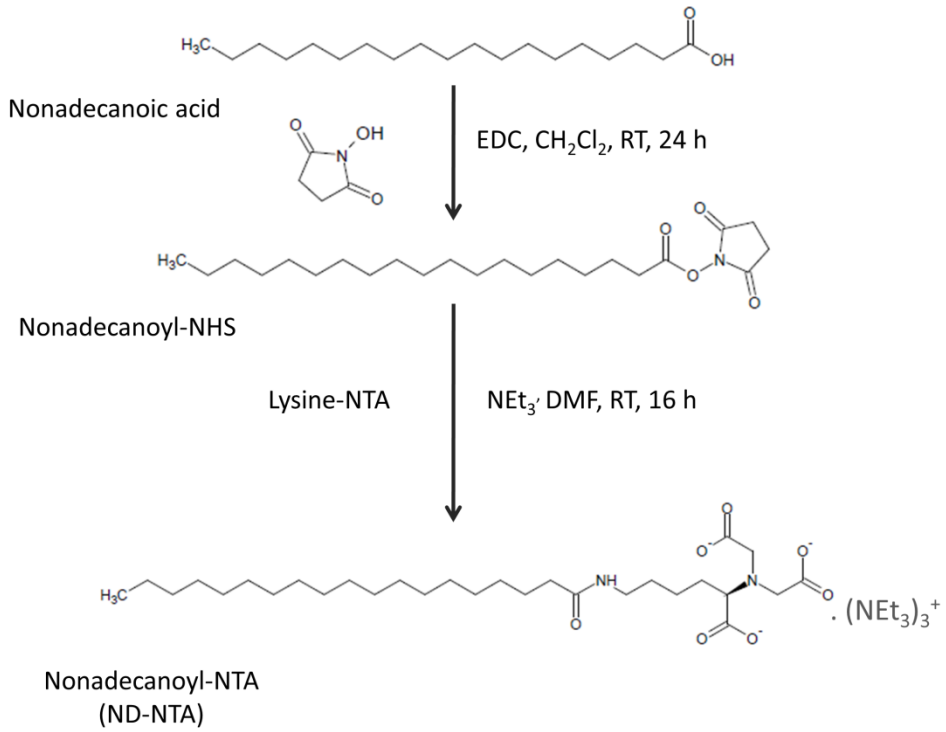

Scheme 3.1: Nonadecanoyl-NTA synthesis.

Nonadecanoyl-NHS (0.8 g, 2.02 mmol), N_α,N_α-bis(carboxymethyl)-*L*-lysine hydrate (lysine NTA) (0.5 g, 2.02 mmol, 1 equiv.) and triethylamine (NEt_3) (1.9 ml, 14.14 mmol, 7 equiv.) were dissolved in dry DMF (30 mL) and left to stir for 48 h at room temperature. The solvent was then evaporated and the residue was taken up in water (70 mL), acidified with 1 N HCl until precipitation started. Then the solution was stirred for one hour. The resulting suspension was then filtered and the white powder (0.7 g, 1.2 mmol, 70%) was dried under vacuum. The product, ND-NTA was analyzed with mass spectrometry and proton nuclear magnetic resonance (^{1}H NMR) for chemical structure verification and purity. Micellar aqueous solutions of ND-NTA with different concentrations were prepared through raising the pH to 12 through dropwise addition of 1 N solution of NaOH. pH was then lowered to 8 by addition of 1 N HCl. An aliquot (60 µL) of each solution was analyzed with DLS to explore the size and behavior of the ND-NTA micelles in different solvent conditions.

3.2.5. Encapsulation studies

3.2.5.1. Encapsulation of ND-NTA micelle into His-6 Bfr

ND-NTA (2 mg, 3.6 x 10^{-6} mol, 200 equiv.) was added to His6-Bfr (1.89 x 10^{-9} mol, 1.0 equiv.) in 1 mL of 8 M guanidine hydrochloride (GdnHCl) buffered with 50 mM Tris, 100 mM NaCl at pH 8.0 along with nickel sulfate (4.5 x 10^{-6} g, 2.93 x 10^{-8} mol, 8.0 equiv.) and hemin chloride (1.9 x 10^{-5} g, 2.93 x 10^{-8} mol, 8 equiv.). This solution was kept for 90 minutes at 5 °C and was then dialyzed against 2 L of 50 mM Tris 100 mM NaCl buffer at pH 8.0 at 5 °C for 24 h. The sample was concentrated with a Pall Nanosep® spin column with a 10 kDa cut off to a volume of 0.250 mL. Encapsulated ND-NTA micelles were purified using a GE Sephacryl™ S-300HR resin, with a void volume of 99.05 mL, and running flow rate of 0.5 mL/min, collecting fraction volumes of 1 mL. The running buffer was the same as the dialysis buffer. The first peak

(24-mer Bfr) was collected, concentrated to 0.5 mL and analyzed using SDS page gel and MS, and viewed under TEM.

3.2.5.2. Encapsulation of DGS-NTA(Ni) within His6-Bfr

DGS-NTA(Ni) (0.95 mg, 9.07 x 10^{-8} mol, 48 equiv.) was added to His6-Bfr (1.89 x 10^{-9} mol, 1.0 equiv.) in 1 mL of 8 M GdnHCl buffered with 50 mM Tris, 100 mM NaCl at pH 8.0 along with hemin chloride (1.9 x 10^{-5} g, 2.93 x 10^{-8} mol, 8 equiv.). The mixture was kept for 90 minutes at 5 °C before being dialyzed against 2 L of 50 mM Tris 100 mM NaCl buffer at pH 8.0 at 5 °C for 24 hours. The sample was concentrated with a Pall Nanosep® spin column with a 10 kDa cut off to a volume of 0.5 mL. Similarly, encapsulated DGS-NTA(Ni) was purified using a GE SephacrylTM S-300HR resin, void volume of 99.05 mL, running flow rate was 0.5 mL/min, collecting fraction volumes of 1 mL. The running buffer was the same as the dialysis buffer. The second peak was collected, concentrated to 0.5 mL and analyzed with SDS page gel and MS, and viewed under TEM.

3.2.6. TEM preparation and imaging

Transmission electron microscopy experiments were performed on a CM10 Philips microscope modified with an Advanced Microscopy Techniques image capturing CCD camera. A 100 keV acceleration potential was used for imaging in bright field mode. A 400 mesh copper grid with a carbon-formvar coating was used to perform TEM imaging on the encapsulated ND-NTA micelles. The optimum Bfr staining technique was previously established by Anton van der Ven[80]; two negative staining solutions were used to generate the contrast needed to visualize the protein: 0.5 % molybdic acid ($(NH_4)_6Mo_7O_{24}$), and 0.5% phosphotungstic acid ($H_3PW_{12}O_{40}$). Encapsulated Bfr samples were prepared to a concentration of approximately 0.5 mg/mL. Grid preparation started by placing a 20 μL droplet of protein sample, two 20 μL droplets of water and

one 20 µL droplet of stain on Parafilm®. The grid was placed on top of the sample droplet for one minute, then it was removed, dabbed with a piece of Whatmann No 1 paper to remove most of the liquid from the grid except for a thin glassy layer of solution. This was then washed by dipping the grid into the two water droplets as in the previous step without the minute wait time. Finally, grids were dipped onto the staining solution; excess stain was dabbed away until a thin glassy layer of solution coating the grid was left. Grids were covered and left at room temperature to dry for 24 h.

3.2.7. MS experimentation

All protein samples were buffer exchanged for water using Pall Nanosep® 10 kDa cut-off spin columns and then diluted to a final concentration of 1-5 µM in a 50 µL solution of a 1:1 water: MeCN mixture with 0.2% formic acid or a 1:1 water:MeOH mixture with 0.1% formic acid and a 1:1 water:MeCN mixture with 0.5% NH_4OH for samples containing DGS-NTA(Ni). Protein samples were run on a Thermo Scientific Q-Exactive™ mass spectrometer. Spectra were collected between 100-2500 m/z and the supplied MaxEnt-1 MassLynx softwareA was used to deconvolute the protein mass.

3.2.8. DLS sample preparation

Samples for DLS analysis were first centrifuged at 7650g for 10 minutes and then filtered through Acrodisc syringe filters with a 0.2 µm membrane cut off. A volume of 60 µL of each sample was transferred to a Hellma Precision Quartz cell and finally submitted to Malvern Zetasizer Nano ZS system for analysis.

3.2.9. Fluorescence spectroscopy studies using pyrene

A stock solution of pyrene (2×10^{-4} M) was prepared in acetone. Two 10 µL aliquots of pyrene solution were transferred into two empty vials and the solvents were evaporated at 37 ◦C for 1 h. After evaporation, one vial was filled with 1 mL of ND-NTA (2 mg/mL) in Tris buffer (50 mM Tris, 100 mM NaCl) at pH 8.0 and gently stirred overnight at room temperature to ensure pyrene incorporation into the micelles. The other vial was used to perform the control experiment, where it was filled with 1 mL of 50 mM Tris and 100 mM NaCl buffer at pH 8 and allowed to stir overnight. These two solutions were then mixed with His6-Bfr, hemin chloride and $NiSO_4$ and two separate encapsulation experiments were undertaken as described earlier in this chapter. Samples were purified as before employing a GE SephacrylTM S-300HR resin, a void volume of 99.05 mL, a running flow rate of 0.5 mL/min, and collecting fraction volumes of 1 mL. Samples were concentrated to 1 mL for fluorescence spectroscopy analysis using a QuantaMaster instrument from Photon International Technology; a volume of 0.5 mL from each sample was transferred to Hellma Precision Quartz cell. Samples were excited at λ= 335 nm and pyrene emission spectra were recorded from 350 nm to 600 nm. Slit widths for the incoming and the emission light were set to 1 mm. Results were exported with PTI FeliX32 software and analyzed on Microsoft Office Excel 2010.

3.3. Results and Discussion

3.3.1. His6-Bfr purification

A 1 mL GE His Trap™ affinity column was used to purify the His6-Bfr protein, and the supernatant from the homogenized cells was injected into the above the column. To determine the purity of the protein, fractions were examined using SDS-PAGE gel electrophoresis (Figure 3.3 A) and fractions with higher purity were collected, pooled and concentrated using an Amicon stirred cell pressure concentrator with a Millipore Ultrafiltration membrane with a molecular weight cut off of 10 kDa. Protein samples were analyzed using a Thermo Scientific Q-Exactive™ mass spectrometer to confirm the molecular mass of the protein (19559 Da), whereas the calculated mass was 19560 Da (Figure 3.3, B&C).

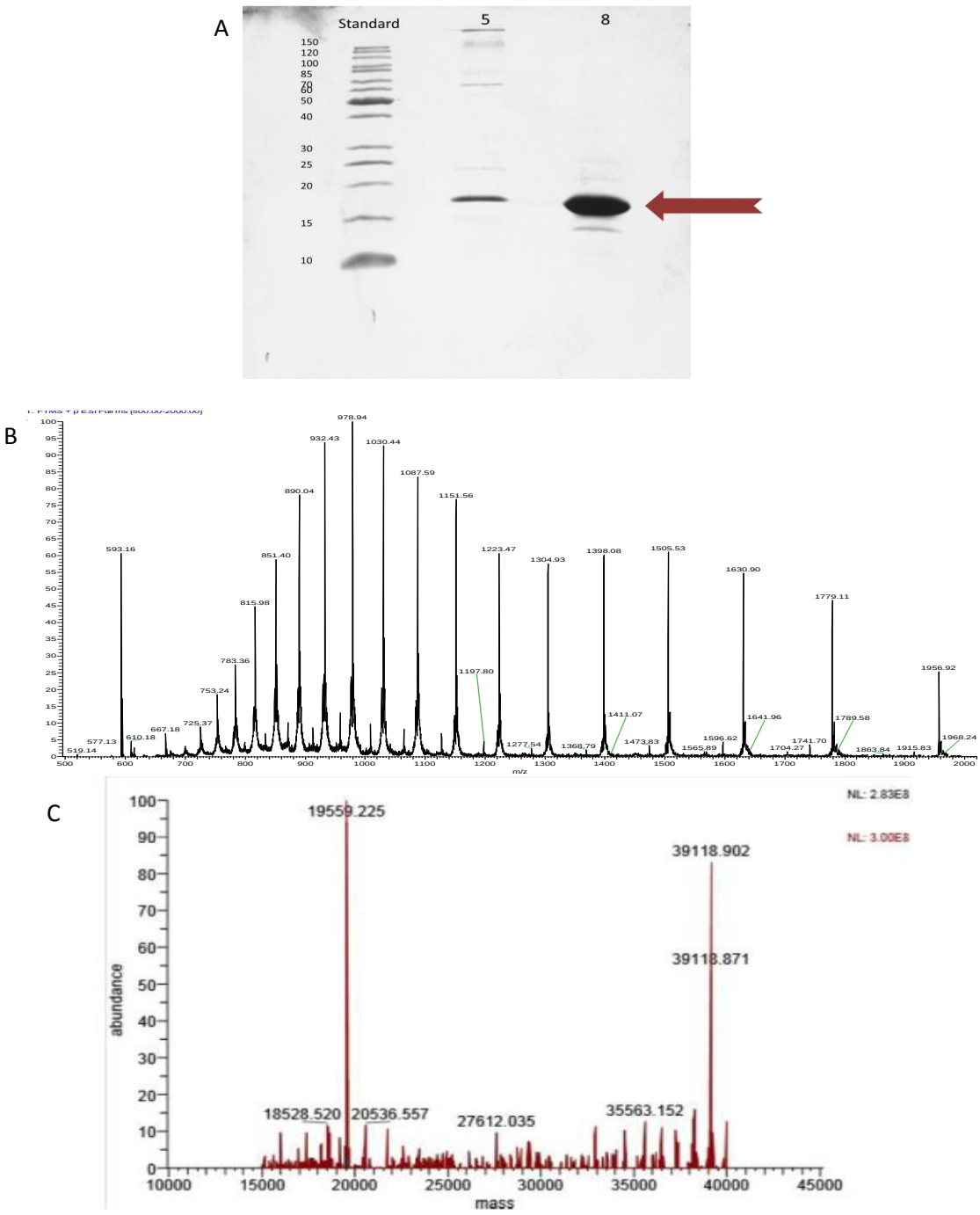

Figure 3.3: Results of SDS-PAGE gel and MS analysis purified of His6-Bfr. (A) SDS-PAGE of the His6-tag Bfr fractions from chromatography. The lanes listed from right to left were fractions 8 and 5, and the PageRuler Unstained Protein ladder from Bio-Rad. The largest bands above the 15 kDa marker (~ 18.7 kDa) were His6-tag Bfr. (B) Mass spectrum of His6-tag Bfr obtained from using a Thermo Scientific Q-Exactive™ mass spectrometer, raw spectrum (B) showed a Gaussian distribution of multiply charged His6-tag Bfr. (C) The processed spectrum was deconvoluted using the MaxEnt 1 tool supplied with the MassLynx software, The deconvoluted mass was measured as 19559.22 Da, one mass unit different from the correct mass of 19560 Da.

3.3.2. Synthesis of ND-NTA

ND-NTA was successfully synthesized from NHS activated NA as reported in reference 103. Reaction yield was fairly good, 70%. Product was analyzed using ^{1}H NMR 500 MHz to verify chemical structure and purity; samples were prepared in DMSO-d_6 and our findings presented good agreement with what was reported in the literature (Figure 3.4 A). Mass spectrometry analysis was performed using a Thermo Scientific LTQ Linear Ion Trap. The prominent peaks corresponded to ND-NTA of 543.42 which had a calculated molecular weight of 542.74 Da (Figure 3.4B).

Solutions of ND-NTA with different concentrations were used to perform dynamic light scattering (DLS) experiments. The critical micellar concentration (*cmc*), the concentration at which amphiphilic molecules begin to form micelles, of ND-NTA was reported in reference 105 to be 0.012 mg/mL or 0.02 mM. Concentrations used for DLS analysis were *cmc*/2, *cmc*, 2x *cmc*, 4x *cmc*, 1 mM, and 2 mM. Although DLS is not a standard tool for measuring micelle size in absolute terms, it was very useful to obtain a rough estimation of the size of the ND-NTA micelles. Number- and volume-based distributions were used to obtain mode peak values of aggregation size for each concentration (Figure 3.5). Analysis of the results showed that ND-NTA exhibits sharp transitions into micellization at concentrations of 1 mM and 2 mM with aggregate sizes of 7-10 nm. Thus a 2 mM concentration was used to perform the micelle encapsulation studies. Moreover, number and volume distribution results of 2 mM ND-NTA aqueous solution were compared to those of a 2 mM ND-NTA solution in the denaturing buffer system, consisting of 8 M GdnHCl with 50 mM Tris and 100 mM NaCl at pH 8, at which the micelle encapsulation would be performed. As expected, the ND-NTA hydrodynamic size was

found to be higher in the solvent with high solute concentration due to the effect of salts on the surface charges of surfactant head groups allowing the micelles to grow (Figure 3.6).

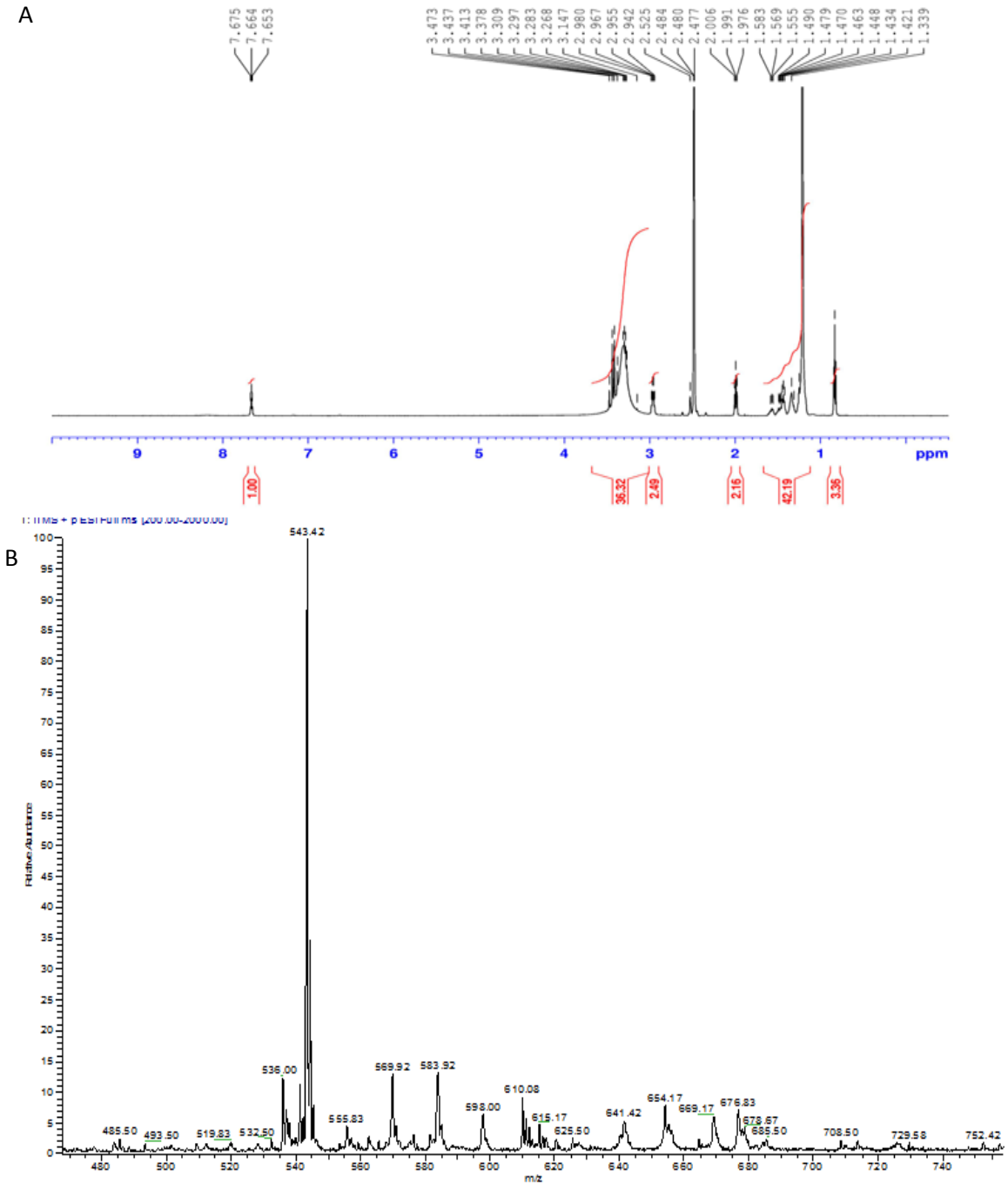

Figure 3.4: Results of ^{1}H NMR and MS analysis of synthesized ND-NTA. (A) ^{1}H NMR (500 MHz) results were as following: 0.81-0.84 (3H, t), 1.21–1.44 (40H, m), 1.9-2.01 (2H, t), 2.9 (2H, d), 3.20–3.42 (12H, m), 7.6 (1H, t), nonintegrated signals at 1.9-2 are related to the DMSO-d_6. (B) ND-NTA was detected at m/z+ of 543.42 as its calculated MW is 542.72 g/mol.

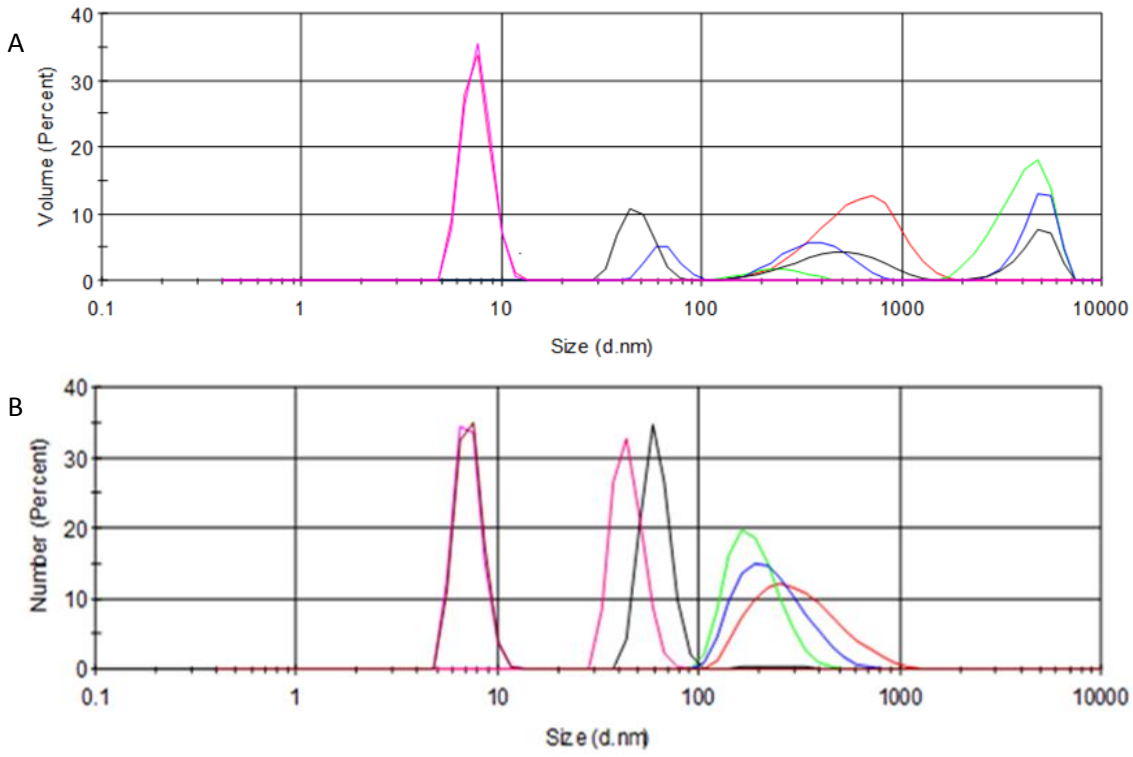

Figure 3.5: Overlay of volume (A) and number (B) distribution analysis of DLS results of different concentrations of ND-NTA in water. 0.01 mM (red), 0.02 mM (blue), 0.04 mM (green), 0.08 mM (black), 1 mM (pink) and 2 mM (magenta).

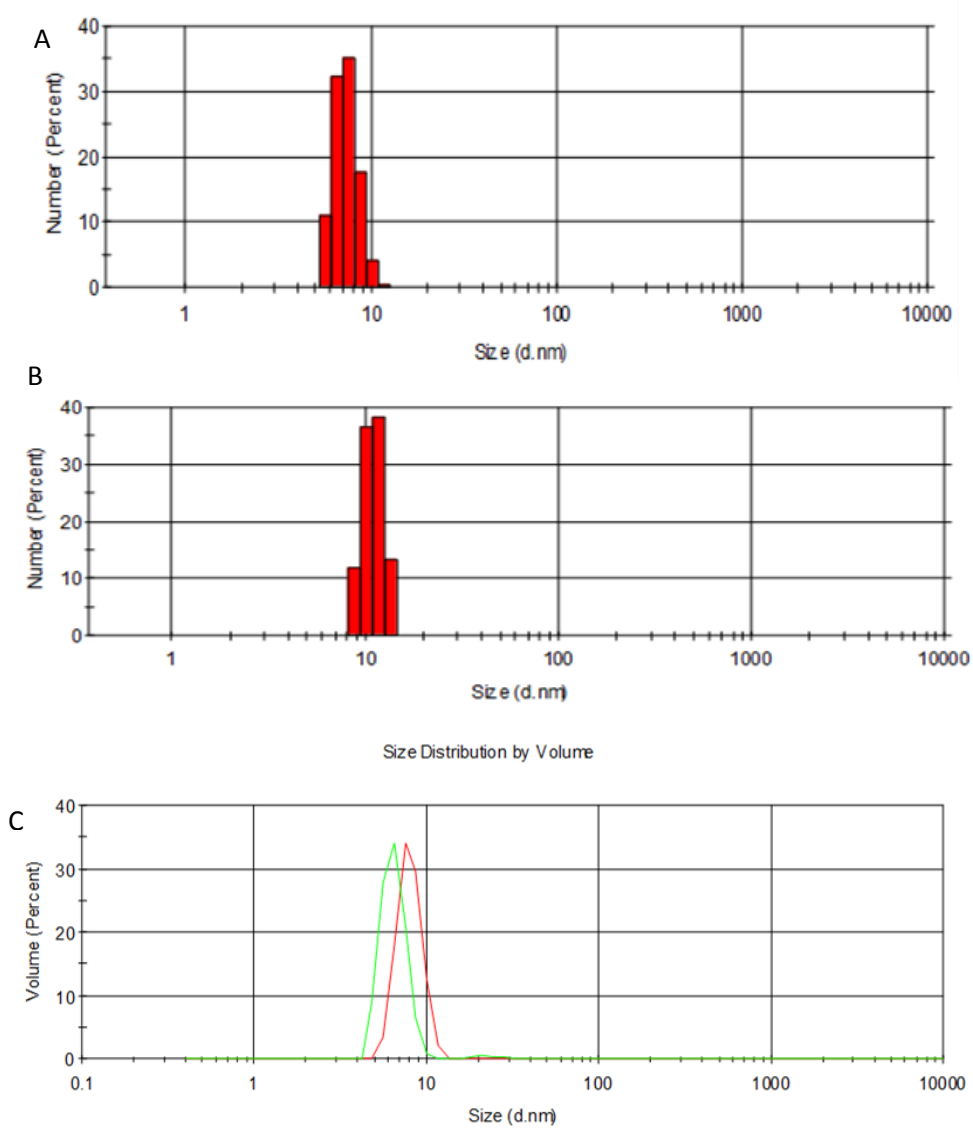

Figure 3.6: DLS results of a number- (A&B) and volume- (C) based distributions of ND-NTA micelles in water and in denaturing buffer solution. ND-NTA micelles in water (A, green in C) exhibits an aggregation size of 7-10 nm while in the case of the denaturing buffer solutions (B, red in C) its aggregation size increased to 9-12 nm. Concentration of ND-NTA in these experiments was 2mM.

3.3.3. ND-NTA micelle encapsulation

Introduction of a ND-NTA micelle into the His6-Bfr cavity was achieved through mixing the His6-Bfr with ND-NTA, hemin chloride and $NiSO_4$ in 8 M GdnHCl buffered with 50 mM Tris, 100 mM NaCl at pH 8.0 which is used to decluster the Bfr cages for 90 minutes at 5 ^{0}C.

$NiSO_4$ was added to complete the metal mediated affinity interaction between the Bfr Histags and the NTA moieties, while hemin chloride was known to facilitate Bfr cage, 24-mer structures, formation. Dialyzed samples were concentrated and purified using SEC. Protein fractions were concentrated and analyzed on SDS-page gel electrophoresis, MS, and TEM. MS analysis indicated the presence of free ND-NTA monomers which have an expected mass of 542.5 g/mol, while deconvoluting the protein spectrum revealed the interaction between His6-Bfr monomer and ND-NTA(Ni) which was expected to have molecular mass of 20157 Da (Figure 3.7).

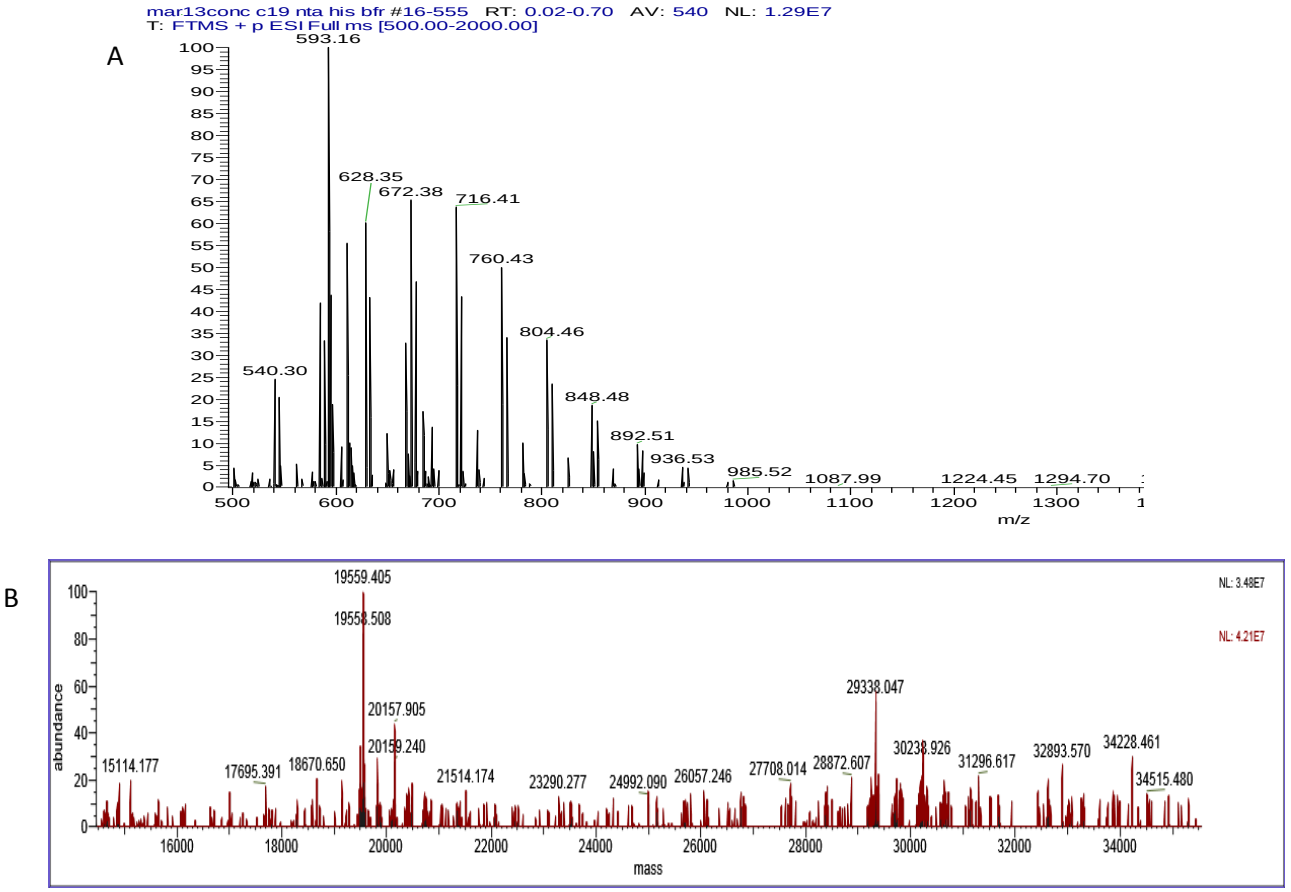

Figure 3.7: MS results of ND-NTA micelle encapsulation experimentations. (A) Raw spectrum revealed a m/z of 540 which corresponds to deprotonated ND-NTA which is expected to have a molecular mass of 542.5 g/mol. (B) The processed spectrum was deconvoluted using the MaxEnt 1 tool supplied with the MassLynx software, The deconvoluted mass of His-Bfr subunit was measured as 19559.22 Da, one mass unit off of the correct mass of 19560 Da, and the mass of His-Bfr subunit complexing with ND-NTA through one Ni atom was calculated as 20157.5 Da.

3.3.4. TEM conditions and results

The encapsulation of the ND-NTA micelle was confirmed by employing transmission electron microscopy (TEM). This technique had been utilized successfully to visualize encapsulated guest molecules such as AuNP and streptavidin within the His6-Bfr.[80] Two TEM stains were used: Phosphotungstic acid and molybdic acid to visualize Bfr capsules and determine the presence of the encapsulated hydrophobic structures. Such atom sized stains were known to penetrate through the intrinsic pores found in the Bfr shell into the cavity. Based on the analysis of the TEM images, the ND-NTA micelles were large enough to fill most of the His6-Bfr interior and thus exclude the stain away from the cavity. A lack of stain penetration would confirm the encapsulation of large micellar structures within the His6-Bfr lumen.

Trials using phosphotugstic acid and molybdic acid stains were used at first to optimize the visualization of Apo-His6-Bfr, and the same stains were utilized to probe the presence of the ND-NTA micelle within the Bfr complex. Apo-Bfr images revealed the penetration of stains in to the Bfr core; however, some of the protein molecules lacked stain penetration, which could be due to the uneven distribution of the stain on the TEM grid or could be due to the low clarity of the images (Figure 3.8). Molybdic acid was chosen as the stain for subsequent studies.

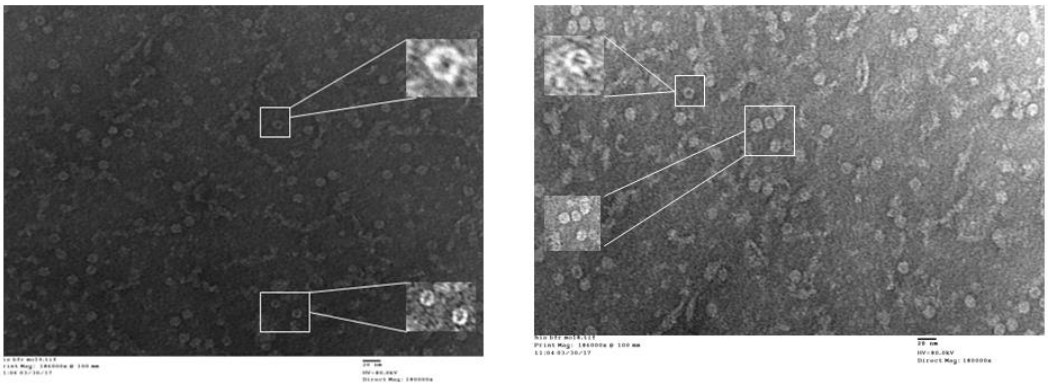

Figure 3.8: Negatively stained TEM images of apo-His6-Bfr using molybdic acid (left) and phosphotungstic acid (right). Apo-His6-Bfr appears as a donut shaped 2-D object due to the penetration of the stains in to the core.

TEM imaging results of His6-Bfr with likely encapsulated micelles were comparable to those of the apo His6-Bfr in terms of both morphology and size. Lack of stain penetration was clear where all protein structures were dull in color in comparison to the donut-shaped protein structures observed in the apo His-Bfr images (Figure 3.9), which are entirely consistent with micelle encapsulation within the His6-Bfr. Furthermore, the His6-Bfr capsules with micelles encapsulated appeared to be larger than the apo-His6-Bfr; diameter changes were estimated to be about 1.8-fold larger in diameter for the loaded protein capsules This result could be due to the large size of ND-NTA micelles and their hydrodynamic nature, which cause the protein cages to appear as swollen capsules accommodating such large guest structure. However, Bfr cages appeared to be less uniform in shape and size, which could be due to particles overlapping or particle fusion caused by high intensity electron beams used to produce very high magnification images.

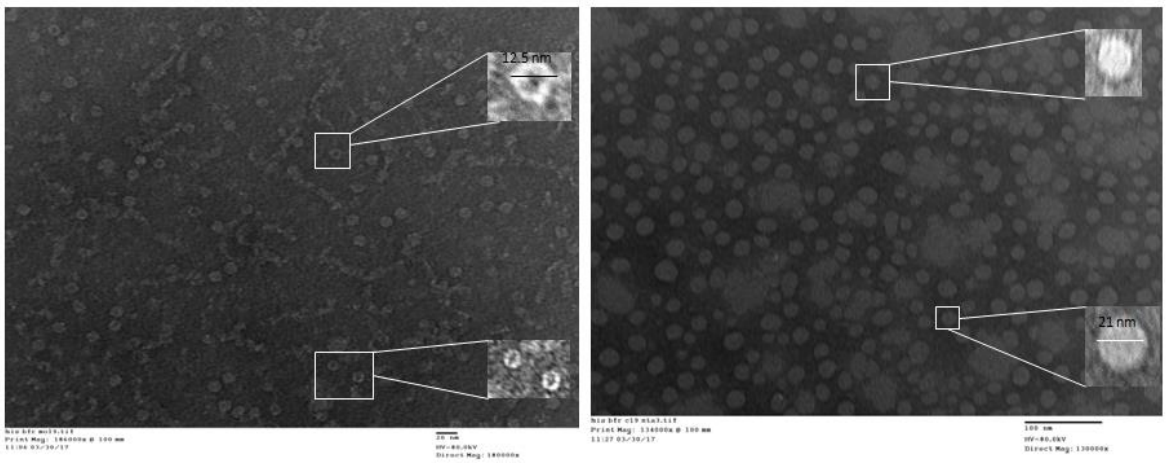

Figure 3.9: TEM imaging results of apo-His6-Bfr and His6-Bfr encapsulating ND-NTA micelle stained by 0.5 M solution of molybdic acid. Donut-shaped appearance of apo-Bfr (left) indicates the penetration of the stain into the cage cavity, while the absence of stain penetration resulted in the dull sphere appearance of Bfr cages encapsulating the micelles (right). Magnified images of single protein particle showed a dark shell area surrounding a brighter cavity. Diameter analysis using ImageJ software of different protein particles demonstrated that micelles containing Bfr molecules diameters within the range 20-22 nm, compared to apo-Bfr particles which exhibits diameters between 12-14 nm.

3.3.5. Fluorescence studies of pyrene

Pyrene has been widely used as a fluorescent probe to characterize various micellar solutions; intensities of pyrene emissions have been used to determine the critical micelle concentration (*cmc)* of different surfactants. Of interest to the current work, the use of pyrene emission patterns to confirm the *cmc* of ND-NTA was reported in reference 105. In this project, pyrene was first loaded into ND-NTA micelles and then pyrene-loaded micelles were introduced into His6-Bfr cages. SEC-purified His6-Bfr samples were analyzed using fluorescence spectroscopy to probe the existence of pyrene within Bfr cages and results were compared to standard pyrene-loaded ND-NTA micellar solutions (Figure 3.10). Pyrene emission spectra excited at λ= 335 exhibited vibronic patterns for both samples with λ_1 = 372 and λ_2 = 392, which is consistent with results reported in literature;[105] however, pyrene vibronic bands from Bfr samples exhibited lower intensities. This could be due to the presence of heme in this sample that could absorb some of the pyrene energy as reported in the literature,[106] in addition to the effect of the pyrene being placed in a slightly different environment, that of the protein cavity. Also, pyrene emission exhibited an extra band, termed an excimer, around 470 nm. This additional band usually appears when two fluorophores are spatially adjacent,[107] which suggests that there is more than one pyrene molecule within the single ND-NTA micelle in both solutions. Emission based standard curve calculations were used to estimate the number of pyrene molecules within a single Bfr cage, which was able to accommodate a minimum of 6 pyrene equivalents (Appendix 1). To verify the effect on pyrene fluorescence provided by heme quenching and the internal protein environment itself, pyrene-loaded protein cages were declustered using a denaturing buffer solution of GdnHCl. Pyrene emission spectra were collected after different time intervals and compared to those of the intact protein cages; a gradual enhancement in pyrene emission

intensity was observed (Figure 3.11). These results suggest that pyrene molecule emission is reduced within the encapsulated micelle due to a combination of self quenching as well as quenching due to the presence of heme molecules present in the protein. In addition, the pyrene excimer band at around 470 nm was not observed after the protein denaturation, which suggests that fluorophores were pulled away from each other probably due to micelle breaking after dilution. Moreover, in order to confirm that pyrene probe was dissolved within the encapsulated micelle in the previous study, a standard trial experiment for introducing pyrene into His6-Bfr was performed. Although the concentration of pyrene was very low to be encapsulated through a concentration gradient encapsulation pathway any hydrophobic interaction between pyrene and Bfr surface could result in a detection of pyrene within the Bfr sample; therefore, a similar encapsulation procedure was followed without addition of the amphiphilic compound, ND-NTA.

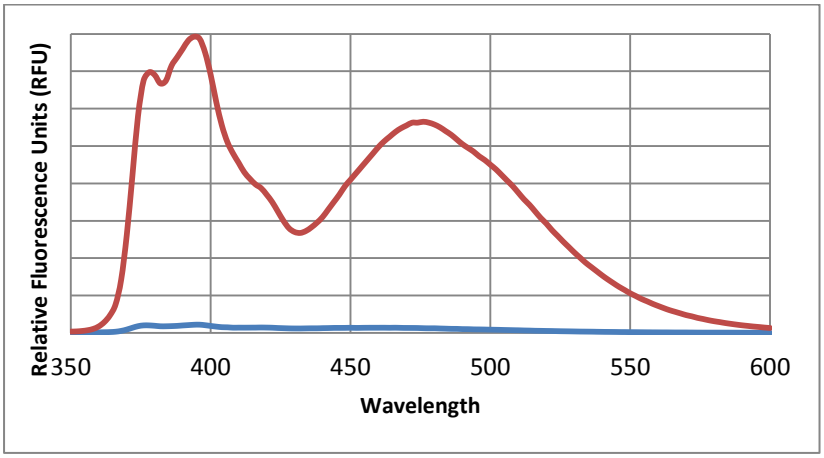

Figure 3.10: Comparison of pyrene emission spectra obtained from 2 mM ND-NTA micellar solution (red) and pyrene-loaded ND-NTA micelle within the Bfr cages (blue). Detailed RFU values for the blue scan can be obtained from Figure 3.11.

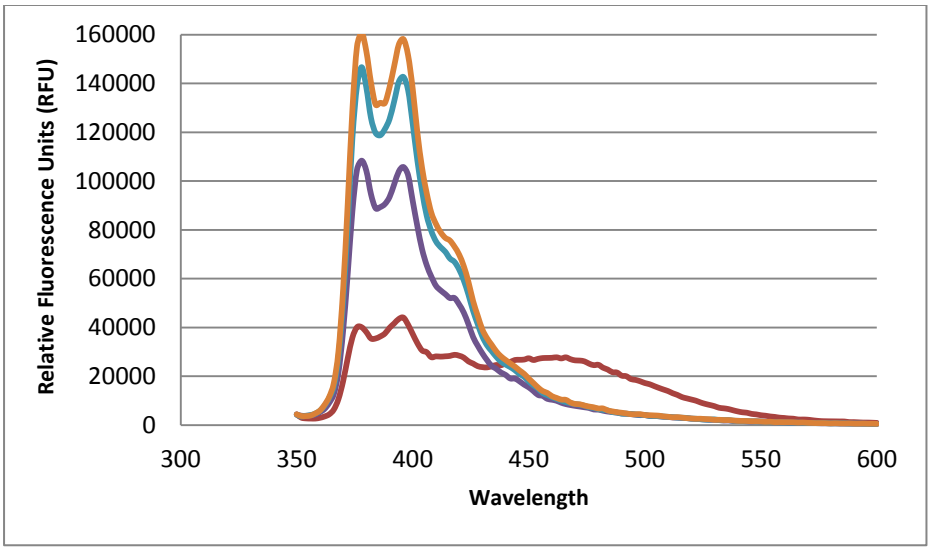

Figure 3.11: Fluorescence spectroscopy results of pyrene-loaded ND-NTA micelle encapsulation. The lowest intensity plot (red) correspond to intact His6-Bfr cages containing pyrene dissolved within the micellar structure; upon denaturing about 5-fold enhancement in pyrene emission intensity was noticed after 10 minutes (dark blue) which gradually increased (30 minute, cyan) until an 8-fold (orange) increase in intensity after one hour under protein declustering conditions was observed. Also the pyrene excimer band at around 470 nm disappeared after declustering the protein.

In addition, fluorescence spectroscopy results of the control experiment indicated that pyrene can not be introduced into the Bfr cage without being dissolved first within a micellar structure since no evidence of pyrene emission was detected that was associated with the protein (Figure 3.12); however, low emission signals were detected between 350 nm and 400 nm which probably correspond to the amino acid tryptophan from the Bfr subunits. For further confirmation an apo-His6-Bfr, heme-free sample at the same concentration was analyzed under the same excitation conditions and an identical emission profile was obtained. However, relatively higher emission intensity was observed in the heme-free protein sample which could be due to the quenching effect of heme on the tryptophan emission as was previously reported in the literature.[108]

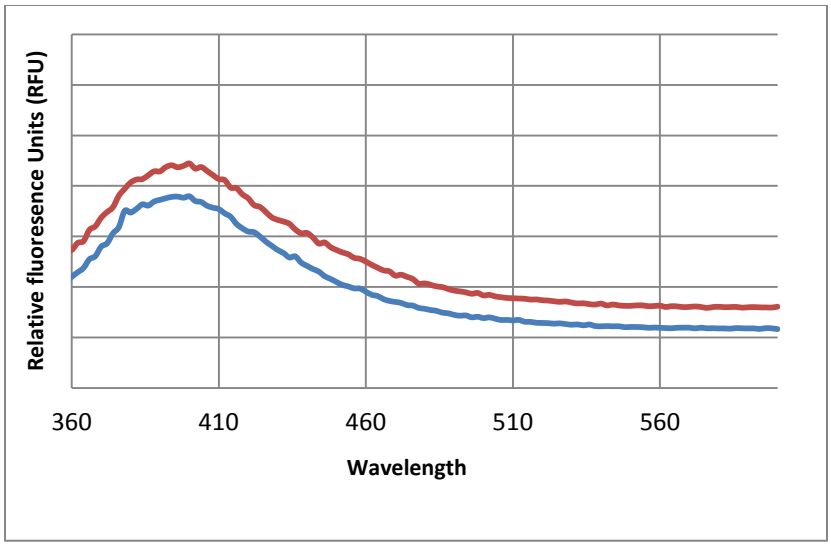

Figure 3.12: Fluorescence spectroscopy results of the control pyrene encapsulation experiment (blue) and apo-His6-Bfr solution (red). Emission spectra between 350 nm and 400 nm from both samples probably correspond to tryptophan from the Bfr protein.

3.3.6. Encapsulation of DGS-NTA(Ni) within His6-Bfr

An attempt to introduce DGS-NTA(Ni) lipid molecules into the His6-Bfr cavity was performed through the addition of DGS-NTA(Ni) to a solution of His6-Bfr in the presence of hemin chloride in a denaturing buffer solution. Reclustered protein cages were purified using size-exclusion column chromatography. First fractions from the gel filtration chromatography step were suspected to contain nanoparticles that were larger than His6-Bfr cage molecules, which usually elutes after 40 minutes (Figure 3.13); therefore, samples from the first fractions were collected and separated from those that were expected to contain the His6-Bfr protein, and both samples were visualized by TEM. Analysis of the MS results of the second set of fractions confirmed the presence of His6-Bfr protein as expected. DGS-NTA(Ni) was analyzed by MS to optimize its ionization and thus detection conditions. unfortanately, we were unable to detect any of the lipid using MS run in the positive ion mode while the use of negative ion mode provided a good ionization and an interpretable spectrum showing what could be the Na^+ adducts of the

lipid detected at m/z$^-$ 1264. Protein signals were detectable using both the positive and negative ion modes; however, lipid signals were not detectable in the presence of the protein in the ionization field and they were observed later after the sample was removed and the ionization solution was run through the system (Figure 3.14). The reason could be that the high degree of ionization of the protein would probably suppress the ionization of the lipid and once the protein sample was discarded, the ionization of lipid molecules, which were still in the system, could be optimized. Analysis of the MS results suggests that DGS-NTA(Ni) could be successfully loaded into the Bfr cavity. Also, the concentration of pure protein cages obtained from this experiment was found to be lower than that of the ND-NTA micelle encapsulation which could be due to the association of protein subunits with the formed lipid aggregates. Therefore, further analysis using TEM and DLS was necessary in order to verify the lipid encapsulation, and investigate the nature of lipid aggregates that were formed during the experiment.

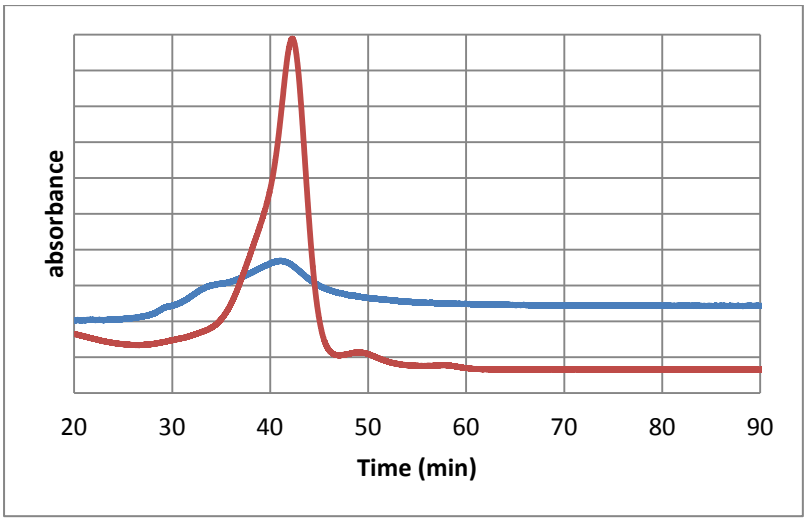

Figure 3.13: Size exclusion chromatography results obtained at 260 nm for Apo-His6-Bfr (red) and DGS-NTA(Ni)-loaded His6-Bfr (blue). Early fractions collected after 30 minutes were suspected to contain aggregate that are larger than the Bfr cage protein, therefore they were collected and visualized under TEM separately.

A

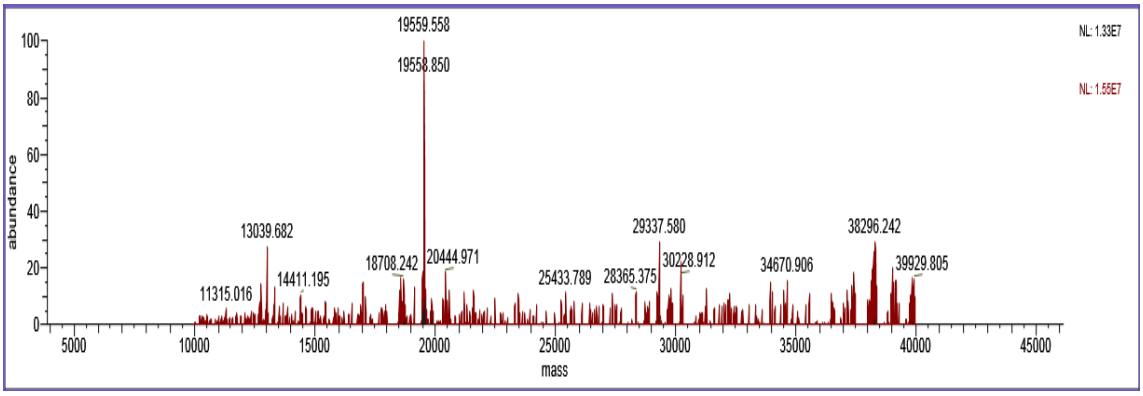

B

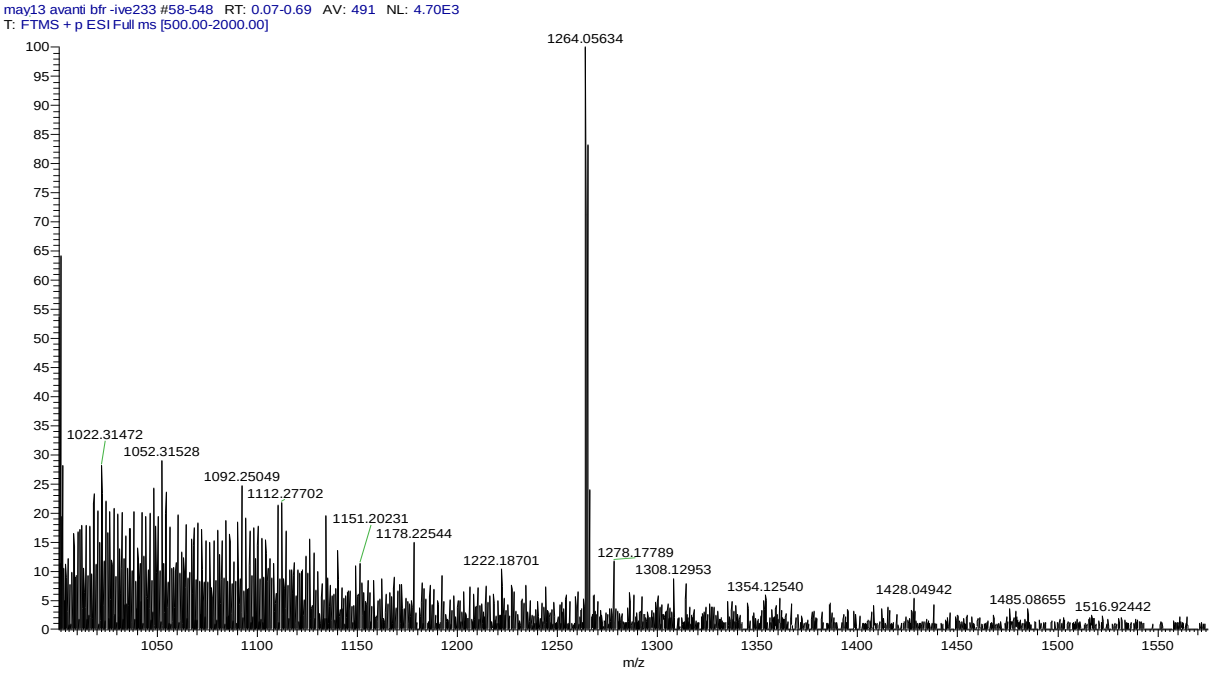

Figure 3.14: Mass spectrometry results of His6-Bfr encapsulating DGS-NTA(Ni). (A) Deconvoluted spectrum of mass expected for a single His6-Bfr subunit is detected at m/z of 19559.5. (B) Raw spectrum showing expected multi-sodium DGS-NTA(Ni) at m/z of 1264 after protein sample was discarded; however, traces of the multicharged protein signals can be observed in the spectrum. Similar signal was observed when standard free lipid was analyzed under same the conditions.

3.3.6.1. TEM conditions and results

A staining solution of 0.5 % molybdic acid was used to visualize protein molecules as previously described. TEM images revealed a lack of stain penetration into the protein core from most of the protein molecules which indicates that DGS-NTA(Ni) lipid molecules have been indeed encapsulated within the His6-Bfr cavity (Figure 3.15). In addition, it was observed that most of the protein molecules were slightly larger than expected; around 2 nm increases in diameter were measured in ImageJ software for protein particles with suspected encapsulated guest lipid. In contrast, empty protein molecules from the same grid had a diameter of 12.3 nm which is consistent with that of the apo-Bfr cage protein.

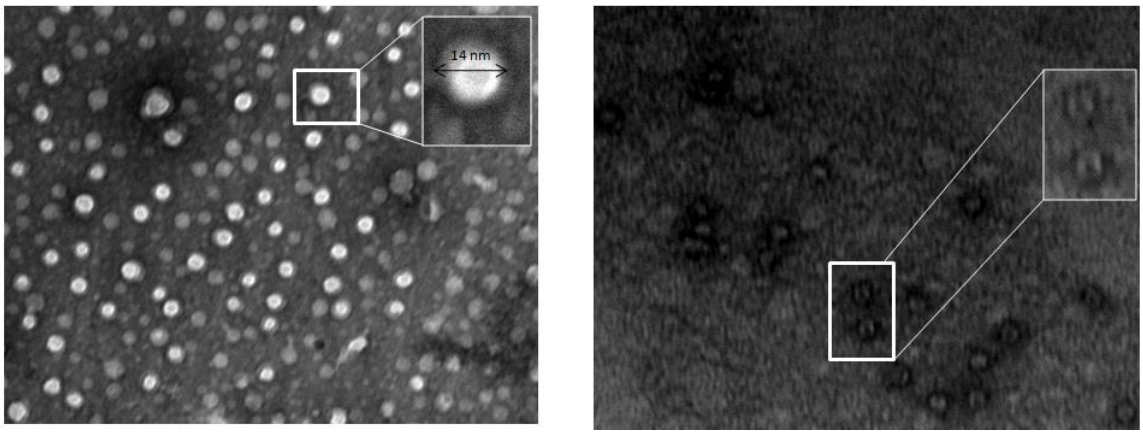

Figure 3.15: TEM imaging results of DGS-NTA(Ni) encapsulation experiment. Protein molecules on the left presented lack of stain penetration along with a slight enhancement in size. Images of other part of the grid revealed some empty protein cages appeared as donut-shaped structures due to the penetration of stain into the core of the protein along with other protein structures which possibly were occupied by guest molecules, thus their cores were not stained.

In addition, the first fractions from gel filtration chromatography were visualized under TEM and compared to those obtained from a solution of 18:1 DGS-NTA(Ni) (0.95 mg/mL); images of both samples revealed the formation of aggregates of different sizes ranging from 40 nm to 120 nm (Figure 3.16). The excess DGS-NTA(Ni) observed from the encapsulation experiment could be due to the use of excess equivalents of the lipids in the experiment.

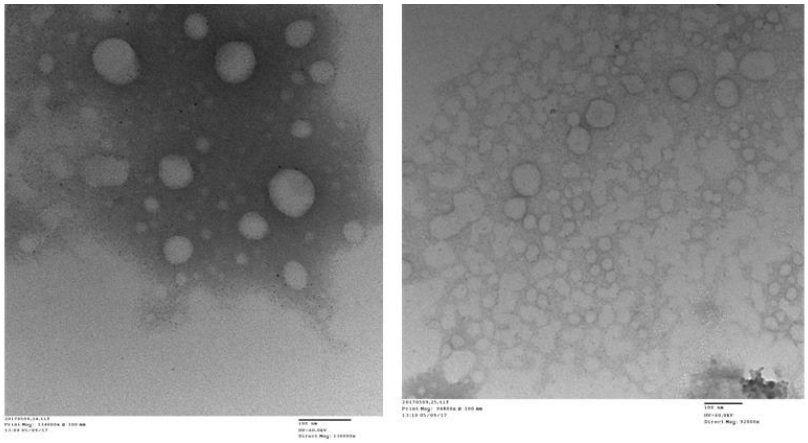

Figure 3.16: TEM imaging results of first fractions obtained from size exclusion chromatography (Right) and a prepared solution of DGS-NTA(Ni) at concentration of 0.95 mg/ml (Left). Aggregations of different sizes (40-120 nm) were observed in both samples. The shell-like structure observed in samples from the SEC fractions could be due to the attachment of protein subunits to the surface of the aggregates since similar interactions have been reported in the literature where DGS-NTA(Ni) was used to design protein coated liposomes.[109]

3.3.6.2. DLS results

Samples of DGS-NTA(Ni) at two different concentrations, 1 mg/mL and 2 mg/mL, were analyzed using DLS. Although different studies have utilized the same lipid structures toward synthesis of liposomes,[109] the behavior of these kinds of lipids at lower concentrations have not been clearly elucidated. Therefore, we utilized DLS to characterize the behavior of the guest lipid under concentrations close to what were utilized during the encapsulation experiments. Analysis have shown that the size of aggregates formed by DGS-NTA(Ni) lipids decreases as the concentration increases (Figure 3.17). Similar phenomena were observed in two studies with different kinds of lipid molecules.[110,111] The reason for this behavior could be due to the increased access of the mono DGS-NTA(Ni) to the surface of the aggregates as its concentration increases which could have resulted in an increase in the surface curvature.[110] Moreover a solution of DGS-NTA(Ni) in the denaturing buffer solution, consisting of 8 M GdnHCl, 50 mM Tris and 100 mM NaCl, was analyzed by DLS to ascertain the effect of high solute

concentrations on the morphology of such structures, however high concentration of solutes did not have any effect on the size of the DGS-NTA(Ni) aggregates (Figure 3.17).

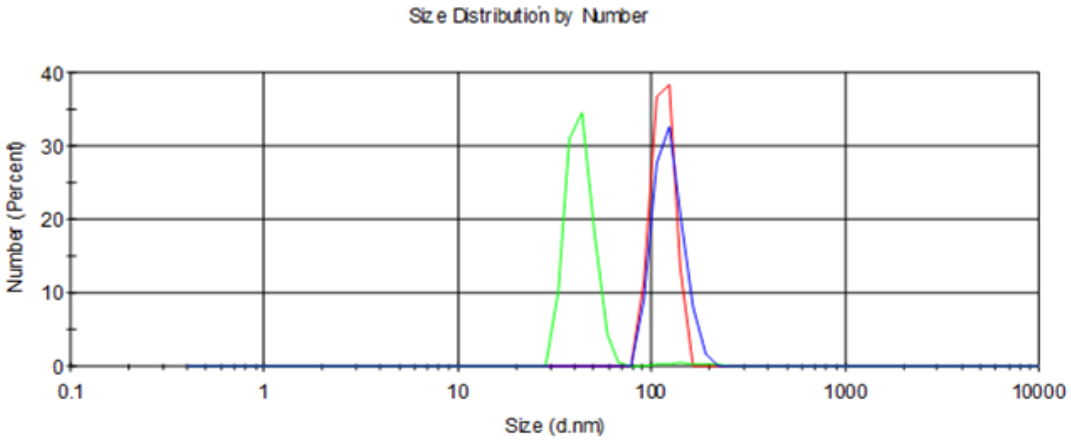

Figure 3.17: DLS size analysis results of 1 mg/mL and 2 mg/mL solutions of 18:1 DGS-NTA(Ni). Solutions of 1 mg/mL DGS-NTA(Ni) in water (red) and in denaturing buffer (blue) exhibited aggregations with diameter around 120 nm, while a higher concentration of about 2mg/mL exhibited smaller aggregation size of about 45 nm (green).

Moreover, DLS was utilized to compare the size of ND-NTA micelles and DGS-NTA(Ni) loaded His6-Bfr to that of the apo-His6-Bfr to verify the TEM results. Analysis of the results confirmed the size increase in the His6-Bfr host after introducing the hydrophobic guests to its core (Figure 3.18). Confirming the TEM results, the largest size reported corresponded to ND-NTA micelles containing Bfr, with a diameter of about 16 nm, whereas the DGS-NTA(Ni)-loaded His6-Bfr exhibited a diameter of about 14 nm.

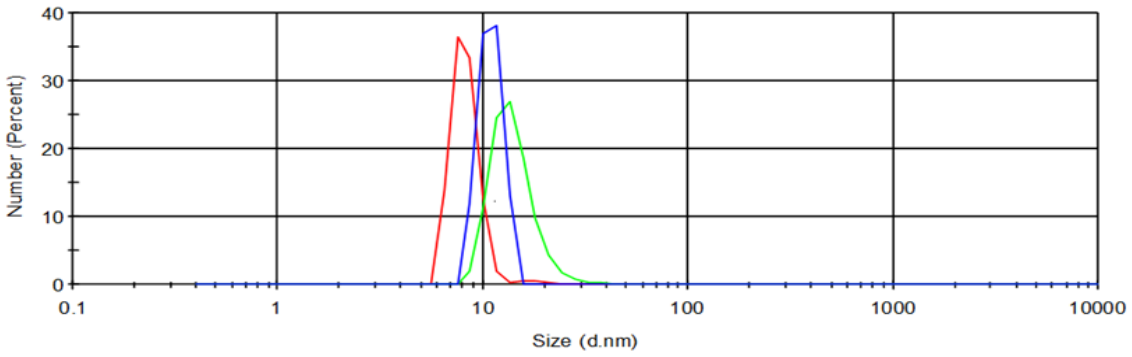

Figure 3.18: Typical number-based size distribution results of apo-His6-Bfr (red), His6-Bfr encapsulating DGS-NTA(Ni) (blue), and His6-bfr encapsulating ND-NTA micelles (green). Although DLS is not a standard technique to determine the actual size of particles, however in this case, DLS results confirmed previous TEM results that indicated an increase of the size of protein particles after encapsulating hydrophobic molecules.

3.4. Conclusions

The results presented in this chapter indicate that His6-Bfr is able to accommodate hydrophobic guest molecules with NTA functionalities such as the ND-NTA micelle (Figure 3.19). As described earlier, the size of the encapsulated cargos were found to strongly affect the size of the Bfr cage protein which have shown surprising flexibility to accommodate such large guest molecules. These findings could be employed towards the engineering of protein-based hydrophobic molecular delivery platforms.

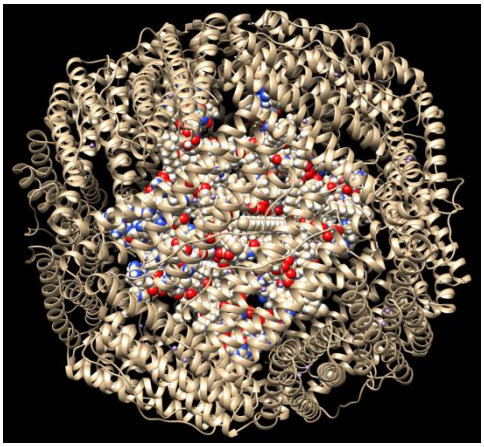

Figure 3.19: Illustration of a His6-Bfr with C19LysineNTA-Histag with linker shown in space fill in the centre of the protein. Image was generated in Chimera using PDB ID: 1BFR.

4. Chapter 4: Future Prospects

4.1. Introduction

The research presented in this thesis has extended the versatility of Bfr as a nanobioplatform in terms of chemical modification and molecular loading; however, further investigations are required in order to obtain a better understanding of the host-guest interaction and to further expand the capabilities of this protein. The synthesis of more hydrophobic heme analogues can be achieved and optimized based on the findings presented in Chapter 2, and a further improvement of purification yields of the heme-bis-amine analogues could be accomplished. Also the introduction of hydrophobic heme analogues to His6-Bfr could be achieved through the encapsulation of previous hydrophobic guest molecules such as ND-NTA, since the formation of a micellar environment within the system could improve the solubility of the hydrophobic heme analogues and thus its incorporation into the Bfr cage (Figure 4.1). Moreover, different carboxylic acids, shorter than nonadecanoic acid, can be used to synthesize alkyl chains with NTA functionalities; then additional encapsulation studies on smaller micelles can be investigated.

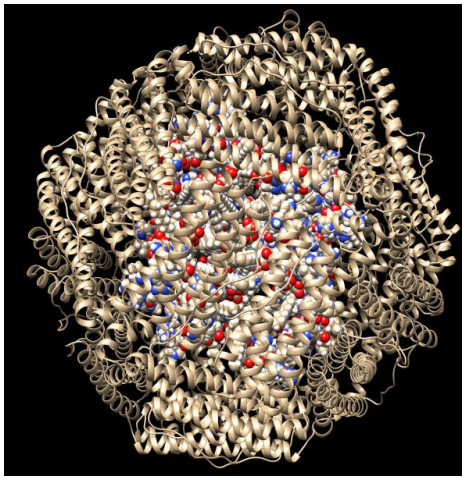

Figure 4.1: An illustration of a His6-Bfr with C18alkylamine groups on the hemes shown in space fill in the centre of the protein. Also in the centre is shown the C19LysineNTA-Histag with linker and this is shown in space fill as well. Image was generated in Chimera using PDB ID: 1BFR and chemical drawing of the heme and NTA compounds.

4.2. Loading different hydrophobic drugs into the engineered His6-Bfr

As described in Chapter 3, the hydrophobic probe pyrene was successfully loaded into the His6-Bfr and released upon protein denaturation. The same procedure can be used to load hydrophobic compounds such as curcumin and Carmustine, also known as bis-chloronitrosourea (BCNU), (Figure 4.2) into the Bfr cage and then undertaking their evaluation against mammalian cell lines as they were previously utilized to evaluate other hydrophobic delivery scaffolds.[100,112] The encapsulation efficiency of some drugs such as haloperidol can be estimated through monitoring the changes in absorption and fluorescence spectra of the encapsulated drug.[113]

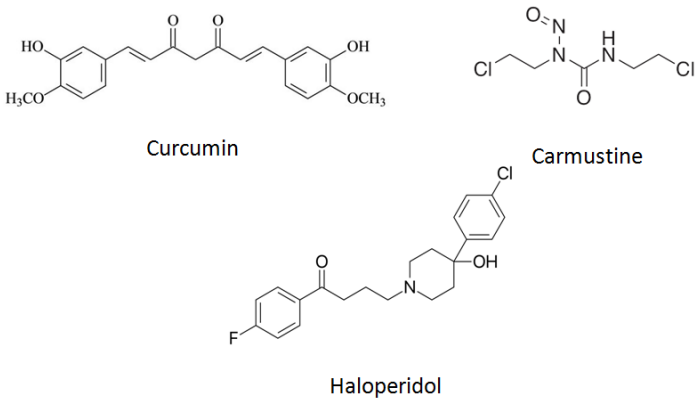

Figure 4.2: Structures of some hydrophobic compounds that might be loaded into the Bfr core through micelle encapsulation.

4.3. Combining the hydrophobic engineering with the surface modification of His6-Bfr cage protein

As a delivery platform, it is critical to engineer the outer surface of the Bfr in order to improve the targeting specificity of this nanocarrier. The previous work on ferritin, which was discussed earlier in Chapter 1, could be applied to the Bfr cage protein; for instance affinity tags could be added to the outer surface of His6-Bfr such as RGD peptides[60] and utilized to direct

hydrophobic therapeutics into a tumor cell line. Moreover, Hawa Gyamfi, a Ph.D. candidate in the Honek laboratory, has studied several N-terminal extensions of the Bfr subunits; several Qtag and Sort tag sequences have been added to the N-terminal methionine (Figure 4.3). The Qtags are glutamine-containing peptides that are substrates for the enzyme transglutaminase. They would be used to link on a new amine to the glutamine thus to the Bfr surface. For instance, Ms. Gyamfi has already shown that transglutaminase can replace the "NH_2" of the glutamine in the tag with dansyl cadaverine, a fluorescent amine, which was successfully added to the Bfr subunits. The SortTag would be useful with an enzyme called sortase, whose reaction is shown in Figure 4.4. It is another way to attach proteins or peptides to the surface of Bfr using the enzyme sortase. This work could be used in future to direct our engineered His6-Bfr delivery system to material surfaces or cells.

MKGDTKVINYLNKLLGNELVAINQYFLHARMFKNWGLKRLNDVEYHESIDE
MKHADRYIERILFLEGLPNLQDLGKLNIGEDVEEMLRSDLALELDGAKNLREA
IGYADSVHDYVSRDMMIEILRDEEGHIDWLETELDLIQKMGLQNYLQAQIRE
EGLEHHHHHH

Tag	Sequence
QTag 1	MKETAAAKFERQHMDSPDLH
QTag 2	MKETAAAKFERQHMDSGGGG
QTag 3	MERLQQPTGGG
QTag 4	MERLQQPTGGGG
SortTag1	MLVPRGGGGG

Figure 4.3: Constructs of some of the tags that were successfully added to the external N-termini of the Bfr subunits. The top sequence shown in black is for a His6-Bfr subunit. Different tags are displayed in the table where the linker region is shown in red while the tag sequence is colored in green.

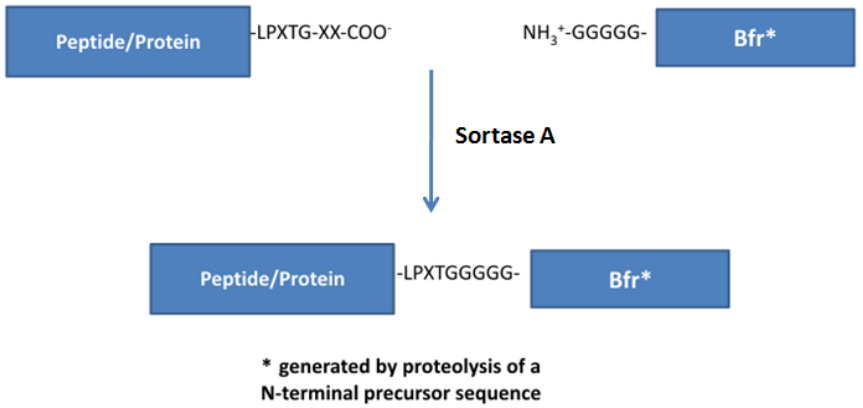

Figure 4.4: Schematic illustration of the sortase mediated reaction to add proteins or peptides to the surface of Bfr. The SortTag1 sequence would be displayed on the surface of Bfr, a protease would be required to trim back this exposed sequence to produce "GGGGGMKGD…" which is necessary for the sortase reaction. This new Bfr would be the nucleophile that would be used by sortase to react with any peptide or protein that had a C-terminus sequence "….LPXTGXX" The sortase reacts with this protein/peptide. The sortase forms an activated thioester and the N-terminus of the GGGGG-Bfr reacts and displaces the sortase enzyme, forming a new attachment to the surface of Bfr.

Moreover, enhancement of cell internalization of the engineered His-Bfr system through the attachment of types of cell permeable peptides (CPP) onto the surface of His6-Bfr, which could be attached through formation of disulfide linkage to engineered surface cysteines, could be investigated. The CPPs are short sequences of positively charged amino acids that are known for their ability to traverse the cell membrane.[114] these peptides have been previously utilized to facilitate cell penetration and internalization of different protein-based therapeutic cargos.[115,116] The success in delivering our engineered nanocarrier into cells would highlight novel drug delivery applications and could be employed toward the development of promising cage protein-based drug delivery platforms with capabilities of delivering hydrophobic cargos.

References

1. Lee, A.; Wang, Q. Adaptations of nanoscale viruses and other protein cages for medical applications. *Nano. Med. J.* **2006**, *2*, 137-149.

2. Ma Ham, A.; Tang, Z.; Wu, H.; Wang, J.; Lin, Y. Protein-based nanomedicine platforms for drug delivery. *Small* **2009**, *5*, 1706-1721.

3. Georgens, C.; Weyermann, J.; Zimmer, A. Recombinant virus like particles as drug delivery system. *Curr. Pharm. Biotechnol.* **2005**, 6, 49-55.

4. Muller, O.; Kaul, F.; Weitzman, M.; Pasqualini, R.; Arap, W.; Kleinschmidt, J.; Trepe, M. Random peptide libraries displayed on adenoassociated virus to select for targeted gene therapy vectors. *Nat. Biotechnol*. **2003,** 2, 1040-1046.

5. Flenniken, M.; Liepold, L.; Crowley, B.; Willits, D.; Young, M.; Douglas, T. Selective attachment and release of a chemotherapeutic agent from the interior of a protein cage architecture. *Chem. Commun. (Camb*). **2005**, 447-449.

6. Flenniken, M.; Liepold, L.; Harmseen, AL.; Harmseen AG.; Willits, D.; Young, M.; Douglas, T Melanoma and lymphocyte cell-specific targeting incorporated into a heat shock protein cage architecture. *Chem. Biol.* **2006**, 13, 161-170.

7. Verheije, M.; Würdinger,T.; van Beusechem, V.; de Haan, C.; Gerritsen, W.; Rottier, P. Redirecting coronavirus to a nonnative receptor through a virus-encoded targeting adapter. *J. Virol*. **2006**, 80, 1250-1260.

8. Gleiter, S.; Lilie, H. Cell-type specific targeting and gene expression using a variant of polyoma VP1 virus-like particles. *Biol. Chem*. **2003**, 384, 247-255.

9. Mammen, M.; Choi, S-K.; Whitesides, G. Polyvalent interactions in biological systems: implications for design and use of multivalent ligands and inhibitors. *Angew. Chem. Int. Ed. Engl.* **1998**, 37, 2754-27 94.

10. Khor, I.; Lin, T.; Langedijk, J.; Johnson, J.; Manchester, M. Novel strategy for inhibiting viral entry by use of a cellular receptor-plant virus chimera. *J. Virol.* **2002**, 76, 4412- 4419.

11. Ren, Y.; Wong, S.; Lim, L. Folic acid-conjugated protein cages of a plant virus: a novel delivery platform for doxorubicin. *Bioconjug. Chem*. **2007**, 18, 836-843.

12. Douglas, T.; Young, M. Host-guest encapsulation of materials by assembled virus protein cages. *Nature* **1998**, 393, 152-155.

13. Wang, Q.; Raja, K.; Janda, K.; Lin, T.; Finn, M. Blue fluorescent antibodies as reporters of steric accessibility in virtus conjugates. *Bioconjug. Chem*. **2003**, 14, 38-43.

14. Flenniken, M.; Liepold, L.; Crowley, L.; Willits, D.; Young, M.; Douglas, T. Selective attachment and release of a chemotherapeutic agent from the interior of a protein cage architecture., *Chem. Commun.* **2005**, 28, 447-449.

15. Choi, S.; Kwon, I.; Hwang, K.; Kim, I.; Ahn, H. Small heat shock protein as a multifunctional scaffold: Integrated tumor targeting and caspase imaging within a single cage. *Biomacromolecules* **2011**, 12, 3099-3106.

16. Flenniken, M.; Willits, D.; Brumfield, S.; Young, M.; Douglas, T. The small heat shock protein cage from *Methanococcus Jannaschii* is a versatile nanoscale platform for genetic and chemical modification. *Nano lett.* **2003**, 3, 1573-1576.

17. Wu, H.; Engelhard, M.; Wang, J.; Fisher, D.; Lin, Y. Synthesis of lutetium phosphate-apoferritin core-shell nanoparticles for potential applications in radioimmunoimaging and radioimmunotherapy of cancers. *J. Mater. Chem.* **2008**, 18, 1779-1783.

18. Wu, H.; Wang, J.; Wang, Z.; Fisher, D.; Lin, Y. Apoferritin-templated yttrium phosphate nanoparticle conjugates for radioimmunotherapy of cancers. *J. Nanosci. Nanotechnol.* **2008**, 8, 2316-2322.

19. Uchida, M.; Flenniken, M.; Allen, M.; Willits, D.; Crowley, B.; Brumfield, S.; Willis, A.; Jackiw, L.; Jutila, M.; Young, M.; Douglas, T. Targeting of cancer cells with ferrimagnetic ferritin cage nanoparticles. *J. Am. Chem. Soc*. **2006**, 128, 16626-16633.

20. Jutz, G.; Rijn, P.; Miranda, B.; Böker, A. Ferritin: a versatile building block for bionanotechnology. *Chem. Rev.* **2015**, 115, 1653-1701.

21. Kratz, F. Albumin as a drug carrier: Design of prodrugs, drug conjugates and nanoparticles. *J. Control. Release* **2008**, 132, 171-183.

22. Lee, T.; Sokoloski, T.; Royer, G. Serum albumin beads: an injectable, biodegradable system for the sustained release of drugs. *Science* **1981**, 213, 233-235.

23. Lu, W.; Wan, J.; She, Z.; Jiang, X. Brain delivery property and accelerated blood clearance of cationic albumin conjugated pegylated nanoparticle. *J. Control. Release* **2007**, 118, 38-53.

24. Willmott, N.; Chen, Y.; Goldberg, J.; Mcardle, C. ; Florence, A. Biodegradation rate of embolized protein microspheres in lung, liver and kidney of rats. *J. Pharm. Pharmacol*. **1989**, 41,433-438.

25. Latha, M.; Lal, A.; Kumary, T.; Sreekumar, R.; Jayakrishnan, A. Progesterone release from glutaraldehyde cross-linked casein microspheres: in vitro studies and in vivo response in rabbits. *Contraception* **2000**, 61, 329-334.

26. Willmott, N.; Magee, A.; Cummings, J.; Halbert, G.; Smyth, J. Doxorubicin-loaded casein microspheres: protein nature of drug incorporation. *J. Pharm. Pharmacol.* **1992**, 44, 472-475.
27. Elzoghby, A.; Vranic, B.; Samy, W. Swellable floating tablet based on spray-dried casein nanoparticles: Near-infrared spectral characterization and floating matrix evaluation. *Int. J .Pharm*. **2015**, 491, 113-22.
28. Meyer, D.; Kong, G.; Dewhirst, M.; Zalutsky, M.; Chilkoti, A. Targeting a genetically engineered elastin-like polypeptide to solid tumors by local hyperthermia. *Cancer. Res.* **2001**, 61, 1548-1554.
29. Megeed, Z.; Haider, M.; Li, D.; Malley, B.; Cappello, J.; Ghandehari, H. In vitro and in vivo evaluation of recombinant silk-elastin like hydrogels for cancer gene therapy. *J. Control. Release* **2004**, 94, 433-445.
30. Joye, I.; Davidov-Pardo, G.; Ludescher, R.; McClements, D. .Fluorescence quenching study of resveratrol binding to zein and gliadin: Towards a more rational approach to resveratrol encapsulation using water-insoluble proteins. *Food. Chem.* **2015**, 185, 261-267.
31. Gulfam, M.; Kim, J.; Lee, J.; Ku, B.; Chung, B.; Chung, B. Anticancer drug loaded gliadin nanoparticles induce apoptosis in breast cancer cells. *Langmuir* **2012**, 28, 8216-8223.
32. Choi, J.; Park, H.; Kim, T.; Jeong, Y.; Oh, M.; Hyeon, T.; Gilad, A.; Lee, K. Engineered collagen hydrogels for the sustained release of biomolecules and imaging agents: promoting the growth of human gingival cells. *Int. J. Nanomedicine.* **2014**, 9, 5189-5201.
33. Higaki, M.; Azechi, Y.; Takase, T.; Igarashi, R.; Nagahara, S.; Sano, A.; Fujioka, F.; Nakagawa , N.; Aizawa, C.; Mizushima, Y.Collagen minipellet as a controlled release delivery system for tetanus and diphtheria toxoid. *Vaccine* **2001**, 19, 3091-3096.
34. Muvaffak, A.; Gürhan, I.; Hasirci, N. Cytotoxicity of 5-fluorouracil entrapped in gelatin microspheres. *J. Microencapsul.* **2004**, 21, 293-306.
35. Dinarvand, R.; Mahmoodi, S.; Farboud, E.; Salehi, M.; Atyabi, F. Preparation of gelatin microspheres containing lactic acid--effect of cross-linking on drug release. *Acta. Pharm.* **2005**, 55, 57-67.
36. Saha, R.; Vasanthakumar, S.; Bende, G.; Snehalatha, M. Nanoparticulate drug delivery systems for cancer chemotherapy. *Mol. Membr. Biol*. **2010**, 27, 215-231.

37. Alavi, M.; Karimi, N.; Safaei, M. Application of various types of liposomes in drug delivery systems. *Adv. Pharm. Bull.* **2017**, 7, 3-9.

38. Samad, A.; Alam, M.; Saxena, K. Dendrimers: a class of polymers in the nanotechnology for the delivery of active pharmaceuticals. *Curr. Pharm. Des.* **2009**, 15, 2958-2969.

39. Rafiei, P. ;Haddadi, A. Docetaxel-loaded PLGA and PLGA-PEG nanoparticles for intravenous application: pharmacokinetics and biodistribution profile. *Int. J. Nanomedicine* **2017**, 27, 935-947.

40. Buehler, D.; Toso, D.; Kickhofer, V.; Hong Zhou, Z.; Rome, L. Vault engineering for hydrophobic drug delivery. *Small* **2011**, 7, 1432-1439.

41. Swift, J.; Wehbi, W.; Kelly, B.; Stowell, X.; Saven, J.; Dmochowski, I. Design of functional ferritin-like proteins with hydrophobic cavities. *J. Am. Chem. Soc*. **2006**, 128, 6611-6619.

42. Southall , N.; Dill, K.; Haymet, A. A view of the hydrophobic effect. *J. Phys. Chem. B* **2002**, *106*, 521-533.

43. Dill, K. Dominant forces in protein folding. *Biochemistry* **1990**, 29, 7133-7155.

44. Upreti, M.; Jyoti, A.; Sethi, P. Tumor microenvironment and nanotherapeutics. *Trans. Cancer. Res*. **2013**, 2, 309-319.

45. Lee, S.; Chang, D.; Shim, M.; Kim, B.; Kim, S.; Seo, M. Ionically fixed polymeric nanoparticles as a novel drug carrier. *Pharm. Res*. **2007**, 24, 1508-1516.

46. Kaul, G.; Amiji, M. Long-circulating poly(ethylene glycol)-modified gelatin nanoparticles for intracellular delivery. *Pharm. Res*. **2002**, 19, 1061-1067.

47. Naito, K.; *et al*. Calicheamicin-conjugated humanized anti-CD33 monoclonal antibody (gemtuzumab zogamicin, CMA-676) shows cytocidal effect on CD33-positive leukemia cell lines, but is inactive on P-glycoprotein-expressing sublines. *Leukemia* **2000**, 14, 1436-1443.

48. Jin, Y.; Liu, S.; Yu, B.; Golan, S.; Koh, C.; Yang, J.; Huynh, L.; Yang, X.; Pang, J.; Muthusamy, N.; Chan, K.; Byrd, J.; Talmon, Y.; Lee, L.; Lee, R.; Marcucci, G. Targeted delivery of antisense oligodeoxynucleotide by transferrin conjugated pH-sensitive lipopolyplex nanoparticles: a novel oligonucleotide-based therapeutic strategy in acute myeloid leukemia. *Mol. Pharm.* **2010**, 7, 196-206.

49. Chang J.; Shim, W.;Yang, S.; Kwak, E.;Chong, S.; Kim, D.; Chung, S.; Shim, C. Liver cancer targeting of Doxorubicin with reduced distribution to the heart using

hematoporphyrin-modified albumin nanoparticles in rats. *Pharm. Res*. **2012**, 29, 795-805.

50. Yin, J.; *et al*. Label-free and turn-on aptamer strategy for cancer cells detection based on a DNA-silver nanocluster fluorescence upon recognition-induced hybridization. *Anal. Chem.* **2013**, 85, 12011-12019.

51. Yu, C.; He, X.; Wang, K.; Xu, F.; Shangguan, J.; He, D.; Shi H. Novel aptamer nanoparticle bioconjugates enhances delivery of anticancer drug to MUC1-positive cancer cells *in vitro*. *PLoS ONE* **2011**, 6, e24077.

52. Doll, T.; Raman, S.; Dey, R.; Burkhard, P. Nanoscale assemblies and their biomedical applications. *J. R. Soc. Interface* **2013**, 10, 20120740.

53. He, D.; Marles-Wright, J. Ferritin family proteins and their use in bionanotechnology. *New Biotechnol*. **2015**, 32, 651-657.

54. Brown, J.; Patterson, L.; Williamson, J.; Brown, J. Method for Analysis, and Distribution Profile, of Covalently-linked Ferritin-daunorubicin Conjugate in the Blood of Trypanosome-infected Mice. *J. Pharm. Pharmacol.* **1992**, 44, 48-51.

55. Aime, S.; Frullano, L.; Crich, S. Compartmentalization of a Gadolinium complex in the apoferritin cavity: A route to obtain high relaxivity contrast agents for magnetic resonance imaging. *Angew. Chem. Int. Ed*. **2002**, 41, 1017-1019.

56. Lin, X.; Xie, J.; Niu, G.; Zhang,F.; Gao, H.; Yang, M.; Quan, Q.; Aronova, M.; Zhang, M.; Lee, S.; Leapman, R.; Chen, S. Chimeric ferritin nanocages for multiplefunction loading and multimodal imaging. *Nano Lett.* **2011**, 11, 814-819.

57. Fan, K.; Gao, L.; Yan, X. Human ferritin for tumor detection and therapy. *Nanomed. Nanobiotechnol*. **2013**, 5, 287-298.

58. Falvo, E.; Tremante, E.; Fraioli, R.; Leonetti, C.; Zamparelli, C.; Boffi, A.; Morea, V.; Ceci, P.; Giacomini, P. Antibody-drug conjugates: targeting melanoma with cisplatin encapsulated in protein-cage nanoparticles based on human ferritin. *Nanoscale* **2013**, 5, 12278-12285.

59. Ebrahimi, K.; Hagedoorn, P.; Hagen, W. Unity in the biochemistry of the iron-storage proteins ferritin and bacterioferritin. *Chem. Rev*. **2015**, 115, 295-326.

60. Zhen, W.; Tang, W.; Chen, H.; Lin, X.; Todd, T.; Wang, G.; Cowger, T.; Chen, X.; Xie, J. RGD-modified apoferritin nanoparticles for efficient drug delivery to tumors. *ACS Nano* **2013**, 7, 4830-4837.

61. Zhen, Z.; Tang, W.; Todd, T.; Xie, J. Ferritins as nanoplatforms for imaging and drug delivery. *Expert Opin Drug Deliv*. **2014**, 11, 1913-1922.

62. Truffia, M.; Fiandraa, L.; Sorrentinoa, L.; Monieria,M.; Corsia,F.; Mazzucchellia, S. Ferritin nanocages: A biological platform for drug delivery, imaging and theranostics in cancer. *Pharmcol Res*. **2016**, 107, 57-65.

63. Klem, M.; Mosolf, J.; Young, M.; Douglas, T.; Science, N. Photochemical mineralization of europium, titanium, and iron oxyhydroxide nanoparticles in the ferritin protein cage. *Inorg. Chem*. **2008**, 47, 2237-2239.

64. Jacobs, J.; Hasan, M.; Paik, K.; Hagen, W.; van Loosdrecht, M. Development of a bionanotechnological phosphate removal system with thermostable ferritin. *Biotechnol. Bioeng.* **2010**, 105, 918-923.

65. Butts, C.; Swift, J.; Kang, S-G.; Di Costanzo, L.; Christianson, D.; Saven, J.; Dmochowski, I. Directing noble metal ion chemistry within a designed ferritin protein. *Biochemistry* **2008**, 47, 12729-12739.

66. Zhao, L.; Seth, A.; Wibowo, N.; Zhao, C-X.; Mitter, N.; Yu, C.; Midddleberg, A. Nanoparticle vaccines. *Vaccine* **2014**, 32, 327-337.

67. Kratz, P.; Bottcher, B.; Nassal, M. Native display of complete foreign protein domains on the surface of hepatitis B virus capsids. *Proc. Natl. Acad. Sci. USA*. **1999**, 96, 1915-1920.

68. Mayes, E.; Bewick, A.; Gleeson, D.; Hoinville, J.; Jones, R.; Kasyutich, O.; Nartowski, B.; Warne, J.; Wiggins, K.; Wong, K. Biologically derived nanomagnets in self-organized patterned media. *IEEE. Trans. Magn*. **2003**, 39, 624-627.

69. Frolow, F.; Kalb, A.; Yariv, J. Structure of a unique two fold symmetrical heme binding site. *Nat. Struct. Biol.* **1994**, 1, 453-460.

70. Andrew, S.; Lebrun, N.; Barynin, V.; Thomson, A.; Moore, G.; Guest, J.; Harrison, P. Site-directed replacement of the coaxial heme ligands of bacterioferritin generates heme-free variants. *J. Biol. Chem.* **1995**, 270, 23268-23274.

71. Dunford, H. Oxidations of iron(II)/(III) by hydrogen peroxide: from aquo to enzyme. *Coord. Chem. Rev*. **2002**, 233, 311-318.

72. Pulliainen, A.; Kauko, A.; Haataja, S.; Papageorgiou, A.; Finne, J. Dps/Dpr ferritin-like protein: insights into the mechanism of iron incorporation and evidence for a central role in cellular iron homeostasis in Streptococcus suis. *Mol. Microbiol.* **2005**, 57, 1086-1100.

73. Crow, A.; Lawson, T.; Lewin, A.; Moore, G.; Le Brun, N. Structural basis for Iron mineralization by bacterioferritin. *J. Am. Chem. Soc.* **2009**, 131, 6808-6813.

74. Yang, X.; Le Brun, N.; Thomson, A.; Moore, C.; Chasteen, N. The iron oxidation and hydrolysis chemistry of Escherichia coli bacterioferritin. *Biochemistry* **2000**, 39, 4915-4923.

75. Zhang, y.; Orner, B. Self-assembly in the ferritin nano-cage protein superfamily. *Int. J. Mol. Sci.* **2011**, 12, 5406-5421.

76. Wahlgren, W.; Omran, H.; Von Stetten, D.; Royant, A.; van der Post, S.; Katona, G. Structural characterization of bacterioferritin from blastochloris viridis. *PLoS ONE* **2012**, 7, e46992.

77. Wong, S.; Grigg, J.; Le Brun, E.; Moore, G.; Murphy, M.; Mauk, A. The B-type channel is a major route for iron entry into the ferroxidase center and central cavity of bacterioferritin. *J. Biol. Chem.* **2015**, 290, 3732-3739.

78. Neya, S.; Nagai, M.; Nagatomo, S.; Hoshino, T.; Yoneda, T.; Kawaguchi, A. Utility of heme analogues to intentionally modify heme-globin interactions in myoglobin. *Biochim. Biophys. Acta.* **2016**, 1857, 582-588.

79. Kobayashi, K.; Nagamune, T.; Furuno, T.; Sasabe, H. Monomolecular layer of alkylated Cytochrome p450 formed at the air/water interface. *Bull. Chem. Soc. Jpn.* **1999**, 72, 691-696.

80. van der Ven, A. Protein engineering of bacterioferritin: Applications to bionanotechnology. **2014**, M.Sc. Thesis, University of Waterloo.

81. Kamaly, N.; Xiao, Z.; Valencia, P.; Radovic-Moreno, A.; Farokhzad, O.Targeted polymeric therapeutic nanoparticles: design, development and clinical translation. *Chem. Soc. Rev.* **2012**, 41, 2971-3010.

82. Ji, X.; Huang, L.; Huang, H. Construction of nanometer cisplatin core-ferritin (NCC-F) and proteomic analysis of gastric cancer cell apoptosis induced with cisplatin released from the NCC-F. *J. Proteomics* **2012**, 75, 3145-3157.

83. Comellas-Aragones, M.; Engelkamp, H.; Claessen, V.; Sommerdijk, N.; Rowan, A.; Christianen, P.; Maan, J.; Verduin, B.; Cornelissen, J.; Nolte, R. A virus-based single-enzyme nanoreactor. *Nat. Nanotechnol.* **2007**, 2, 635-639.

84. Patterson, D.; LaFrance, B.; Douglas, T. Rescuing recombinant proteins by sequestration into the P22 VLP. *Chem. Commun.* **2013**, 49, 10412-10414.

85. Patterson, D.; Schwarz, B.; Waters, R.; Gedeon, T.; Douglas, T. Encapsulation of an enzyme cascade within the bacteriophage P22 virus-like particle. *ACS Chem. Biol*. **2013**, 9, 359-365.

86. Stephanopoulos, N.; Tong, G.; Hsiao, S.; Francis, M. Dual-surface modified virus capsids for targeted delivery of photodynamic agents to cancer cells. *ACS Nan.* **2010**, 4, 6014-6020.

87. Goldsmith, L.; Pupols, M.; Kickhoefer, V.; Rome, L.; Monbouquette, H. Utilization of a protein "shuttle" to load vault nanocapsules with gold probes and proteins. *ACS Nano* **2009**, 3, 3175-3183.

88. Choi, K.; Choi, S.; Jeon, H.; Kim, I.; Ahn, H. Chimeric capsid protein as a nanocarrier for siRNA delivery: stability and cellular uptake of encapsulated siRNA. *ACS Nano* **2011**, 5, 8690-8699.

89. Suttisansanee, U. Biochemistry in Bacterioferritin. **2006,** Unpublished doctoral dissertation, University of Waterloo, Waterloo, Ontario Canada.

90. Huang, Z.; Park, J.; Watson, D.; Hwang, P.; Szoka, F. Facile synthesis of multivalent nitrilotriacetic acid (NTA) and NTA conjugates for analytical and drug delivery applications. *Bioconjug. Chem.* **2006**, 17, 1592-1600.

91. Fruk, L.; Kuhlmann, J.; Niemeyer, C. Analysis of heme-reconstitution of apoenzymes by means of surface plasmon resonance. *Chem. Commun.* **2009**, 2009, 230-232.

92. Thirstrup, D.; Baird, G.S. Histochemical application of a peroxidase DNAzyme with a covalently attached hemin cofactor. *Anal. Chem*. **2010**, 82, 2498-250.

93. Murakami, H.; Nagasaki, T.; Hamachi, I.; Shinkai, S. Sugar sensing utilizing aggregation properties of boronic-acid-appended porphyrins and metalloporphyrins. *Tetrahedron Lett*. **1995**, 34, 975-981.

94. Zhang, Y.; Huang, Y.; Li, S. Polymeric micelles: nanocarriers for cancer-targeted drug delivery. *AAPS. Pharm. Sci. Tech*. **2014**, 15, 862-871.

95. Bombelli, C; Giansanti, L; Luciani, P; Mancini, G. Gemini surfactant based carriers in gene and drug delivery. *Curr. Med. Chem*. **2009**, 16, 171-183.

96. Taksim, A.; Kamel, A.; Wettig, S. Interactions between DNA and gemini surfactant: Impact on gene therapy: Part I. *Nanomedicine (Lond).* **2016**, 11, 289-306.

97. Sultana, S.; Khan, M.; Kumar, M.; Kumar, S.; Ali, M. Nanoparticles-mediated drug delivery approaches for cancer targeting: a review. *J. Drug Target.* **2013**, 21, 107-125.

98. Forrest, M.; Yanez, J.; Remsberg, C.; Ohgami, Y.; Kwon, G.; Davies, N. Paclitaxel prodrugs with sustained release and high solubility in poly(ethylene glycol)-b-poly (ε-caprolactone) micellenanocarriers: pharmacokinetic disposition, tolerability, and cytotoxicity. *Pharm. Res.* **2008**, 25, 194-206.

99. Yoo, H.; Park, T. Biodegradable polymeric micelles composed of doxorubicin conjugated PLGA-PEG block copolymer. *J. Control. Release* **2001**, 70, 63-70.

100. Pathak, J.; Liu, J.; Zeng, Y.; Shi, S.; Xu, L.; Zhang, H.; Pan, Y. Design of polyaspartic acid peptide-poly (ethylene glycol)-poly (ε-caprolactone) nanoparticles as a carrier of hydrophobic drugs targeting cancer metastasized to bone. *Int. J. Nanomedicine* **2017**, 12, 3561-3575.

101. Gaber, N.; Darwis, Y.; Peh, K.; Tan, Y. Characterization of polymeric micelles for pulmonarydelivery of beclomethasone dipropionate. *J. Nanosci. Nanotechnol.* **2006**, 6, 3095-3101.

102. Dong, H.; Li, Y.; Cai, S.; Zhuo, R.; Zhang, X.; Liu, L. A facile one-pot construction of supramolecular polymer micelles from a-cyclodextrin and poly(e caprolactone). *Angew. Chem. Int. Ed*. **2008**, 47, 5573-5576.

103. Wiradharma, N.; Tong, Y.; Yang, Y. Self-assembled oligopeptide nanostructures for co-delivery of drug and gene with synergistic therapeutic effect. *Biomaterials* **2009**, 30, 3100-3109.

104. Akbarzadeh, A.; Rezaei-Sadabady, R.; Davaran, S.; Joo, S.; Zarghami N.; Hanifehpour, Y.; Samiei, M.; Kouhi, M.; Nejati-Koshki, K. Liposome: classification, preparation, and applications. *Nanoscale Res. Lett*. **2013**, 8,102.

105. Ménard, N.; Tsapis, N.; Poirier, C.; Arnauld, T.; Moine, L.; Lefoulon, F.; Péan, J.; Fattal, E. Drug solubilization and in vitro toxicity evaluation of lipoamino acid surfactants. *Int. J. Pharm*. **2012**, 423, 312-320.

106. Zaragoza-Galán, G.; Fowler, M.; Duhamel, J.; Rein, R.; Solladié, N.; Rivera, E. Synthesis and characterization of novel pyrene-dendronized porphyrins exhibiting efficient fluorescence resonance energy transfer: optical and photophysical properties. *Langmuir* **2012**, 28, 11195-11205.

107. Bains, G.; Kim, S.; Sorin, E.; Narayanaswami, V. The extent of pyrene excimer fluorescence emission is a reflector of distance and flexibility: Analysis of the segment linking the LDL receptor-binding and tetramerization domains of apolipoprotein E3. *Biochemistry* **2012**, 51, 6207-6219.

108. Lawson, T.; Crow, A.; Lewin, A.; Yasmin, S.; Moore, G.; Le Brun, N. Monitoring the iron status of the ferroxidase center of *Escherichia coli* bacterioferritin using fluorescence spectroscopy. *Biochemistry* **2009**, 48, 9031-903.

109. Platt, V.; Huang, Z., Cao, L., Tiffany, M., Riviere, K., Szoka, F. Influence of multivalent nitrilotriacetic acid lipid-ligand affinity on the circulation half-life in mice of a liposome-attached his_6-protein. *Bioconjugate Chem.* **2010**, 21, 892-902.

110. Zhong, H.; Zhang,H.; Liu,Z.; Yang,X.; Brusseau, M.; Zeng, G. Sub-CMC solubilization of dodecaneby rhamnolipid in saturatedporous media. *Sci. Rep.* **2016**, 6.

111. Zhong, H. Yang, L.; Zeng, G.; Brusseau, M.; Wang, Y.; Li, Y.; Liu, Z.; Yuan, X.; Tan, F. Aggregate-based sub-CMC solubilization of hexadecane by surfactants. *RSC. Adv.* **2015**, 5, 78142-78149.

112. Park, J.; Kim, H.; Cho, S.; Lee, M. Characterization of hydrophobic anti-cancer drug-loaded amphiphilic peptides as a gene carrier. *J. Cell. Biochem.* **2012**, 113, 1645-1653.

113. Kabanov, A.; Chekhonin, V.; Alakhov, V.; Batrakova, E.; Lebedev, A.; Melik-Nubarov, N.; Arzhakov, S.; Levashov, A.; Morozov, G.; Severin, E. The neuroleptic activity of haloperidol increases after its solubilization in surfactant micelles: Micelles as microcontainers for drug targeting. *FEBS. Lett*. **1989**, 258, 343-345.

114. Derossi, D.; Joliot, A.; Chassaing, G.; Prochiantz, A. The third helix of the Antennapedia homeodomain translocates through biological membranes. *J. Biol. Chem.* **1994**, 269, 10444-10450.

115. El-Andaloussi, S.; Johansson, H.; Holm, T.; Langel, U. A novel cell-penetrating peptide, M918, for efficient delivery of proteins and peptide nucleic acids. *Mol. Ther.* **2007**, 15, 1820-1826.

116. Morris, M.; Depollier, J.; Mery, J.; Heitz, F.; Divita, G. A peptide carrier for the delivery of biologically active proteins into mammalian cells. *Nat. Biotechnol.* **2001**,19, 1173-1176

Appendix

Appendix 1: Standard curve calculations used to estimate the number of pyrene molecules within the engineered His6-Bfr cage protein

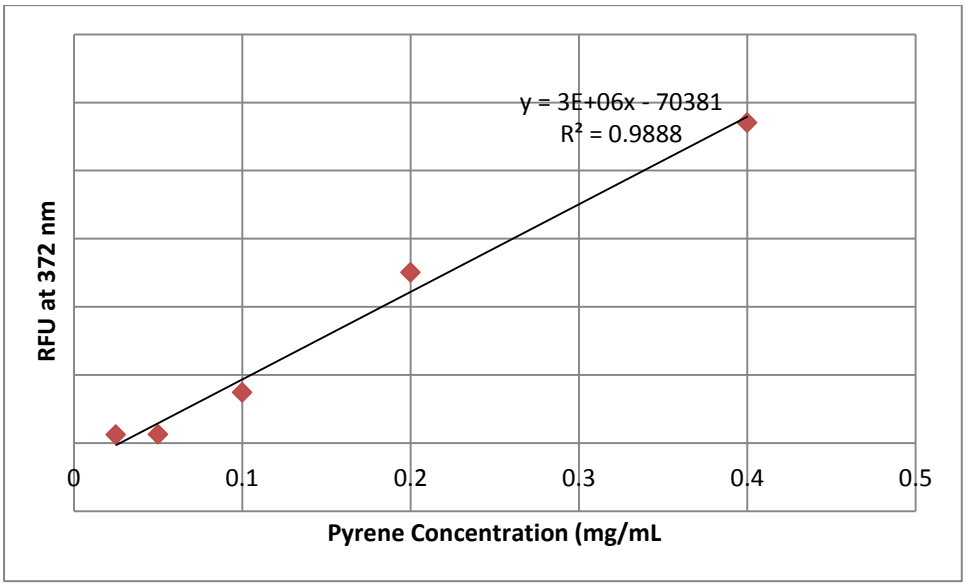

$RFU_{py\text{-}Bfr} = 3\times 10^{6}X - 70381$ → X is the concentration of pyrene in the His6-Bfr sample

$RFU_{py\text{-}Bfr} = 274556$

$X = 158556 + 70381 / 3\times 10^{6}$

X= 0.076 mg/mL or 0.37 mM

The concentration of the Bfr in the sample= 0.06 mM.

The number of equivalents of pyrene per a protein cage= 6.17

However, this result is only an estimate of the number of pyrene molecules within a single Bfr capsule since the emission intensity in the protein sample could be reduced by different factors as described in Chapter 3.